REPORT DOCUMENTATION PAGE

1. AGENCY USE ONLY (Leave Blank)	2. REPORT DATE	3. REPORT TYPE AND DATES COVERED
	1994	Final

4. TITLE AND SUBTITLE
Specific Interactions in Polyurethane Cationomers

5. FUNDING NUMBERS

6. AUTHORS
Richard Joseph Goddard

7. PERFORMING ORGANIZATION NAME(S) AND ADDRESS(ES)
University of Wisconsin-Madison

AFRL-SR-BL-TR-98-

9. SPONSORING/MONITORING AGENCY NAME(S) AND ADDRESS(ES)
AFOSR/NI
110 Duncan Avenue, Room B-115
Bolling Air Force Base, DC 20332-8080

...MONITORING
...ENCY REPORT NUMBER

11. SUPPLEMENTARY NOTES

12a. DISTRIBUTION AVAILABILITY STATEMENT
Approved for Public Release

12b. DISTRIBUTION CODE

13. ABSTRACT *(Maximum 200 words)*
See attached.

19980115 188

14. SUBJECT TERMS	15. NUMBER OF PAGES
	16. PRICE CODE

17. SECURITY CLASSIFICATION OF REPORT	18. SECURITY CLASSIFICATION OF THIS PAGE	19. SECURITY CLASSIFICATION OF ABSTRACT	20. LIMITATION OF ABSTRACT
Unclassified	Unclassified	Unclassified	UL

SPECIFIC INTERACTIONS IN POLYURETHANE CATIONOMERS

by

RICHARD JOSEPH GODDARD

A dissertation submitted in partial fulfillment

of the requirements for the degree of

Doctor of Philosophy

(Chemical Engineering)

at the

UNIVERSITY OF WISCONSIN-MADISON

1994

19980115 188

SPECIFIC INTERACTIONS IN POLYURETHANE CATIONOMERS

Richard Joseph Goddard

Under the supervision of Professor Stuart L. Cooper

At the University of Wisconsin-Madison

Studies have shown that addition of cationic groups to a segmented polyurethane can dramatically change physical attributes such as solution behavior, mechanical strength, and viscoelastic properties. However, the specific interactions responsible for these changes are not well understood. A series of polyether polyurethane cationomers were synthesized using chain extenders with pendant trialkylammonium groups. The morphology and properties of the cationomers were studied as a function of ion-related variables using small-angle X-ray scattering (SAXS), tensile testing, dynamic mechanical thermal analysis (DMTA), and differential scanning calorimetry (DSC). Ion content affected phase separation and mechanical properties the most; the alkyl group length was of secondary importance; and the type of neutralizing anion had essentially no effect. Further, a lamellar microstructure typical of conventional polyurethanes was evident, with no apparent aggregation of ionic groups.

When the cationomers were annealed at room temperature for a period of approximately one month, DSC thermograms showed an endotherm centered near 70°C which was not present in the unannealed polymer. Extended X-ray absorption fine

structure temperature studies demonstrated that the endotherm corresponds to water leaving the coordination shell of the anion.

Fourier transform infrared temperature studies were completed to gain further insight into the nature of the specific interactions in these cationomers. Results showed that the interurethane N-H to C=O hydrogen bond found in typical polyurethanes was replaced by a stronger interaction between urethane N-H groups and the neutralizing anion. With no evidence of ionic aggregation, these interchain ties are apparently the primary interaction which "hold the cationomers together." A reversible shift in N-H hydrogen bonding, from the anion to urethane carbonyls, was observed on heating.

The flow transition in DMTA appears to be a direct consequence of this redistribution of hydrogen bonds. Since the number of N-H to anion bonds responsible for phase separation decreased at elevated temperatures, SAXS temperature studies and dynamic viscoelastic measurements were performed to determine if the cationomers passed through a microphase separation transition. Although considerable intersegmental mixing accompanied macroscopic flow, evidence of the lamellar microstructure persisted into the melt, and a homogenous phase was not observed.

_____   _____
Stuart L. Cooper   Date

Acknowledgements

This section is my opportunity to say thank you to everyone who has helped make this thesis possible. To those included, hopefully you have heard me say thanks many times before, but undoubtedly it was not said often enough. To those inadvertently not mentioned, please accept my apology in advance, and know that your role was no less appreciated or important.

It is not possible for me to list all the things, in addition to his guidance and support, that Professor Stuart L. Cooper has contributed as a thesis advisor. Most importantly, he has created a graduate research environment where one is surrounded by excellence, exploring new ideas is encouraged, presentation of work is expected, and money is seldom a constraint.

A number of people deserve special recognition for their direct contribution to this research: previous Cooper group graduate students Craig Myers who supplied data on the sample PU-BD, and Brian Grady who co-investigated the room temperature annealing peak; fellow graduate student Ellen O'Connell for obtaining ^{1}H-NMR data; undergraduate student helpers Rick Reiner for obtaining DSC data while Brian and I were running EXAFS experiments at SSRL, and Todd Scheele for assistance with FTIR sample preparation and data analysis. Others include the operators and staff at SSRL and CHESS for their assistance in performing EXAFS studies, Professor Robert McMahon and his research group who let me use their FTIR while the department's new instrument was on order, and Professor Michael Winokur and Ty Prosa for maintaining the somewhat antiquated X-ray generator where SAXS experiments were performed. The technical

Lastly and most importantly, I wish to acknowledge the people in my life outside of graduate school, although the list is incomplete and the praise too short. I want to thank my parents, Frederick and Carolyn Goddard, for everything they have given me over the years, particularly: encouragement and independence, discipline and freedom, and love and friendship. I must thank my wife, Melanie, for her love, support, and understanding. For the last 4+ years, you have endured an adverse climate (both atmospheric and political), worked at jobs less than satisfying, and put your career on hold. It is your turn now.

Table of Contents

Table of Figures

Table of Tables

Chapter I. Introduction

A. Chemistry and Structure of Conventional Polyurethanes

Polyurethanes (PU) are a broad class of condensation polymers characterized by the urethane (-NH-CO-O-) linkage. The urethane linkage is formed by the reaction of isocyanate-containing and hydroxy-containing monomers. Polyurethane chemistry offers tremendous versatility, and an almost limitless variety of chemical components and compositions are possible. The resulting wide range of physical properties have led to commercial applications of PUs in such areas as low-density flexible foams, rigid structural foams, tough elastomers, high-performance thermoplastics, and durable coatings.

PU elastomers belong to the family of linear multiblock copolymers of the type $(AB)_n$ where at the service temperature one block of the material is glassy or semicrystalline, and the other block is soft or rubbery. In most cases, the soft segments are oligomeric diols of polyethers or polyesters with molecular weights between 500 and 5000, while the hard segments are generally composed of an aromatic diisocyanate chain extended by a low molecular weight diol. Unfavorable interactions between the two segments lead to a microphase-separated structure where the hard domains act as physical crosslinks and reinforcing filler. A primary driving force for microphase separation in PUs is the higher polarity of the urethane segments as compared to the soft segments. Phase separation is usually further enhanced by interurethane hydrogen bonds and/or crystallization driving forces. Consequently, microphase separation can occur at segment molecular weights lower than 1000 g/mol. This is in marked contrast to the amorphous

styrene-diene block copolymers where due to weaker van der Waals driving forces, microphase separation requires segment molecular weights approaching 10,000 g/mol.

The two-phase microstructure of PU elastomers was first reported by Cooper and Tobolsky.[1] Since that time, the morphology of PU elastomers has been extensively studied because of its strong influence on physical properties.[2-11] Both the domains and the interdomain spacings of segmented PUs are generally on the order of tens to hundreds of Angstroms, and phase separation is far from ideal. As such, a variety of morphological features may contribute to the mechanical properties as indicated in the schematic of Figure I-1. Possible structural components include hard segment crystallites with varying degrees of order, amorphous hard segments, amorphous or semi-crystalline soft domains with dissolved hard segments, soft segments within hard domains, and interfaces between phases. Although the hard and soft domains have been directly observed using electron microscopy,[12,13] the experiments are inherently difficult due to factors such as the small domain sizes (less than ~ 100Å), beam damage, and a lack of long range order in the PU microstructure. A much more common technique for analyzing the morphology of multiblock PUs is small-angle X-ray scattering (SAXS), which provides information on domain sizes and arrangement, the degree of phase separation, and the interfacial region.[14-18] Physical methods such as differential scanning calorimetry[19-22] (DSC) and dynamic mechanical thermal analysis (DMTA)[23-25] provide further morphological information on the purity and crystallinity of both phases.
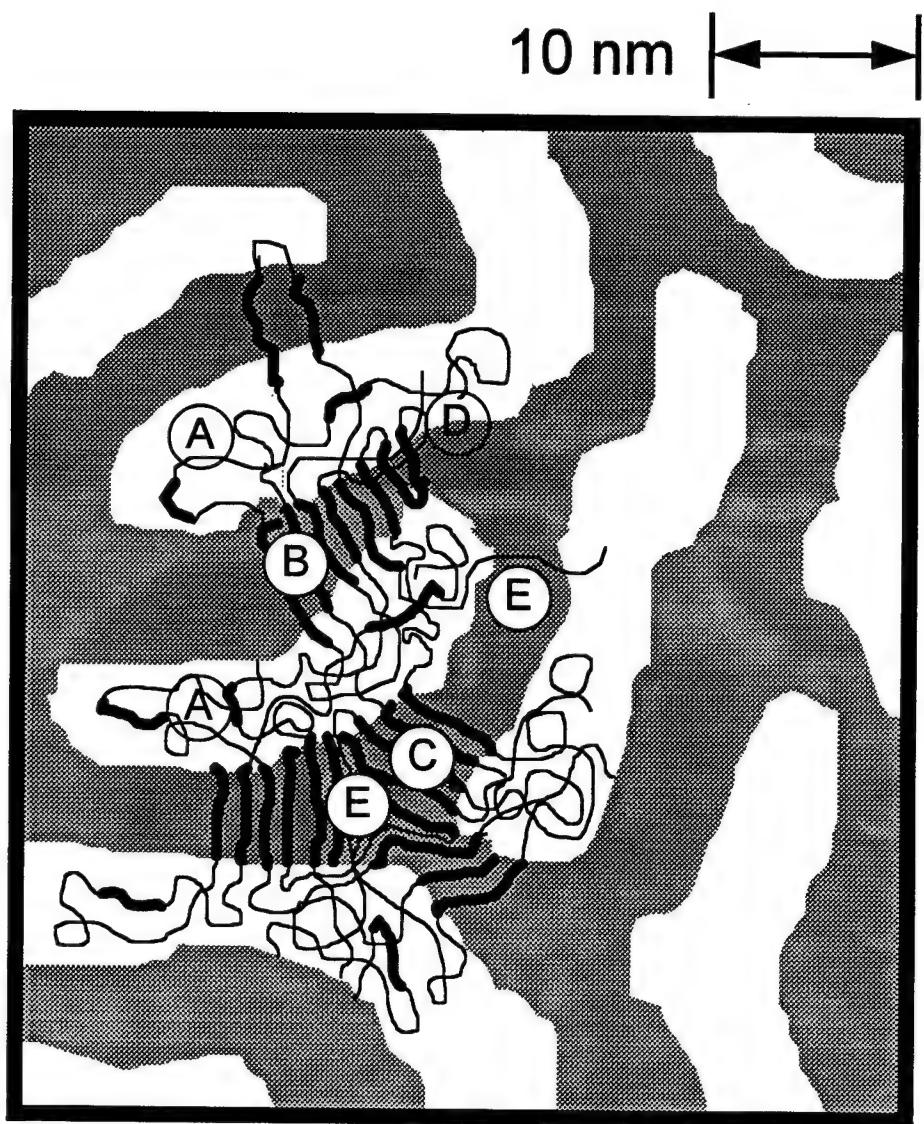
Figure I-1.   Schematic showing possible morphological features in a multiblock polyurethane elastomer: (A) amorphous soft domain with dissolved hard segments, (B-C) hard segment crystallites with differing degrees of order, (D) interface, and (E) soft segments within hard domains.

B. Polyurethane Cationomers

Ionic groups have also been incorporated in the structure of segmented polyurethanes to improve phase separation, hard domain cohesion, or the ability of the polymer to emulsify or dissolve in polar solvents. When the concentration of ionic groups is approximately 1 meq/g or less, the term polyurethane ionomer is used to describe the material. PU ionomers may be further classified as anionomers, cationomers, or zwitterionomers depending on which charge (negative, positive or both, respectively) is covalently bonded to the polymer. Dietrich and co-workers[26] reviewed a variety of early syntheses for ion-containing PUs. Two general schemes were presented. In the first, ionic groups are introduced during the polymerization by chain extension with ionic diols. An alternative strategy is to derivatize a previously prepared PU with suitable reagents. Depending on the chemical structure, two different arrangements of ionic groups have been observed in PU ionomers. Ionic groups may aggregate within an otherwise one-phase matrix[27,28] (Figure I-2), or ionic aggregation may be superimposed on the already present two-phase morphology (eg. Figure I-1) of the non-ionic precursor.[29,30]

A modest number of previous investigations on polyurethane cationomers have been reported.[26,31-45] Dietrich and co-workers were the first to describe the synthesis and properties of polyurethane cationomers.[26] They found that PUs chain extended with N-methyldiethanolamine (MDEA) lacked elastomeric character, passing directly from the glassy state into viscous flow during shear modulus tests. Quaternization of MDEA effectively crosslinked the material, increasing the tensile strength and modulus by factors of 20 to 40, and extending the elastic temperature regime over 120°C. Interchain
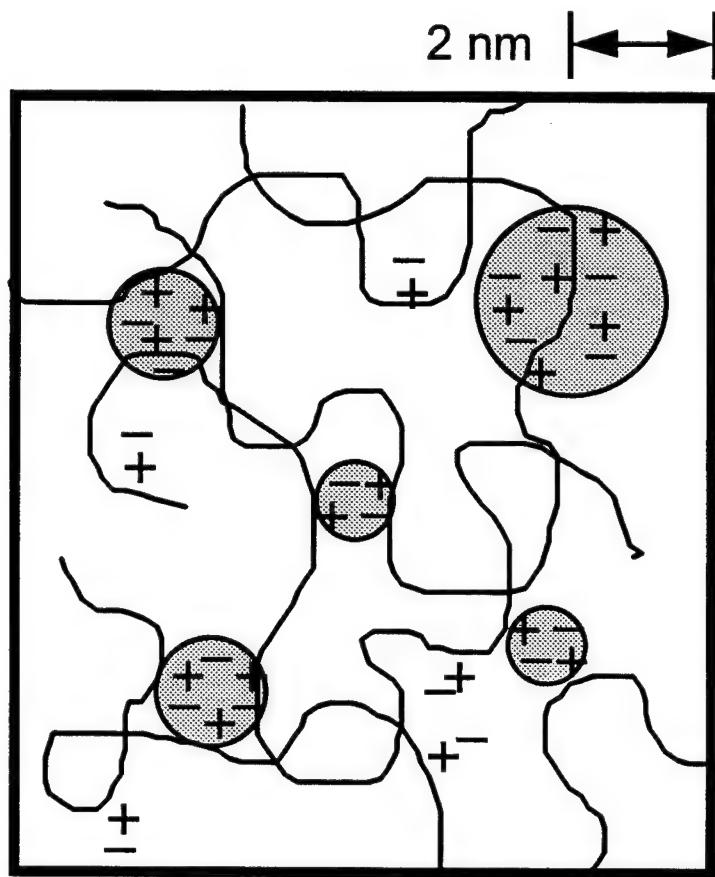
Figure I-2. Schematic of ionic aggregation in an amorphous polymer matrix.

association of ionic groups were also observed in non-aqueous solutions of the cationomers, with the apparent molecular weight determined from viscosity measurements increasing rapidly with increasing concentration. Aqueous dispersions of similar PU cationomers were prepared by Lorenz et al.[31] Aggregation of the ionic species was noted in solutions of acetone. The first additions of water to the acetone solution disrupted the physical network by solvating the ions, while further water addition increased the associations of hydrophobic polymer segments. In the bulk state, the PU cationomers behaved like crosslinked materials, with a linear dependence between the modulus and the square of the ion concentration.

The first microstructural investigations of PU cationomers were completed by a group of scientists at the Ukrainian Academy of Sciences. In a series of segmented PUs with pendant quaternary ammonium groups, SAXS revealed no significant changes in morphology with different halogen anions or between the cationomers and the unionized control.[32] In these same polymers, Lipatov and co-workers[33] also found that an increase in ion content improved phase separation, but otherwise affected the microstructure very little. Wide-angle diffraction patterns showed no evidence of crystallinity before or after quaternization, and ionization produced no new features in the SAXS patterns. The interdomain spacing of a 70% neutralized cationomer was 20% greater than the unionized control, but did not change as the extent of neutralization was increased to 100%. Khranovskii et al. studied the intermolecular interactions in oligourethanes with terminal ammonium groups using infrared spectroscopy.[34] Changes in the spectral regions sensitive to hydrogen bonding led them to conclude that the structure of hydrogen bonds

between urethane N-H and C=O groups that is found in conventional polyurethanes was completely replaced by a new network of hydrogen bonds between the urethane N-H and the counter anion. They later postulated that a wide variety of interactions existed, including ionic aggregation and a number of hydrogen bonded and ion-dipole structures.[33] Nierzwicki and Rutkowska[35] investigated the degree of microphase separation in a PU cationomer versus a conventional polyurethane using dynamic mechanical studies and proton nuclear magnetic resonance decay experiments. The cationomer displayed greater phase separation, sharper interfaces, and less molecular motion within the hard domains; however, use of a covalently crosslinked ionomer and a linear polymer as a control complicated interpretation of results.

Al-Salah and co-workers investigated structure-property relationships in PU cationomers formed by the quaternization of PUs chain extended with N-alkyl diethanolamine (ADEA).[36] Variations in physical properties with molecular weight of the soft segment and isocyanate type were the same as in conventional PUs. Mechanical properties improved significantly with increasing ion concentration and decreasing carbon number of the ADEA alkyl group, while the type of organic acid used as the quaternizing agent had less of an effect. Structure-property relationships were also investigated by Chan and Chen in multiblock PU cationomers with MDEA as the chain extender.[37-41] In their polymer systems, the unionized controls already displayed a high degree of phase separation. Consequently, dynamic mechanical analyses showed insignificant changes in phase separation when the polymers were quaternized. Addition of cationic groups did however improve hard domain cohesion, as evidenced by an increase in the tensile

modulus with increasing ammonium concentration. The effect of isocyanate type on mechanical properties was again comparable to that in conventional polyurethanes.

A few investigators have reported novel syntheses of PU cationomers, with characterization generally only of the reaction products. Buruiană and co-workers synthesized cationomers by quaternizing a PU with piperazine rings in the chain backbone, and noted a polyelectrolyte effect in dilute solutions of N,N-dimethylformamide.[42] Tanaka and Nakaya observed liquid crystalline behavior in some PU cationomers with quaternary ammonium groups in the main chain and long alkyl side chains; the polymers consisted only of diisocyanate and low molecular weight diols (i.e. they were not segmented).[43] Multiblock PU cationomers containing pendant trimethylammonium groups were synthesized using ionic diols by Varma et al.,[44] while Chattopadyay and co-workers introduced pendant triethylammonium groups using halide-containing chain extenders followed by ionization of the base PU with triethylamine.[45]

In general, the previous studies have shown that addition of cationic groups to a polyurethane can dramatically change physical attributes such as solution behavior, mechanical strength, and viscoelastic properties. Although a few investigators have proposed models to explain such effects, the nature of the interactions in these materials are not well understood. Research presented in this thesis was directed toward two goals. The first was to systematically investigate the effect of ion-related variables on the microstructure and physical properties of polyurethane cationomers. The second goal was to obtain a greater fundamental understanding of the specific interactions in these systems and the temperature dependence of those interactions. Knowledge from such

investigations is important in the development of new and improved materials, and in tailoring polymer properties by varying processing conditions.

The synthesis of the novel polyurethane cationomers used throughout the thesis is described in Chapter II. Cationomers with pendant trialkylammonium groups, as opposed to ionic functionality in the polymer backbone, were chosen for study since the pendant ion-pair might augment specific interactions through its greater accessibility. Chapter II also details the experimental protocol used to characterize the cationomers and their behavior. The effects of ion content, alkyl group length, and neutralizing anion on the microstructure and physical properties of the PU cationomers are reported in Chapter III. A number of parameters commonly varied in PU structure-property investigations (such as hard segment content, isocyanate type, soft segment type or molecular weight) were not studied, since these variables are not ion-related, and earlier studies have indicated that the effects of these variables are the same as in conventional polyurethanes.

Results of Chapter III prompted further investigation into a number of areas related to the nature of the specific interactions in these systems. During the initial characterization of these materials, DSC showed the development of a small endothermic peak at approximately 80°C when the quaternized polymers were stored at room temperature for a period of approximately one month in a desiccator filled with dry calcium sulfate. Some authors have suggested that a similar "room temperature annealing peak" in other ionomers was related to the development of order within ionic aggregates. Using the extended X-ray absorption fine-structure (EXAFS) technique, this phenomenon was investigated in the PU cationomers as described in Chapter IV. Additional insight

10

into the various interactions found in PU cationomers was provided by the Fourier transform infrared (FTIR) temperature studies of Chapter V. Spectral deconvolution and mass balances were used to obtain semiquantitative information on the distribution of specific interactions in the cationomers as a function of temperature and ion content. Results at elevated temperatures showed a marked decrease in the interaction primarily responsible for phase separation in the quaternized PUs. Because of this, the morphology of the PU cationomers was studied as a function of temperature using SAXS and dynamic viscoelastic measurements. A discussion of the experimental results is presented in Chapter VI. In Chapter VII, the major conclusions are summarized and further research in related areas is recommended.

Chapter II. Experimental Methods

A. Materials and Syntheses

A.1. Materials. N,N-dimethylacetamide (DMAc) (Anhydrous, 99+%, Aldrich) was used as received. Diphenylmethane-4,4'-diisocyanate (MDI) (Polysciences) was melted and pressure filtered at 60°C to separate the monomer from dimers, then stored at -20°C until required. 3-dimethylamino-1,2-propanediol (DMP), 3-diethylamino-1,2-propanediol (DEP), 3-dipropylamino-1,2-propanediol (DPP), iodomethane, iodoethane, 1-iodopropane (Aldrich), stannous octoate (Air Products), sodium bromide, sodium chloride, ammonium fluoride, magnesium sulfate, toluene and absolute methanol (Mallinckrodt) were used as supplied by the manufacturers. Polytetramethylene glycol, $\overline{M}_n$ =990 (PTMO) (QO Chemicals) was freed of water by azeotropic distillation in a 10:1 (v/v) ratio of DMAc and toluene immediately prior to use.

Model compounds used in the extended X-ray absorption fine structure (EXAFS) study were tetramethylammonium bromide, sodium bromate, and carbon tetrabromide (Aldrich). The first two were dried in a vacuum oven to remove any absorbed water before use, while the latter was used as received. A 90% polyethylene/10% bromine compound mixture by weight was compression molded into disks at 130°C and 60 MPa for 4 minutes. Preparing the model compounds in this manner allowed for easy insertion of the sample into the path of the X-ray beam.

A.2. Synthesis of 3-trimethylammonium-(1,2-propanediol)iodide (TMPI). 15.0 g (0.126 mol) of DMP in 200 mL of toluene was heated to 40°C under constant agitation and an argon purge. Addition of 35.8 g (0.252 mol) of iodomethane,

approximately 200% of theoretical, resulted in rapid precipitation of TMPI in the form of a white powder. The mixture was allowed to cool to room temperature and kept under stirring in an argon atmosphere for 1 h. The product TMPI was filtered, washed with fresh toluene, recrystallized from a minimum of absolute methanol, and washed with toluene again. A similar procedure for TMPI synthesis was previously reported by Varma $et\ al.$[44] Yield=95%. ^{1}H NMR (D_2O): δ 2.48 (s, 2H, -CHOH-, CH$_2$OH, broad); 1.99-2.03 (m, H, -CHOH-, broad); 1.08-1.32 (m, 2H, -CH_2OH, m, 2H, -N$^+$CH_2-); 0.95 (s, 9H, CH_3-).

A.3. Synthesis of 3-triethylammonium-(1,2-propanediol)iodide (TEPI).

10.0 g (0.068 mol) of DEP in 50 ml of toluene was heated to 85°C under constant agitation and an argon purge. Excess iodoethane, 21.2 g (0.136 mol), was added and after 10-20 min a small amount of cloudy TEPI precipitate was observed. The reaction mixture was kept under stirring, reflux, and an argon purge at 85°C for 20 h. The reaction was shielded from light to avoid yellowing of the product. Filtering and purification of TEPI was the same as for TMPI. Yield=98%. ^{1}H NMR (D_2O): δ 2.44 (s, 2H, -CHOH-, CH$_2$OH, broad); 1.86-1.89 (m, H, -CHOH-, broad); 0.98-1.32 (m, 2H, -CH_2OH, m, 2H, Et$_3$N$^+$CH_2-, m, 6H, CH$_3$CH_2-); ⁻1.09-⁻1.02 (t, 9H, CH_3CH$_2$-).

A.4. Synthesis of 3-tripropylammonium-(1,2-propanediol)iodide (TPPI).

10.0 g (0.057 mol) of DPP in 50 ml of toluene was heated to 100°C under constant agitation and an argon purge. Excess iodopropane, 19.4 g (0.114 mol), was added and the reaction mixture was kept under stirring, reflux, and an argon purge at 100°C for 20 h. The reaction was shielded from light to avoid yellowing of the product. At the end

of 20 h, TPPI was present in the bottom of the reaction flask as a viscous light-yellow liquid. Filtering and purification of TPPI was the same as for TMPI, except that refrigeration was necessary to crystallize TPPI. Yield=90%. ^{1}H NMR (D$_2$O): δ 2.44 (s, 2H, -CHOH-, CH$_2$OH, broad); 1.84-1.87 (m, H, -CHOH-, broad); 0.84-1.26 (m, 2H, -CH_2OH, m, 2H, Pr$_3$N$^+$CH_2-, m, 6H, CH$_3$CH$_2$CH_2-); $^-$0.71-$^-$0.56 (m, 6H, CH$_3$CH_2CH$_2$-); $^-$1.45-$^-$1.38 (t, 9H, CH_3CH$_2$CH$_2$-).

A.5. Polymerizations. Segmented polyurethanes were synthesized by the two-step addition reaction outlined in Figure II-1. All polymers were based on 3/2/1 molar ratios of MDI/chain extender/PTMO. In the first step, a solution of 50% (w/v) MDI in DMAc was added to a stirred 10% (w/v) solution of PTMO in DMAc at 65°C under a dry argon purge. Stannous octoate, 0.15 wt% based on reactants, was then added to catalyze the reaction. After 1 h at 65-70°C, the chain extender was slowly added from a 20% (w/v) solution in DMAc over a 20 min period. 3-dialkylamino-1,2-propanediols were mixed with the corresponding 3-trialkylammonium-(1,2-propanediol)iodide (TAPI) at 0-100 mol% to vary the ionic content of the polyurethanes. Stirring was continued at 80-85°C for 4 h, then at 90°C for 1 h. Non-ionic polymers were precipitated in a 2:1 mixture of deionized water:methanol, then washed with methanol. Polyurethanes chain extended with cationic diols were precipitated in toluene. Polymers were dried 12-18 h in a 65°C convection oven, followed by 2 days in a vacuum oven at 55-60°C. All materials studied have a nominal hard-segment content of 50%.

14
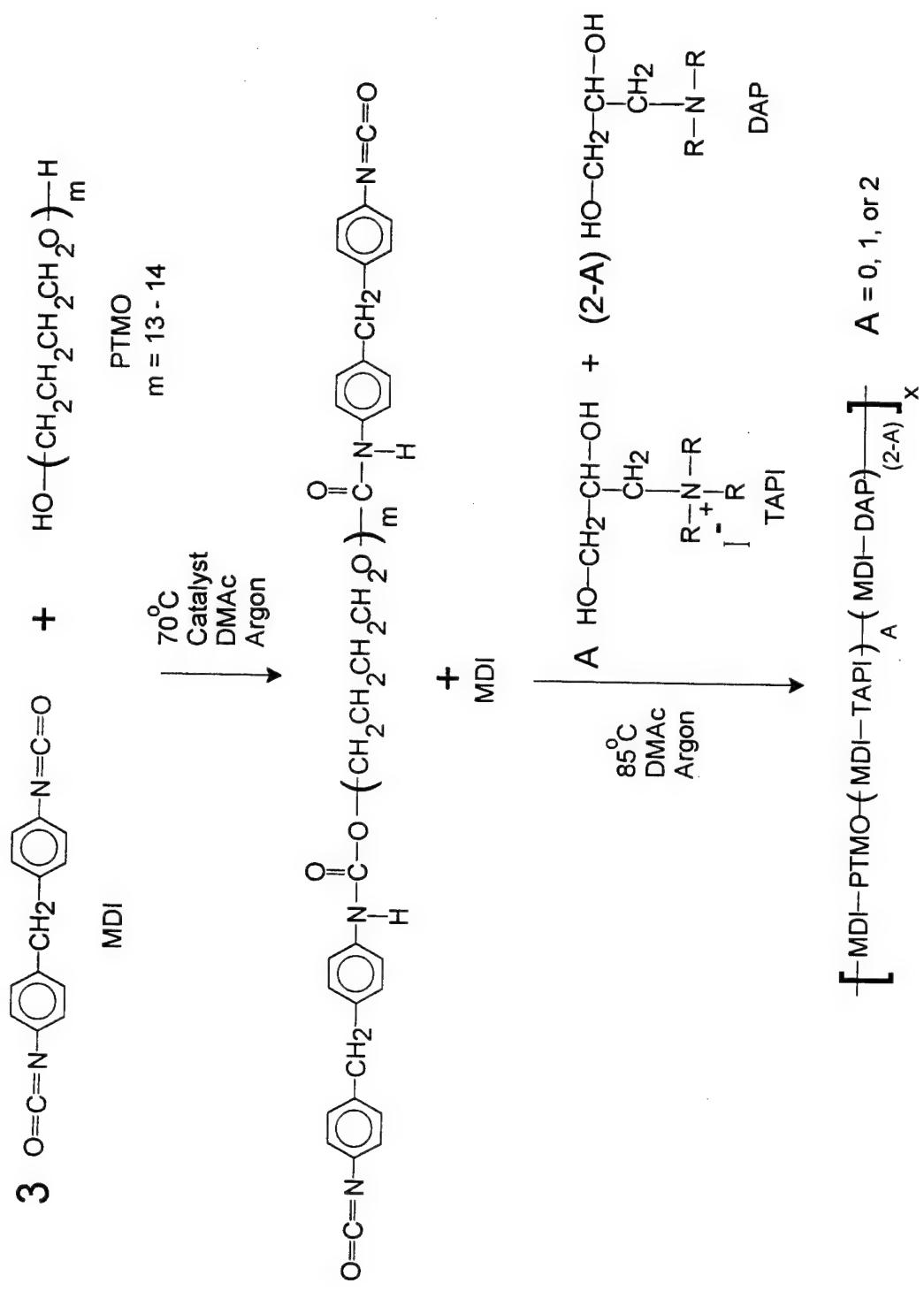
Figure II-1. Two-step synthesis of polyurethane cationomers.

B. Sample Nomenclature

The sample nomenclature used throughout the thesis for the polyurethane cationomers is R-###-X where R represents the alkyl groups on the diol nitrogen (M=methyl, E=ethyl, P=propyl), ### is the mole percent of quaternized amine chain-extender (0, 50, or 100), and X is the halogen anion (I, Br, or Cl) if present. Concentrations of ionic groups ranged from 0.44-0.47 meq/g to 0.82-0.88 meq/g for the R-50-I and R-100-I series, respectively. The sample designated PU-BD is a conventional polyurethane elastomer (Dow Chemical) of MDI/butanediol (BD)/PTMO ($\overline{M_n}$=1000), where the molar ratio of the respective components is also approximately 3/2/1.

C. Ion Exchange

All polyurethane cationomers were synthesized with I^- as the counter-anion. A first attempt at ion exchange was made with a strongly basic ion exchange resin, Amberlyst® A-26 (Aldrich). The polymer E-100-I was dissolved in 2:1 (v/v) toluene:methanol and passed through the resin to replace I^- with OH^-, then neutralized with stoichiometric amounts of 0.1 M HBr, HCl, HF, and H_2SO_4. This procedure proved unsuccessful as all samples (including the OH^- form) became extremely brittle, presumably a result of chain degradation.

Polyurethane cationomers with bromide or chloride counter-anions were successfully prepared via a modified version of a procedure described by Kohjiya et al.[46] About 5 g of polymer E-100-I was dissolved in 50 ml DMAc, then precipitated into 500 ml of a near-saturated solution of sodium chloride or sodium bromide. The

dissolution and precipitation was repeated a second time, followed by repeated washings with deionized water. Exchange efficiencies greater than 99%, with over-neutralization less than 10%, was indicated by elemental analysis (Galbraith Laboratories) for bromide and chloride ions as seen in Table II-1. Since an exchange efficiency of only ~20% resulted with ammonium fluoride or magnesium sulfate, no further characterization was performed on polymers E-100-F or E-100-SO$_4$.

The sample M-100-Br, used only in EXAFS experiments, was polymerized by the procedure given in section A.5 using the chain extender 3-trimethylammonium-(1,2-propanediol)bromide (TMPBr). Even though over-neutralization during ion exchange with NaBr was slight, any excess salt could adversely affect EXAFS results. TMPBr was synthesized via an analogous procedure to A.2, except the reaction was carried out at 5°C for 3 hours, and the quaternization agent was a 2.0 M solution of bromomethane in diethyl ether (Aldrich).

D. Characterization

^{1}H-NMR spectra of synthesized monomers were recorded on a Bruker WP-200 (200 MHz) using tetramethylsilane and methyl sulfoxide as external standards. To prepare samples for tensile testing, differential scanning calorimetry (DSC), thermogravimetric analysis (TGA), infrared temperature studies, and dynamic mechanical thermal analysis (DMTA), polymers were solution cast from anhydrous DMAc into thin films. Most of the solvent was evaporated with dry air at 50°C; residual solvent was removed by placing the films in a vacuum oven at 50-55°C for 4 days, then at room

Table II-1
Ion Exchange Results

Sample	wt% X^a (Theory)	wt% $X^{a,b}$	wt% I^{-b}	ppm Na^{+b}	Percent[c] Excess	Exchange[d] Efficiency
E-100-I	10.82	11.01	--	--	--	--
E-100-Br	7.10	6.65	<0.01	68	<0.1	>99
E-100-Cl	3.28	3.35	0.03	2700	8.2	99
E-100-F	1.78	0.37	8.62	--	--	20
E-100-SO$_4$	1.46	0.62	8.56	--	--	21

[a] X = Halogen ion or sulfur atom after exchange
[b] From elemental analysis
[c] Excess neutralization determined from [wt% Na^+/wt% X (theory)]*100
[d] Exchange efficiency estimated by [(10.82-wt% I^-)/10.82]*100

temperature for 1-3 days. For EXAFS, small-angle X-ray scattering (SAXS), and rheological measurements, each cationomer sample was compression molded for 4 minutes at 60 MPa and a temperature 15-25°C above the location of the highest observed maximum in loss modulus according to DMTA. PU-BD was molded at 200°C to minimize degradation.[47]

D.1.   Tensile testing. Uniaxial stress-strain data were obtained on films approximately 0.2 mm thick using an Instron Model TM at a crosshead speed of 13 mm/min. The Instron was interfaced to a personal computer for automatic data acquisition. Samples were cut using an ASTM D1708 die; results are reported in engineering stress, and are the average of three tests. Standard deviations of Young's Modulus and ultimate properties were within 15% of the average values for all samples.

D.2. Dynamic mechanical thermal analysis. DMTA spectra were collected with a Rheometrics RSA II in autotension mode, with a 120% force for pretension. Temperature steps of 3°C, with a 0.1 min soak time, and a test frequency of 16 Hz, were used over the temperature range of -150°C to 200°C. Test dimensions were approximately 22.5 x 6.3 x 0.2 mm.

D.3. Differential scanning calorimetry. DSC was carried out with a Perkin-Elmer DSC-2C equipped with a Model 3600 data station. The melting points of mercury and indium were used for temperature calibration, with the latter also providing an enthalpy reference. Two scans, from -150° to 200°C under a helium purge, were performed on samples of 17-22 mg at a heating rate of 20°C/min. Samples were immediately quenched to -150°C after the first scan. The glass transition temperature,

T_g, is reported for second scans as the temperature corresponding to the midpoint of the change in heat capacity.

D.4. Thermogravimetric analysis. TGA scans were performed by Betec Laboratory on a DuPont 9900 Thermal Analysis System. Approximately 25 mg of sample was heated in a nitrogen atmosphere at a rate of 3°C/min. This rate is virtually identical to that used in DMTA measurements, although the former is a temperature ramp, while the latter is obtained in small temperature steps.

D.5. Small-angle X-ray scattering. Scattering profiles were collected on a Kratky camera with a Braun Model OED-50M linear position sensitive detector. CuK_α X-rays (wavelength $\lambda = 1.54$Å, E=8042 eV) were generated by an Elliot GX-21 rotating anode, with K_β radiation attenuated by nickel foil. For optimal signal-to-noise, the sample thickness t was selected such that the product μt was approximately equal to one, where μ is the absorption coefficient at 8042 eV. Scattering patterns were corrected for differences in detector sensitivity and linearity along the wire, while a dead time correction was not warranted since total count rates were less than 200 sec^{-1}. Profiles were further corrected for parasitic scattering and sample absorption. Channel-to-angle calibration was determined with a cholesterol myristate sample, and all intensities were adjusted to an absolute basis using a previously calibrated Lupolen standard. Data were desmeared according to the iterative method of Lake[48], as previously described by Register and Cooper.[49] All data are reported as $I/I_e V$ versus q where I is the measured intensity, I_e is the intensity scattered by one electron, and V is the scattering volume. The

scattering vector q is equal to $4\pi\sin\theta/\lambda$, where 2θ is the scattering angle. For general characterization, a sample to detector distance of approximately 60 cm was employed.

For SAXS measurements at elevated temperatures, the cationomer M-50-I was molded into a annular brass ring of the appropriate thickness, and covered on both sides with high-temperature Kapton® tape to minimize thickness changes associated with viscous flow at elevated temperatures. Patterns were obtained at elevated temperatures by heating the sample in a home-built heating cell. Two resistance temperature detectors measured the temperature on either side of the polymer, and control of $\pm 1°C$ was provided by a Proportional-Integral-Derivative (PID) controller tuned to eliminate overshoot. Both t and μt were determined before and after each SAXS profile to monitor possible sample flow and dequaternization at elevated temperatures. In the SAXS temperature studies, the sample to detector distance was decreased to approximately 38 cm to obtain adequate counts in less time. Although the shorter distance also increased the experimental range of q, all profiles were truncated at $q=2.5$ nm^{-1} for consistency with the results of the general characterization.

Electron densities, ρ, for the pure soft and hard-segment of each polymer are summarized in Table II-2, as determined from the equation

$$\rho_{Repeat} = \frac{(Electrons\,per\,Repeat)\,x\,(d_{Repeat})\,x\,A_v}{Repeat\,Mol.\,Wt.} \quad (II-1)$$

where A_v is Avogadro's number. Mass densities, d, of the polymer samples were first measured within 0.003 g/cm^3 by immersion in standards prepared from sodium chloride

Table II-2

Ideal Electron Densities for Soft and Hard Phases

Sample	Repeat Structure	d_{Sample} (g/cm³)	Repeat[a] wt%	d_{Repeat} (g/cm³)	ϕ^c Hard Segment	Repeat Mol. Wt.	Electrons per Repeat	ρ_{Repeat} (e⁻/nm³)
All	-(CH₂)₄-O-	--	-	0.982[b]	---	72.1	40	331
M-100-I	3MDI+2TMPI	1.210	56	1.47[c]	0.46	1273	646	449
M-50-I	3MDI+TMPI+DMP	1.187	53	1.44[c]	0.44	1131	584	448
E-100-I	3MDI+2TEPI	1.200	58	1.42[c]	0.49	1357	694	437
P-100-I	3MDI+2TPPI	1.195	59	1.40[c]	0.50	1441	742	434
PU-BD	3MDI+2BD	1.132	52	1.30[c]	0.45	931	490	412

[a] Determined from stoichiometry

[b] Source: Catalog of Scientific Polymer Products, Inc.; Amorphous PTMO 1000

[c] Calculated from d_{Sample}, $d_{PTMO\ 1000}$, and Repeat wt% assuming no volume change on mixing. The hard-segment is defined as MDI plus chain-extender(s).

and deionized water. The volume fraction, ϕ, and mass density of the hard-segment were then calculated assuming no volume change on mixing.

D.6. Extended X-ray absorption fine structure. Most EXAFS spectra were collected at the Stanford Synchrotron Radiation Laboratory (SSRL), while a few were collected at the Cornell High Energy Synchrotron Source (CHESS). Unless otherwise noted, the data presented in the thesis were collected at SSRL. The same experimental setup was used at both facilities except where noted. The K-edge of bromine ($E_0 = 13474$ eV) was investigated with 5 eV steps in the pre-edge and EXAFS regions, and 2 eV steps between -20 eV below the edge and 60 eV above the edge. Extremely narrow entrance slits (0.2 mm at SSRL, 0.5 mm at CHESS) were used in order to obtain high energy resolution. Energy calibration was performed using the sample M-100-Br, which was molded to the thickness where μt is approximately 2 at E=13574 eV. A 15 cm ionization chamber filled with N_2 and a 30 cm ionization chamber filled with Ar, both at 1 atm, were used to monitor the incoming and outgoing intensities of X-rays respectively. Spectra were collected starting at 25°C and at 20°C intervals thereafter until the sample began to flow on the time scale of the experiment (135°C). Samples were heated in a specially designed cell having a temperature stability of ± 2°C. A total of sixteen scans were taken at each temperature and the scans were coadded (after E_0 determination) before data analysis to improve the signal to noise ratio.

D.7. Fourier transform infrared (FTIR) spectroscopy. Samples for infrared analysis were cast directly onto sodium chloride windows from a 1% (w/v) solution of polymer in DMAc. Film thicknesses were adjusted such that the maximum absorbance

of any band was less than 0.7 to be conservatively within the absorbance range where the Beer-Lambert law is valid.[50] Spectra were acquired on either a Mattson Model GL-5020 (Figures V-5, V-6b, V-9, V-12b, all Figures in Chapter VI) or a Nicolet Model 740 FTIR (all other Figures) spectrometer using a MCT detector at a resolution of 2 cm^{-1}. The number of scans ranged from 64-512. Elevated temperature measurements were obtained by placing the polymer/NaCl sample in a well-insulated homemade temperature cell with resistance heaters and NaCl windows. The temperature was measured at the surface of the sample, and was controlled to within 0.5°C using a PID controller tuned to eliminate overshoot. Samples were maintained at the target temperature for 3 minutes prior to data collection. Additional spectra, taken at times as long as 60 minutes, were essentially identical indicating that 3 minutes was adequate to reach equilibrium conditions.

D.8. Measurement of dynamic viscoelastic properties. The dynamic storage modulus G' and loss modulus G" were determined in a nitrogen atmosphere using a Bohlin VOR Melts-Rheometer in the oscillatory shear mode at temperatures of 60 to 150°C. Sample geometry was defined by 25mm-diameter parallel plates at a gap of approximately 0.5 mm; the gap dimension was corrected for thermal expansion of the apparatus. Measurements were obtained as isothermal frequency scans, at increasing angular frequency ω from about 0.01 to 100 rad/s. Each isothermal scan was conducted at a fixed strain amplitude, well within the linear viscoelastic regime, with strains ranging from 0.05% at 60°C to 9% at 150°C.

E. SAXS Theory and Data Analysis

Small-angle X-ray scattering provides quantitative morphological information on two-phase materials where the domain sizes are on the order of nanometers, and the electron density of the two phases are sufficiently different. Prior to extracting morphological features, background scattering from a variety of contributions (including thermal density fluctuations, inelastic scattering, and the amorphous halo of wide-angle scattering) must be subtracted from the observed scattering profile, I_{obs}. Several empirical methods for subtracting the background scattering, $I_B(q)$, have appeared in the literature. But since most of these require data extending into the amorphous halo, which was not obtained in the present studies, the method of Bonart[51] was selected. In this method, I_B is treated as a constant, and determined from the slope of a plot of $q^4 I_{obs}$ versus q^4. Reasonable linear fits were obtained for cationomers, polyurethanes with the unionized chain extenders, and conventional PUs, as shown in Figure II-2. Hereafter, corrected intensities, $I_{obs}(q)-I_B$, are simply referred to as $I(q)$.

Analysis generally proceeds by either comparing the experimental data with calculated scattering profiles from model structures, or by extracting morphological parameters from the data using a few general assumptions. In the present studies, the latter approach is used. Given the chemical structure of the cationomers under investigation, either a morphology of ionic domains in an amorphous matrix, or a lamellar morphology typical of conventional PUs might be anticipated. Although electron micrographs were not successfully obtained, results presented in Chapter III provide
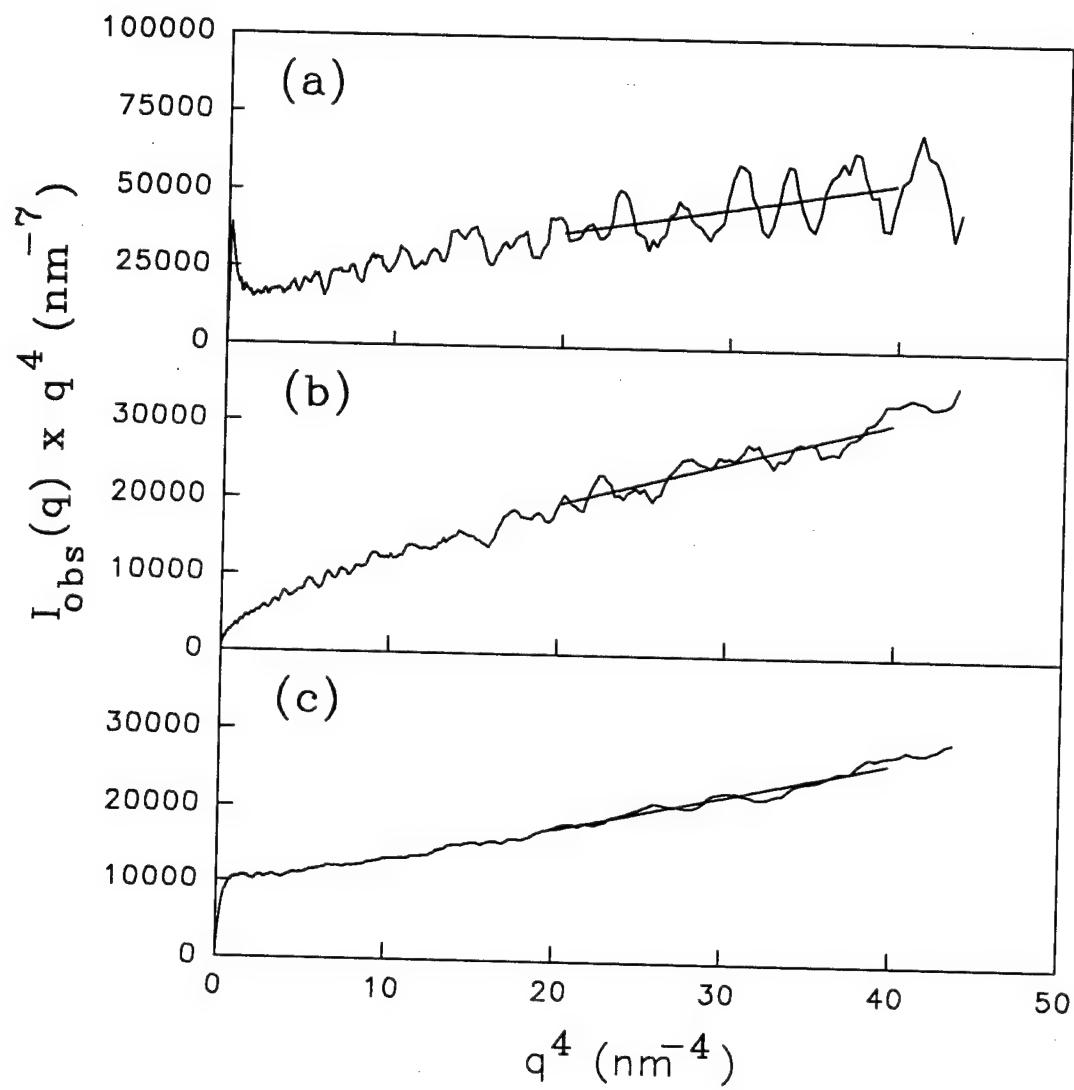
Figure II-2. Typical plots for SAXS background subtraction via the method of Bonart:
(a) M-100-I; (b) M-50-I; (c) PU-BD.

strong evidence that the PU cationomers have a lamellar morphology. All subsequent SAXS analysis, where model dependent, is therefore based on a lamellar model.

Although derived for scattering from discrete crystal planes, Bragg's law is often used to approximate the interdomain spacing, d, of less ideal systems. Bragg's law has the form[52]

$$d = \frac{2\pi}{q_{max}} \qquad (II-2)$$

where q_{max} is the value of q at the first local maximum in intensity. For a lamellar geometry, the intensity I(q) is weighted by the factor q^2 to calculate a Bragg spacing. The average interlamellar distance can also be obtained from the position of the first maximum in the one-dimensional correlation function, $\gamma(x)$, as developed by Vonk.[53,54] The correlation function represents the probability that a rod of length x will have both of its ends in domains with the same electron density, and is given by the equation

$$\gamma(x) = \frac{\int_0^\infty q^2 I(q) \cos(qx)\, dq}{\int_0^\infty q^2 I(q)\, dq} \qquad (II-3)$$

The integral in the denominator of Equation II-3 is related to the invariant, Q. The invariant depends only on the mean-square fluctuation of the electron density within a material, $\overline{\Delta\rho^2}$, as follows[55,56]

$$\frac{Q}{V} = \int_0^\infty q^2 I(q)\, dq = 2\pi^2 \overline{\Delta\rho^2} \qquad (II-4)$$

For an ideal two-phase system, with sharp interfaces and constant electron densities ρ_1 and ρ_2 within each domain, the mean-square electron density fluctuation can be calculated from the equation[14,51]

$$\overline{\Delta\rho^2}_{id} = \phi_1\phi_2\,(\rho_1-\rho_2)^2 \qquad\qquad (II-5)$$

where ϕ_1 and ϕ_2 are the volume fractions of each phase. The ratio $\overline{\Delta\rho^2}/\overline{\Delta\rho^2}_{id}$ provides semi-quantitative information on the degree of phase separation in a system, with limiting values of 0 and 1 corresponding to complete and no phase mixing, respectively.

For calculation of the integral in Equation II-3, $I(q)$ must be extrapolated both below (to $q=0$) and above (toward $q=\infty$) practical instrumental limits. In the region $q=0$ to 0.1 nm^{-1}, extrapolation according to Guinier's law[57] was assumed:

$$\lim_{q\to 0} I(q) = I(0)\,e^{-\frac{R_g^2 q^2}{3}} \qquad\qquad (II-6)$$

where $I(0)$ is the scattered intensity at zero angle, and R_g is the radius of gyration of the scattering body. Guinier's law was derived for isolated particles, whereas the PUs of the present studies represent a dense system. R_g was therefore treated only as a parameter for extrapolation, with no physical significance. Plots of $\ln[I(q)]$ versus q^2 displayed slight curvature throughout the low q^2 regime as shown in Figure II-3, and thus experimental data at the smallest scattering vectors were selected for fitting Guinier's law.
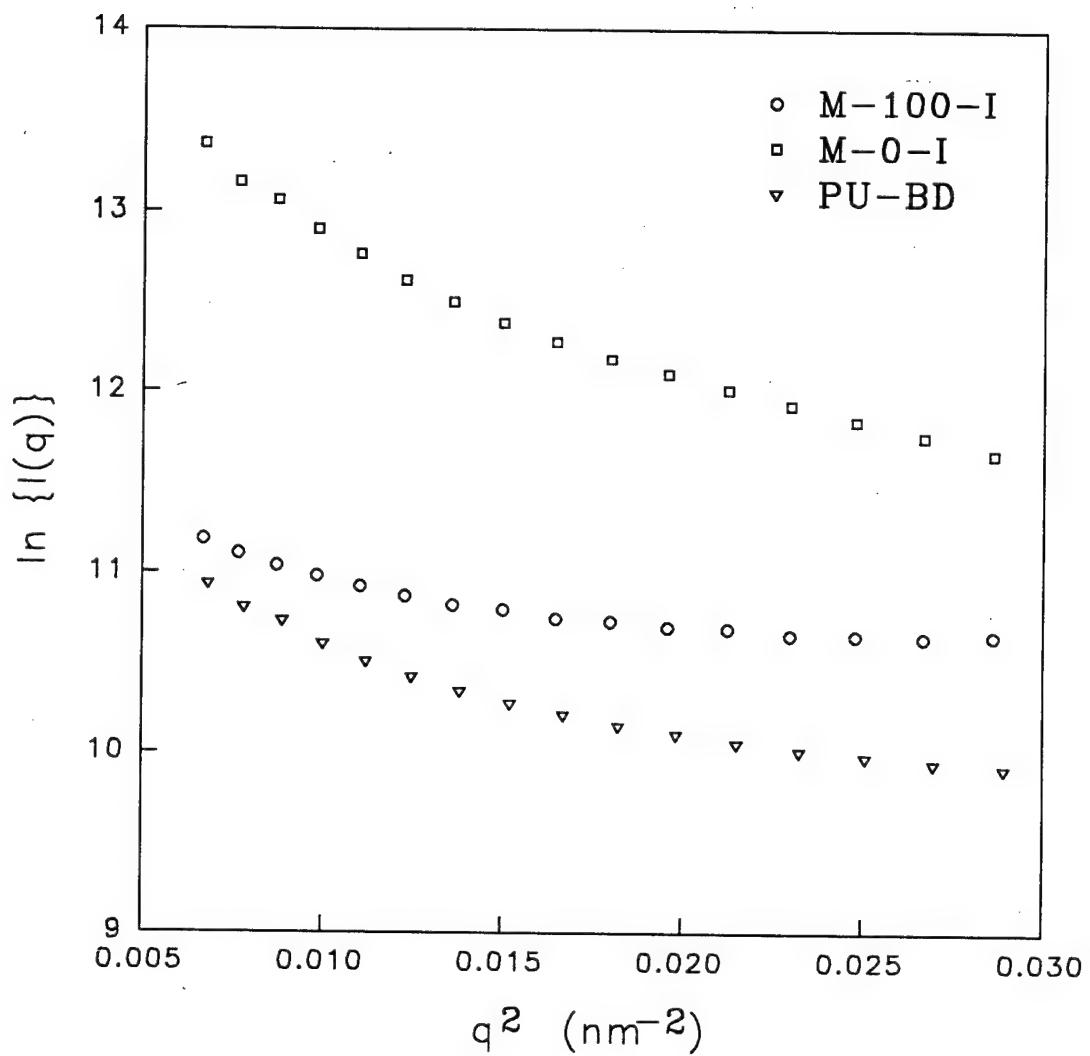
Figure II-3. Guinier plots used in the extrapolation of experimental data to q=0.

For an ideal two phase system, Porod[55,56] showed that the scattering at large vectors could be described by the relationship

$$\lim_{q \to \infty} I(q) = \frac{K_p}{q^4} \tag{II-7}$$

Porod's law predicts that the product $I(q)q^4$ reaches a constant, K_p, as $q \to \infty$. However, this is not observed in most real polymer systems. As reviewed by Tyagi et al.,[17] positive deviations from Porod's law (a positive slope in a plot of $I(q)q^4$ versus q^2 or q) can be attributed to thermal density fluctuations or phase mixing. On the other hand, the presence of interfaces between phases results in negative deviations. In the present studies, deviations led to some uncertainty in the determination of Porod's constant, and consequently in the extrapolation of experimental data in the range q=2.5 to 50 nm^{-1} using Equation II-7. However, because of the large area under the interference peak of the SAXS patterns, both the correlation function and the invariant were relatively insensitive to errors in Porod's or Guinier's constants. For example, deviations from mean values of only $\pm 15\%$ in Q and $\pm 2\%$ in the position of the first maxima in $\gamma(x)$ resulted when varying K_p from 0 to 2 times its assumed value.

F. EXAFS Theory and Data Analysis

EXAFS is the measure of oscillations in the absorption coefficient, μ, about its mean value at energies between 50-1000 eV above an atomic absorption edge. An absorption edge occurs when the X-ray energy is sufficient to cause the ejection of a photoelectron; the K-edge corresponds to the ejection of a 1s electron. Oscillations occur

because the outgoing photoelectron wave can be back-scattered by neighboring atoms, which leads to interference between the outgoing and back-scattered waves. Qualitatively, the shape and period of the oscillations will be a function of the absorbing atom as well as the type, distance and number of back-scattering atoms.

The simplest correct theoretical description of this phenomena was originally developed by Stern et al.[58] and has been labelled single-electron single-scattering theory. This theory assumes that multiple scattering events are unimportant and that disorders, both thermal and static, are small. The fundamental equation from this theory is

$$\chi(k) = \frac{\mu(E) - \mu_0(E)}{\mu_0(E)}$$

$$= \sum_j N_j \, S_o^2(k) \, \frac{F_j(k)}{kr_j^2} e^{-2\sigma_j^2 k^2} e^{\frac{-2r_j}{\lambda_j}} \sin[2kr_j + \phi_{ij}(k)] \tag{II-8}$$

where $\mu(E)$ and $\mu_0(E)$ are the measured and mean absorption coefficients, respectively, at the energy E; N_j is the number of atoms of type j in the jth shell; $S_0^2(k)$ is the amplitude reduction factor which is due to excitations of electrons other than 1s electrons (for a K-edge) in the absorbing atom; $F_j(k)$ is the back-scattering amplitude from the N_j atoms; r_j is the root mean square distance between the central atom and the jth atom; σ_j is the Debye-Waller factor which measures the variation in r_j about its mean; λ_j is the electron mean free path; and ϕ_{ij} is the phase shift experienced by the photoelectron, which is a function of both the absorbing i atom and back-scattering j atom. k is called the wavevector because $2\pi/k$ is the wavelength of the ejected photoelectron. Through a

simple energy balance it can be shown that

$$k = \sqrt{\frac{2m_e}{h^2}(E-E_0)} \qquad \qquad (II-9)$$

where E_0 is the absorption-edge energy, m_e is the mass of an electron, and h is Planck's constant divided by 2π. Generally, F(k) and $\phi_{ij}(k)$ are a function of only the central and back-scattering atom and can be calculated either theoretically[59,60] or from model compounds. λ_j can also be calculated either theoretically or from model compounds. Hence, four parameters are usually unknown for each coordination shell: E_0, r_j, N_j and σ_j. Although E_0 can be identified from a μt vs E plot, generally E_0 should be allowed to vary to correct for errors in energy calibration and phase transferability.[61] The k dependence of the amplitude reduction factor is usually quite small and for the purposes of this thesis, the factor will be treated as a constant. When comparing experimental data with the same absorbing atom, the amplitude reduction factor was assumed to be identical for the two samples, which is generally an excellent assumption. This factor is necessary to accurately simulate the experimental data with FEFF5®. Typically, each shell is analyzed individually as will be described.

Two commercially available software packages were used for data analysis. BAN®, available from Tolmar Instruments, was used for converting the measured μt vs E curve to $k^2\chi(k)$ vs k, subsequent Fourier transformation, isolation of each shell, back-transformation, and determination of the four unknown EXAFS parameters. This software uses the ratio method[61] to calculate N/N_{ref}, $E_0-E_{0,ref}$, $\sigma^2-\sigma_{ref}^2$ and $R-R_{ref}$ where the subscript 'ref' represents the value from a reference compound. FEFF5,[62] available from

the University of Washington, was used to theoretically calculate EXAFS spectra on the basis of the hypothesized atomic coordinates, and the resulting values for the amplitude and phase functions were used with the BAN software in addition to values from model compounds.

G. FTIR Data Analysis

Prior to quantitative analysis, three different complications in the raw infrared spectra necessitated correction: i) contributions from water vapor, ii) extraneous background absorbance, and iii) changes in sample thickness.

Spectral features attributable to water vapor were evident in some of the data taken at elevated temperatures in spite of the careful drying technique employed. The presence of water is a concern, since it would complicate interpretation of the results if its source were water absorbed in the polymer. Water retention in polyurethanes is well known, and the extreme hydrophilicity of the polyurethane cationomers used in this thesis is noted in Chapter IV. However, we strongly believe that the source was absorbed/adsorbed water on components of the heating cell, as water vapor was also evident in spectra obtained at elevated temperatures without a polymer sample. Contributions from water vapor were removed via spectral subtraction. The optimum multiplication constant, ξ, for subtraction of the water component in a given region of interest was determined with a Fortran program which varied ξ so as to minimize the sum of the absolute difference in

absorbance between successive points. The sum of the differences is given by S_{suc} in Equation II-10,

$$S_{suc} = \sum_i \left| A_{corr}(v_{i+1}) - A_{corr}(v_i) \right| \qquad (II-10)$$

where the corrected absorbance is given by $A_{corr}(v_i) = A_{raw}(v_i) - \xi \times A_{water\ vapor}(v_i)$. Figure II-4 shows a typical spectrum before and after subtraction of the water vapor contribution.

Extraneous background absorbance can greatly compromise quantitative infrared studies, since any baseline subtraction is an approximation. For this reason only excellent quality spectra, where the baseline was either constant or linear with a slight slope, were retained. All spectra displaying quadratic or higher-order base absorbance were rejected. A linear baseline was subtracted from each spectrum as defined by regions where negligible absorbance occurs; specifically a least squares fit of data between 3800-3700 cm^{-1} and 2300-2200 cm^{-1} was performed.

The final correction to raw spectra was normalization of absorbances for varying sample thickness. This is necessary to compare results obtained on different polymers, since all samples were not of the same thickness. Further, the thickness of a given sample usually changed during the course of heating and cooling experiments as a result of viscous flow. To correct for varying sample thickness, the ordinate of all spectra and all reported areas have been normalized to the integrated area between 2980-2820 cm^{-1}. This frequency range contains the strongest of the bands between 3100 and 2700 cm^{-1}
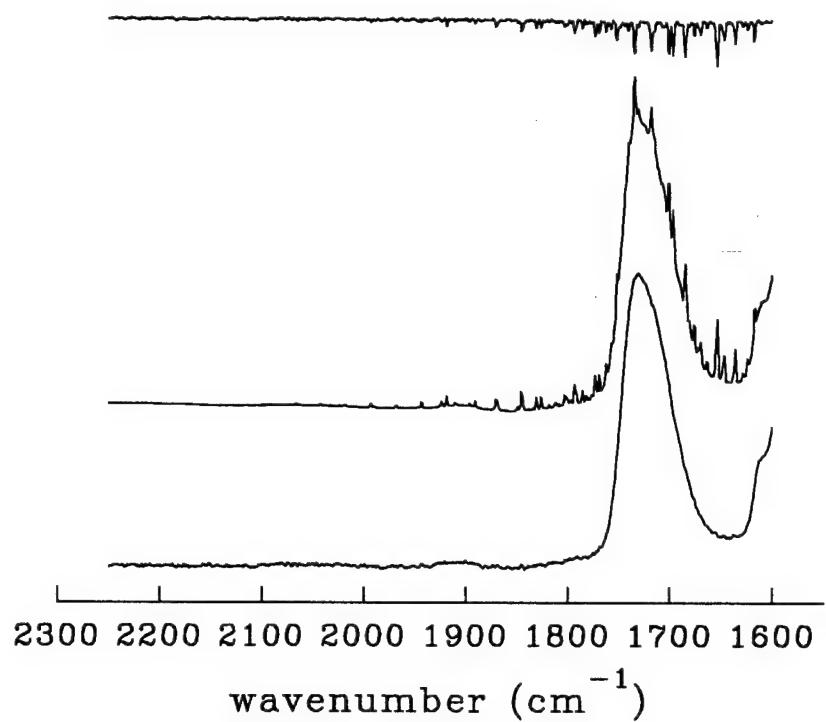
Figure II-4. Representative spectrum before (middle) and after (bottom) subtraction of the water vapor contribution (top).

which are associated with symmetric and asymmetric stretches of aliphatic CH_2 groups. The selection of band(s) for normalization is arbitrary; any region in which the band(s) shape and intensity changes negligibly with temperature could be used. Typical results such as those shown in Figure II-5 support the present method of thickness compensation. First, we see that nearly identical results are obtained using a second band to monitor thickness, namely the peak absorbance of the aromatic C-C stretch at 1412 cm^{-1}. Agreement of the two methods suggests a maximum relative error of approximately 2% in this step of data processing, an error that is negligible relative to assumptions employed later in band deconvolution. Figure II-5 also indicates that there is no thickness change for M-100-I below approximately 130°C, while M-0-I undergoes viscous flow starting at room temperature. The onset of flow seen during infrared scans of the two materials are thus entirely consistent with the dynamic mechanical spectra shown later in Chapter III.
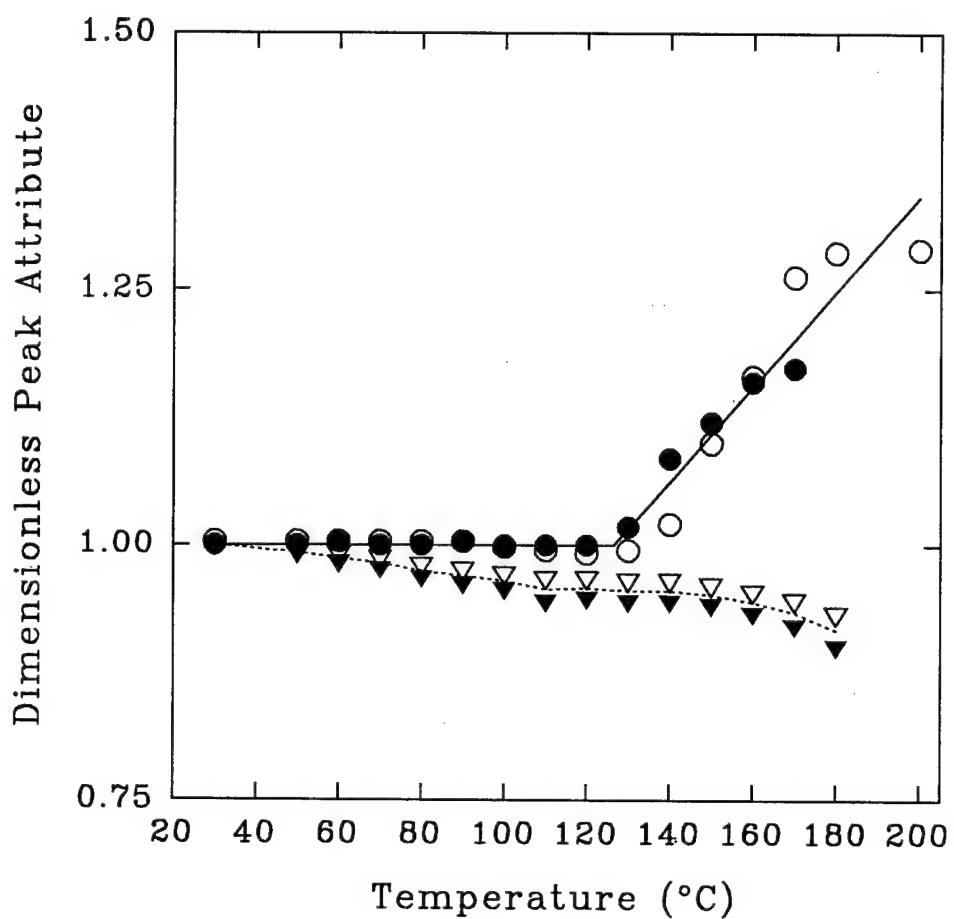
Figure II-5. Thickness corrections for viscous flow during FTIR heating experiments of samples M-0-I (triangles) and M-100-I (circles). Hollow symbols are the integrated area of the C-H stretching region, and filled symbols are the maximum absorbance of the band assigned to aromatic C-C stretching. A value of 1 was assigned to 30 °C.

Chapter III. Effects of Ion-Related Variables

on Microstructure and Physical Properties

A. Introduction

In Chapter II, the synthesis of PU cationomers with pendant trialkylammonium groups using ionic chain-extenders was described. Quaternization of the diols prior to polymerization offered two advantages. First and most important, for some of the quaternizations, reaction conditions were employed which would have likely degraded the polyurethane if the quaternization had been carried out after polymerization. Secondly, separation of the ionic monomer from the starting diol allowed precise control of the ion content. In this chapter, the morphology and properties of the PU cationomers are discussed as a function of ion content, alkyl group length, and neutralizing anion.

B. Results and Discussion

B.1. Dynamic mechanical thermal analysis. The effect of increasing ion content and alkyl group on dynamic mechanical properties is illustrated in Figures III-1 to III-3 with transition data summarized in Table III-1. T_β, which represents the glass transition temperature of the soft segment, and T_γ, attributed to motion of the methylene sequences in the polyether soft segments, were defined by the local maxima in the loss modulus E". The upper α-transition did not result in a maxima in E" for all samples; therefore, T_α was defined as the temperature at which the storage modulus E' decreased to one-third of the value predicted by linear extension of the rubbery plateau. For
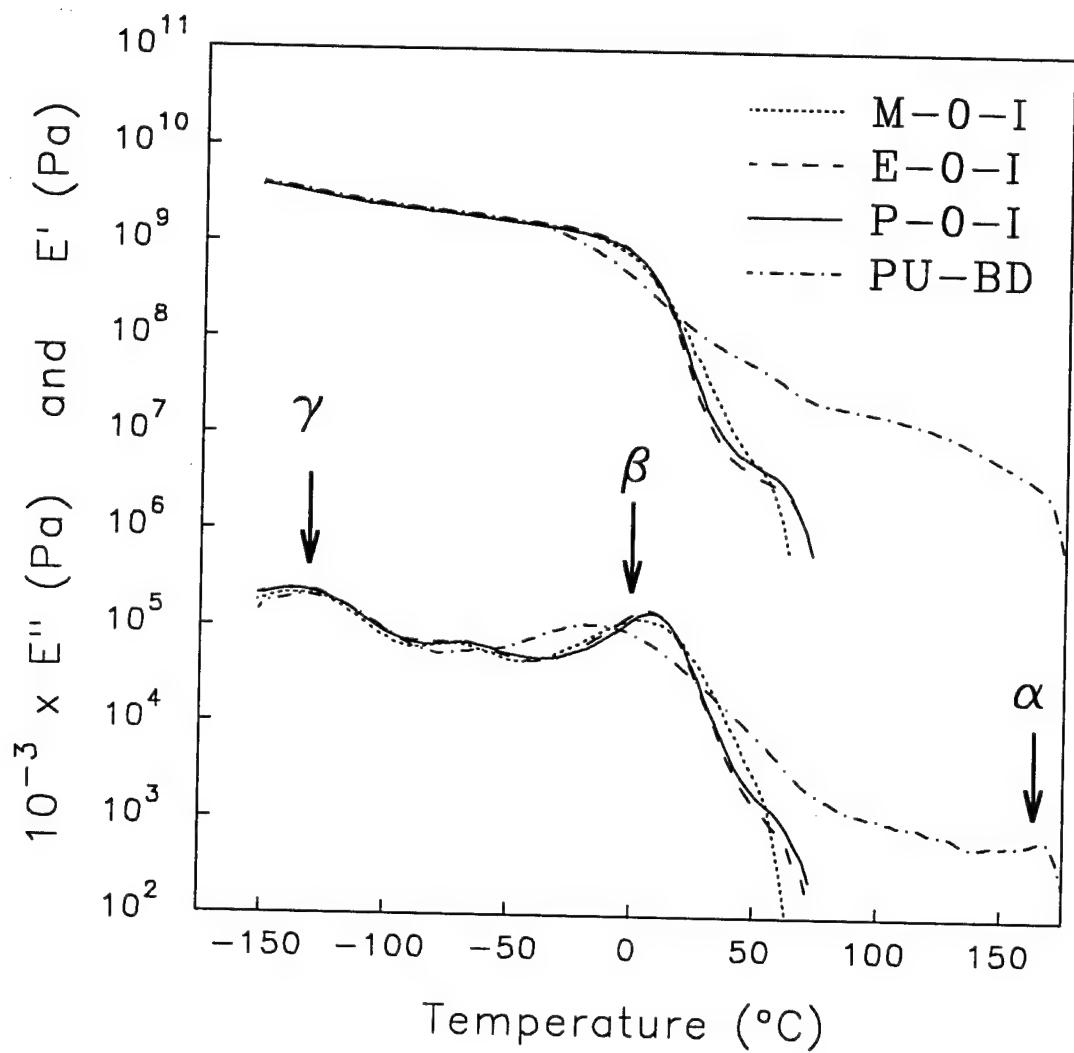
Figure III-1. E' and E" for the unquaternized polyurethanes and the conventional polyurethane PU-BD.
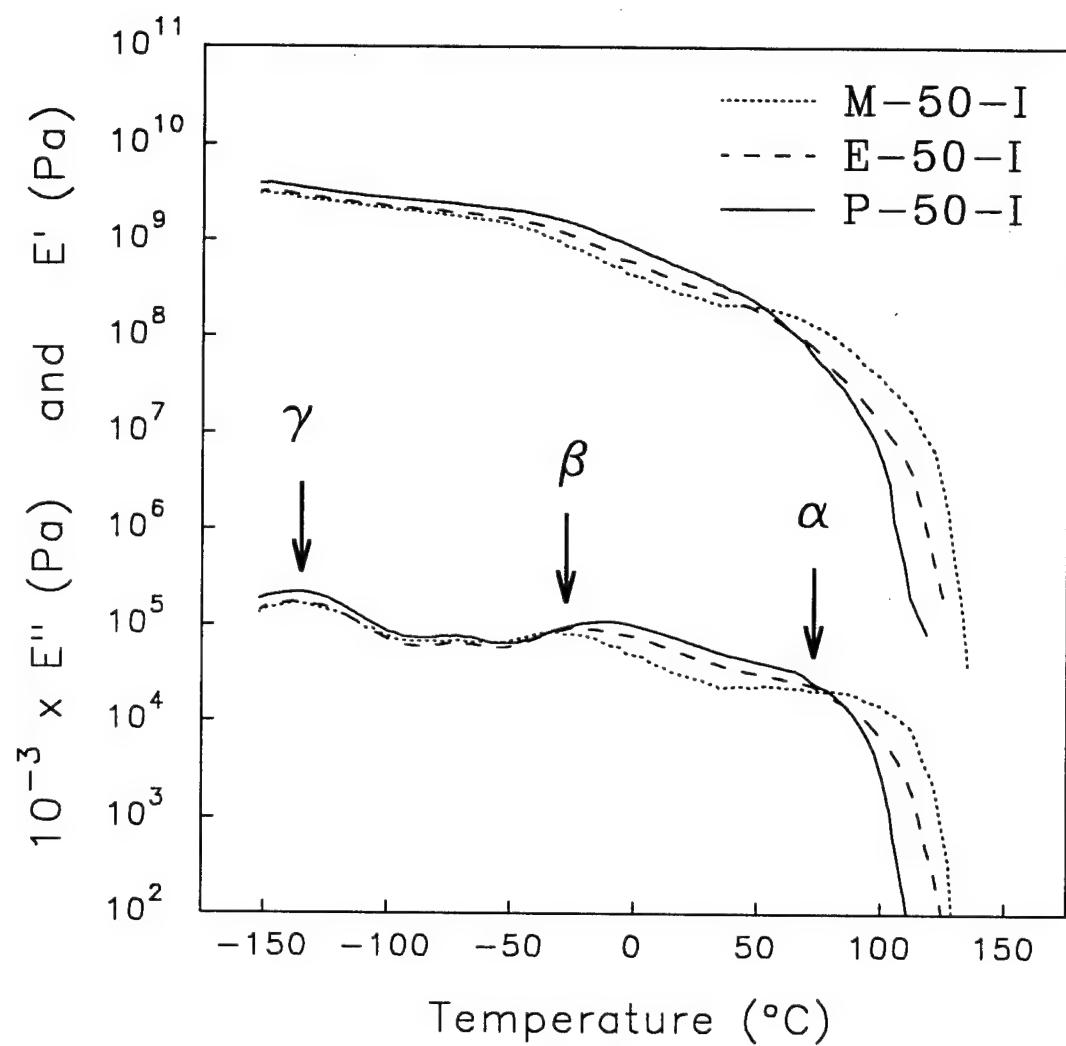
Figure III-2. E' and E" for polyurethane cationomers chain extended with a blend of 50% TAPI and 50% DAP.
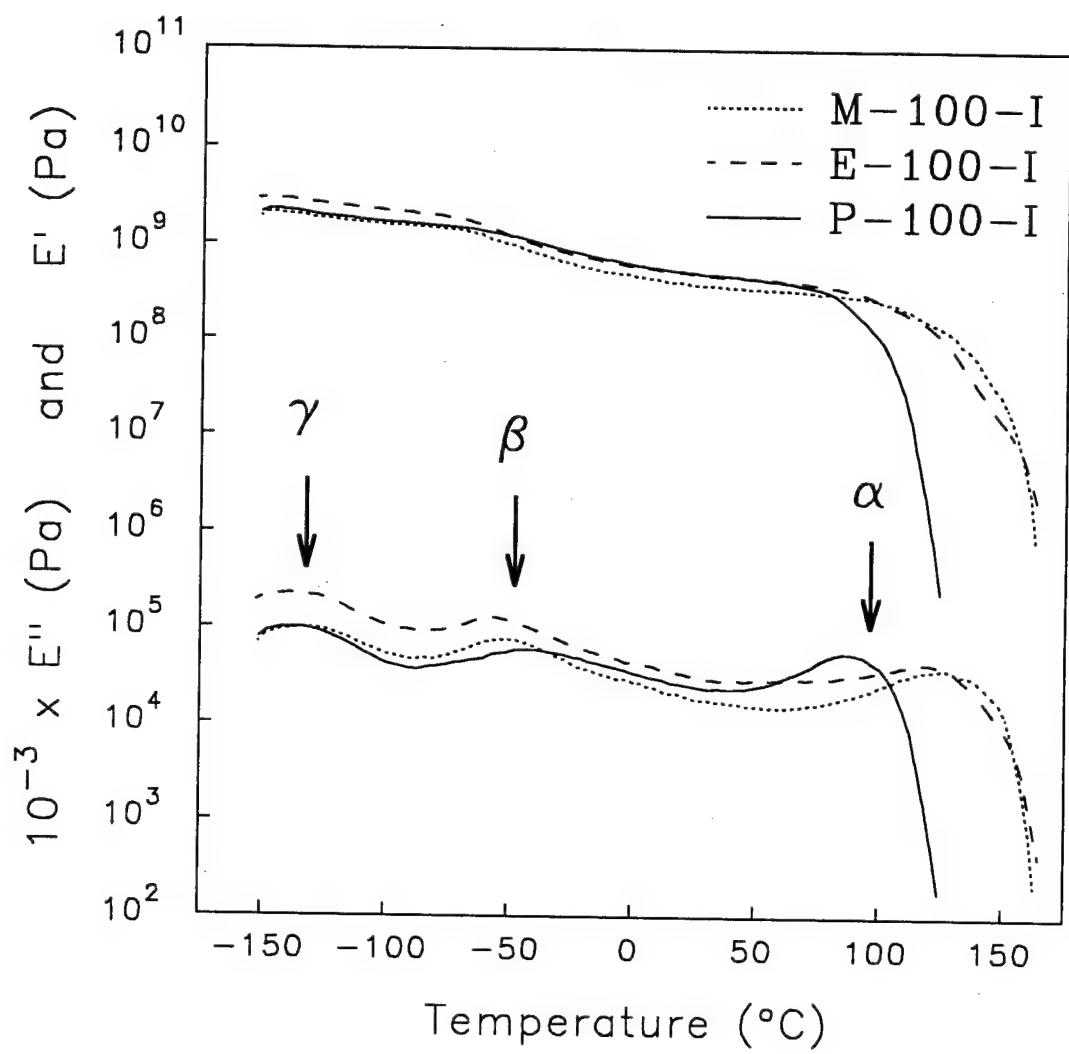
Figure III-3. E' and E" for fully quaternized polyurethane cationomers.

Table III-1
Thermal Transition Data

Sample	DMTA Results			DSC Results
	T_γ (°C)	T_β (°C)	T_α (°C)	T_g (°C)
M-100-I	-133	-52	129	-56
M-50-I	-134	-30	86	-40
M-O-I	-137	4	---	-2
E-100-I	-137	-56	113	-58
E-50-I	-138	-23	76	-33
E-O-I	-138	1	---	-4
P-100-I	-134	-40	92	-52
P-50-I	-137	-13	65	-28
P-0-I	-137	9	---	0
E-100-Br	-136	-57	108	-58
E-100-Cl	-136	-57	119	-62
PU-BD	-133	-18	167	-27

samples that displayed a local maxima in E" at the α-transition, temperatures acquired via the two methods agreed within 3°C.

In the conventional polyurethane PU-BD, phase separation of the MDI/BD hard segments and PTMO soft segments results in a rubbery plateau between approximately -30°C and 160°C. The lower end of this plateau is marked by the glass transition temperature (T_g) of the soft segment with some fraction of dissolved hard segments, while the rubbery plateau ends at T_α with melting of the semi-crystalline hard segments. DMTA spectra of the unionized polyurethanes chain-extended with DAP, shown in Figure III-1, do not exhibit a rubbery plateau or α-transition. In these materials, the bulky pendant amino groups are asymmetric and lack stereoregularity. Crystallization of the hard segments is thus prevented, and the polymers are primarily a mixed hard segment-soft segment one-phase material. Disruption of hard-segment crystallization and phase mixing on addition of pendant groups to the hard segments has been noted in other polyurethanes.[63,64] The glass transition of the R-0-I polymers, T_β = 1-9°C, is intermediate between the T_g of pure PTMO 1000 ($\approx$-70°C) and the T_g of a MDI/DAP hard-segment polymer ($\sim$60°C). For the unquaternized materials, T_γ is constant for all alkyl groups; and T_β shows no clear trend with alkyl group length, varying by only 8°C throughout the series.

As shown in Figure III-3, quaternization of the amino group leads to a two-phase morphology. This is evidenced by a shift of the β-transition to lower temperatures, and the establishment of the higher temperature α-transition. A comparison of T_β's and slopes of the rubbery plateaus for PU-BD and the R-100-I polymers shows that ionic

interactions not only provide the driving force for phase separation in these PU cationomers, but also result in less phase mixing than observed in the conventional PU with the same soft-segment type and molecular weight. T_γ is unaffected by ionization, and is not a function of the alkyl group. In contrast, T_α was found to increase in the order M-100-I > E-100-I > P-100-I, while the soft-segment glass transition temperature decreases in the order E-100-I ≈ M-100-I < P-100-I.

Behavior of the R-50-I polymers, as shown in Figure III-2, is intermediate between that of the fully ionized and unquaternized materials. The storage modulus in the 50% ionized polymers is extended to higher temperatures than in the R-0-I series, but the rubbery plateau is ill-defined, and the α-transition temperatures are well below those of the R-100-I series. Although the R-50-I polymers are two-phase materials, phase mixing is considerably greater than in the R-100-I series as evidenced by a broadening and shift to higher temperature of the β-transition when the ion content is decreased. Phase separation in the 50% ionized materials, as estimated from T_β and the slope of the rubbery plateau, is comparable to that of PU-BD. Trends of T_α and T_β with alkyl group were similar to those observed in the R-100-I polymers; the temperature of the α-transition again increased in the order M-50-I > E-50-I > P-50-I, and T_β decreased in the order M-50-I < E-50-I < P-50-I. These results suggest that ionic interactions are weakest in the R=propyl cationomers, both in terms of the upper temperature limits of the rubbery plateaus, and the degree of phase separation. In fact, the strength of the ionic interactions generally follow the order R=methyl > R=ethyl > R=propyl, with the exception that comparable phase separation is observed in samples E-100-I and M-100-I.

However, in these latter samples complete phase separation is approached, and detection of differences is therefore difficult. A decrease of ionic interaction strength with increasing alkyl chain length likely results from a combination of steric hindrance and charge delocalization by the alkyl groups.

The soft-segment glass transition temperature is not affected by the type of counter-ion for the anions tested as shown in Figure III-4. On the other hand, the temperature of the α-transition increases in the order $Cl^- > I^- > Br^-$, though the total span in T_α for the three samples was only 11°C. This difference is not attributable to errors in measurement as it was observed in repeated DMTA spectra, but might be a result of the ion exchange procedure. Excess NaCl in the sample E-100-Cl (Table II-1) would likely extend the rubbery plateau to higher temperatures, and therefore mask any subtle trend with electronegativity or ionic radius if it existed.

B.2 Differential scanning calorimetry. DSC thermograms for the M-###-I series of PU cationomers and PU-BD are provided in Figure III-5, with thermal transition data for all polymers given in Table III-1. The commercial polyurethane PU-BD displays a soft-segment T_g near -30°C, followed by a series of melting endotherms for semi-crystalline hard-segments with varying degrees of order. In contrast, the only feature observed in the unquaternized material is a mixed hard segment-soft segment glass transition temperature at -2°C. This transition is coincident with T_β of DMTA spectra in R-0-I polymers. Upon complete ionization, phase separation dramatically improves as seen by the shift of the soft-segment T_g to -56°C in the sample M-100-I. The change in heat capacity at T_g is considerably less in M-100-I than in M-0-I, as phase separation
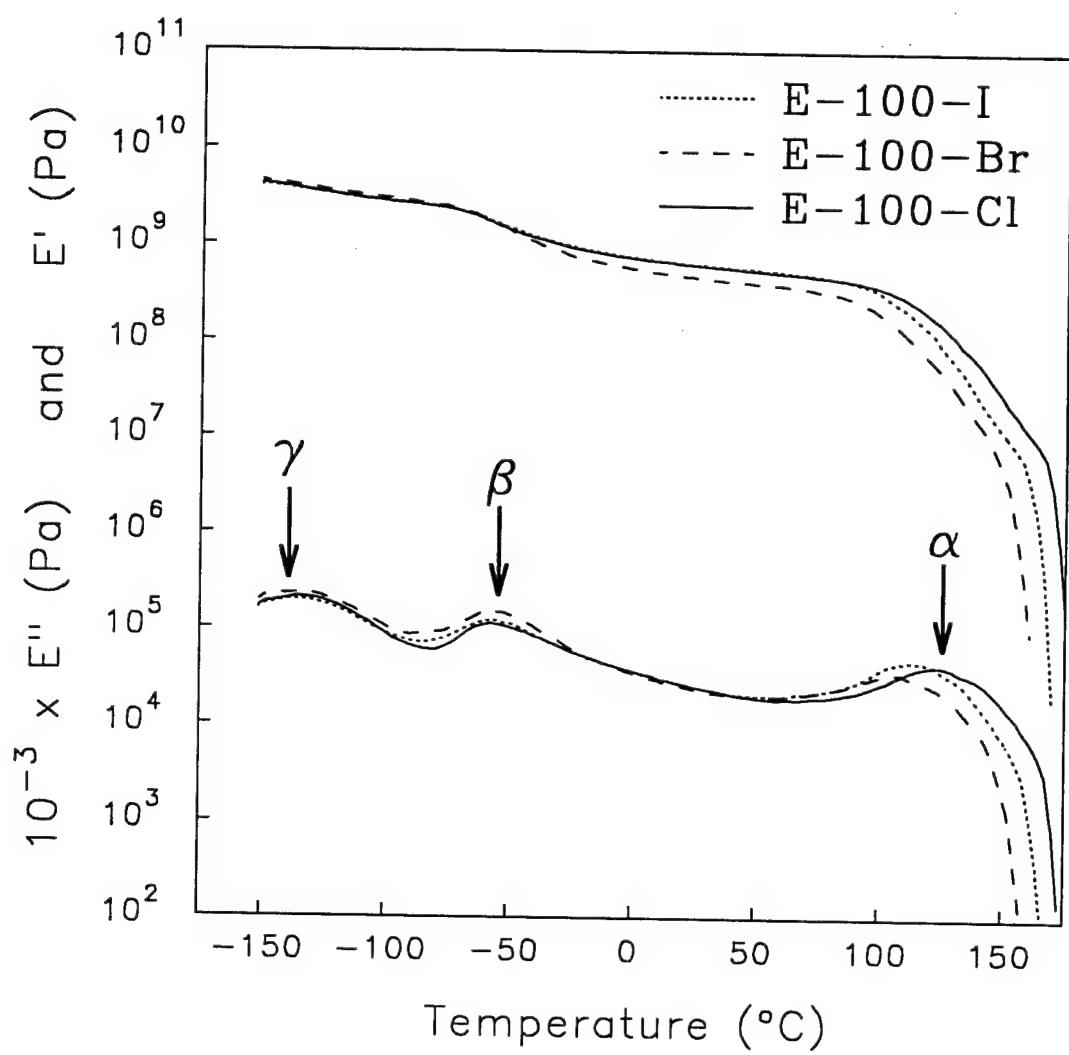
Figure III-4. E' and E" for cationomers E-100-X as a function of neutralizing anion. Polymers E-100-Br and E-100-Cl were prepared from the starting material, E-100-I, by ion exchange.
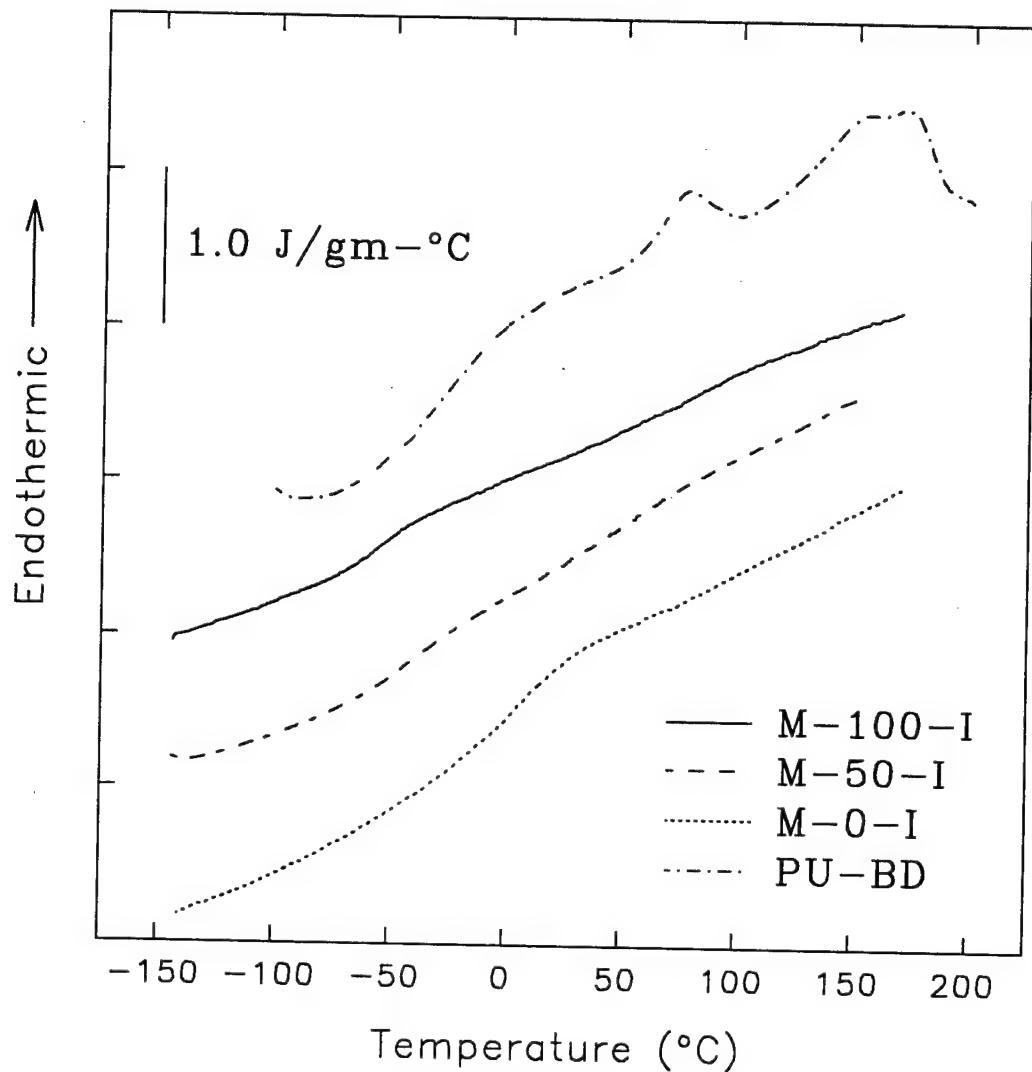
Figure III-5. DSC results for PU-BD and the R=methyl series of polyurethane cationomers. Curves are typical of the R=ethyl and R=propyl series.

reduces the weight fraction of material associated with the transition by approximately one-half. At 50% quaternization, the T_g of the soft-segment is intermediate between that of the unquaternized and fully ionized cationomers. Additionally, phase mixing in the polymer M-50-I results in a glass transition that is subtle and broad, much like the β-peak in DMTA spectra of the same material. The above general descriptions of DSC thermograms as a function of ion content are the same for the R=ethyl and R=propyl series of polymers. At each level of quaternization (0%, 50%, and 100%) the trend of T_g with alkyl group is identical to that discussed for T_β. Finally, and again consistent with DMTA results, the soft-segment T_g is nearly independent of the neutralizing anion.

Unlike PU-BD, high temperature melting endotherms are not observed in any of the PU cationomers, which provides further evidence that the pendant groups of TAPI and DAP prevent hard-segment crystallization. In fact, DSC scans of R-100-I and R-50-I show no evidence of any thermal transition corresponding to the α-transition of DMTA spectra. The absence of a transition is not surprising since amorphous PUs often show no evidence of a hard segment T_g, and ionic transitions have seldom been observed in DSC thermograms.

B.3. Tensile testing. Stress-strain curves for the M-###-I series of cationomers and PU-BD are shown in Figure III-6, with tensile property data for all polymers summarized in Table III-2. At a given ion content, the general response to uniaxial deformation seen in Figure III-6 is also observed in the R=ethyl and R=propyl materials. At 0% quaternization, the mixed hard segment-soft segment copolymers are adhesive-like materials with a meager Young's modulus. The DMTA spectra of the R-0-I materials
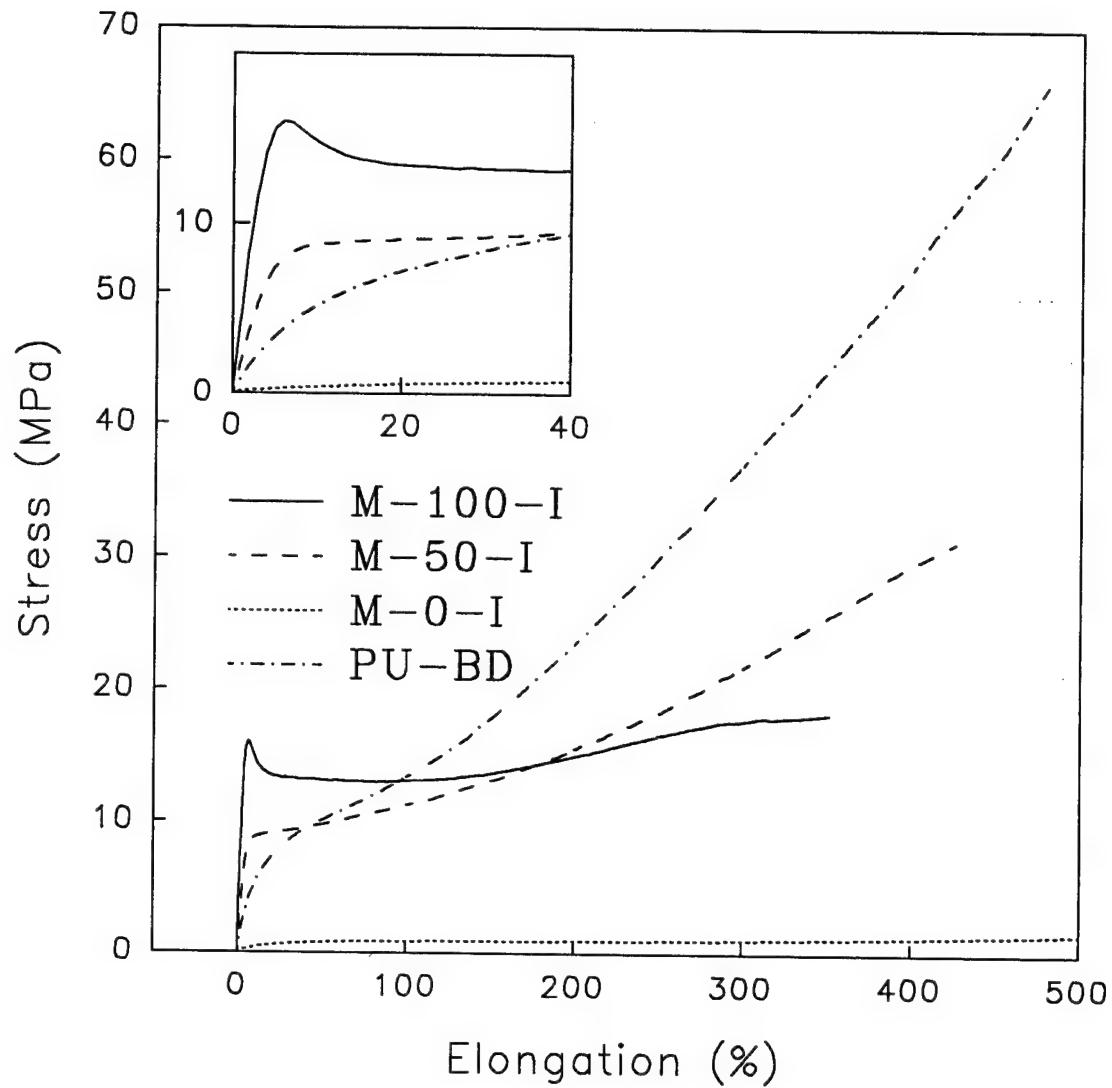
Figure III-6. Stress-strain curves for PU-BD and the R=methyl series of polyurethane cationomers. Curves are typical of the R=ethyl and R=propyl series.

Table III-2
Tensile Properties

Sample	Young's Modulus (MPa)	Tensile Strength (MPa)	Ultimate Elongation (%)
M-100-I	430	18	350
M-50-I	190	31	430
M-O-I	9.1	4.3	810
E-100-I	480	35	390
E-50-I	200	37	490
E-O-I	3.1	0.1	>1000
P-100-I	520	22	310
P-50-I	260	41	440
P-0-I	7.1	0.4	>1000
E-100-Br	380	36	460
E-100-Cl	480	31	260
PU-BD	85	66	480

show that at room temperature the polymers are above their β-transition, and in a region of highly viscous flow. As such, chain entanglements provide the primary resistance to deformation. The low and near-horizontal stress seen in the unquaternized materials, which in E-0-I and P-0-I extended beyond 1000% without sample failure, is consistent with chain disentanglement. As seen from the data of Table III-2, no clear trends between alkyl group length and any of the tensile properties are observed in the unquaternized materials.

Quaternization dramatically increases the tensile properties of the PU cationomers. Copolymers chain-extended with 50% TAPI/ 50% DAP display elastomeric behavior similar to PU-BD. However, the modulus of the R-50-I cationomers is 2-3 times greater than that of the conventional PU, while the tensile strength of the cationomers is lower by a factor of 2-4 at comparable ultimate elongations. The differences in the stress-strain curves of the 50% ionized materials and PU-BD are likely attributable to the response of the hard domains to deformation, since the PUs contain identical soft segments, equivalent volume fractions of each phase (Table II-2), and similar degrees of phase separation as determined from the soft-segment T_g's. A number of previous investigations have shown that ionic[38,63-65] or coordination[66] interactions in PUs provide greater hard domain cohesion than found in typical urethanes like PU-BD. This would account for the higher modulus observed in the R-50-I series, while the greater cohesion may also reduce the ability of the hard segments to respond to stress without failure, thus lowering the ultimate strength. Rearrangement and orientation of hard segments in the direction of stress

has been shown to play an important role in the high-strain response of PUs with semi-crystalline hard segments.[3,67-69]

Further evidence of this is provided by the fully quaternized PU cationomers. The sharp yielding behavior at elongations of 4-8% requires the existence of a rigid, interconnected hard-phase. Beyond the yield point, the stress is relatively flat as a function of elongation since the continuity of the hard-phase has been destroyed. As such, increasing the level of quaternization from 50% to 100% results in an increase of the tensile modulus by 200-240%, but reduces the ultimate strength and elongation at break.

For both the R-100-I and R-50-I series of PU cationomers, the modulus increases in the order R=methyl < R=ethyl < R=propyl. Though the magnitude of the increase is near the standard deviation of the measurements, its occurrence in both series of cationomers suggests the trend is real. Based on the strength of the ionic interactions as indicated by DMTA, a trend in the opposite direction might be expected. In fact, increased tensile properties with decreasing alkyl group length was observed by H.A. Al-Salah and co-workers[36] for urethane cationomers chain-extended with N-alkyl diethanol-amine. The relationship in the present cationomers can be explained by differences in the ratio of components. In the PU cationomers the hard-segments act as physical crosslinks, and since all polymers were synthesized at a fixed stoichiometry, the volume fraction of hard-segments increases from R=methyl to R=propyl as shown for the R-100-I series in Table II-2.

The effect of neutralizing anion type on the tensile properties is shown in Table III-2 for the E-100-X polymers. Values are essentially constant with two notable

exceptions. The Young's modulus of E-100-Br is only 380 MPa versus 480 MPa for both E-100-I and E-100-Cl. However, since the standard deviations in properties for each sample are $\pm$10-15%, this difference may not be statistically significant. A second difference, which is well outside the limits of statistical error, is the lower ultimate elongation of E-100-Cl. Visible turbidity in this sample suggests that excess sodium chloride from the ion exchange procedure likely formed microscopic agglomerates, which act as defects where stress concentration and premature sample failure occur. Kohjiya and co-workers[46] observed an increase in the tensile modulus of water-swollen ionenes with increasing radius of the halogen counter-anion, but did not report tensile properties of dry polymers.

B.4. Small-angle X-Ray scattering. SAXS data for PU-BD, and PU cationomers as a function of alkyl group and ion content, are shown in Figure III-7. The scattering profile for PU-BD exhibits an upturn in intensity at small angles, followed by a single maxima near $q=0.6$ nm^{-1}. The microstructure of conventional polyurethanes has been extensively studied, and it is widely accepted that when the hard-segment content is roughly 50%, the peak results from a periodic arrangement of lamellar hard and soft domains. Li and Cooper[70] used transmission electron microscopy to show that the lamellae of a MDI/BD/PTMO urethane at 50 wt.% hard-segment are somewhat disorganized, lacking uni-dimensional periodicity over a length scale greater than a few lamellae. SAXS patterns of these materials therefore lack higher-order reflections which are frequently observed in systems with ordered lamellae.
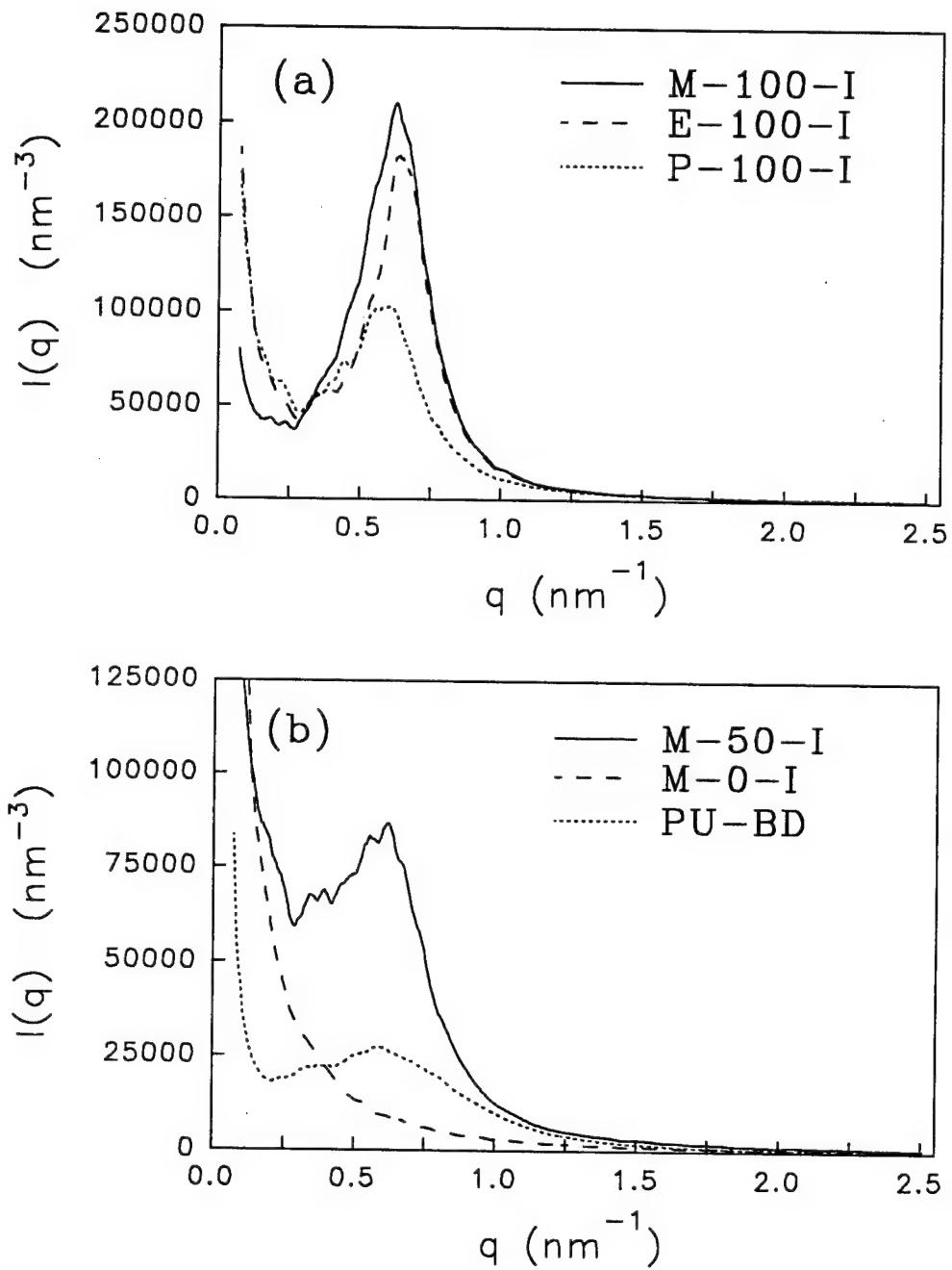
Figure III-7.   Small-angle X-ray scattering profiles of (a) R-100-I polyurethane cationomers, and (b) a conventional PU and the R=methyl series of cationomers.

The absence of an interference peak in the SAXS curve for sample M-0-I is consistent with the results of other techniques which suggest that the unquaternized polymers are mixed soft segment-hard segment one-phase materials. PU cationomers R-100-I and M-50-I have scattering profiles similar to PU-BD, though the maxima is generally less intense and broader in the latter. This result suggests that the morphology of the PU cationomers, like that of PU-BD, is lamellar. However, SAXS data from many other ionomers also show only one peak, and these scattering profiles can be modelled reasonably well by assuming a morphology of isolated ion-rich domains (or aggregates) within an organic matrix. Such a morphology is depicted in Figure I-2.

The position of the maxima in the quaternized polymers is relatively insensitive to the ionic content or alkyl group, and lies in the range of $0.60 \text{ nm}^{-1} \leq q \leq 0.63 \text{ nm}^{-1}$. A corresponding Bragg spacing of approximately 10 nm is typical of the interlamellar spacing for PUs, but not common to ionomers where the interaggregate spacing is usually 3-4 nm. Perhaps the strongest evidence that the morphology of the PU cationomers is similar to that of conventional urethanes is provided by the yield point in stress-strain curves of fully ionized copolymers. It is inconceivable that only ionic groups could form interconnected hard domains, since the pendant ammonium groups constitute less than 20 wt% of the PU cationomers. An interconnected morphology is possible only if both MDI and the chain-extender comprise the hard-domains.

Aggregation of ionic groups within the lamellar hard domains remains a possibility. By the presence of two Bragg peaks, previous X-ray scattering investigations showed that both commercial Nafion[71] and Surlyn[72] ionomers of E.I. du Pont de Nemours

and Co. contain ionic aggregates within the interlamellar layers of the semicrystalline polymer matrix. Similarly, Weiss and co-workers found that ionic aggregates formed within the polystyrene domains of a sulphonated polystyrene (SPS)-(ethylene-co-butylene)-SPS triblock copolymer.[73] However, no evidence of a second peak attributable to ionic aggregation is seen in SAXS profiles of the PU cationomers to $q=6.0$ nm^{-1}. This could imply that ammonium groups do not associate in the hard domains of PU cationomers for reasons similar to those suggested by Eisenberg and co-workers.[74,75] They found no evidence of microphase separation in random styrene-vinylpyridinium cationomers, and suggested that the large pyridinium ion and weak interactions between ion pairs precluded phase separation where the matrix T_g was above room temperature. Since the T_g of the unionized hard domains is approximately 60°C, this argument could be applied to the PU cationomers. However, it is also possible that ionic groups do associate within the hard domains, but the quantity and order of the aggregates are not sufficient to produce a maxima in SAXS profiles.

Additional morphological information can be obtained from the Porod behavior shown in Figure III-8. In the conventional urethane PU-BD, the slope of the product $q^4I(q)$ is negative at high values of q, indicating the presence of diffuse phase boundaries. This behavior has been frequently observed and studied in PUs with semicrystalline hard-segments.[15,76] On the other hand, the slope of the plot for PU cationomers R-100-I and M-50-I is positive, indicative of mixing between phases. This result is surprising in light of the DMTA and DSC results which show the R-100-I materials are much more phase-separated than PU-BD. One could rationalize this discrepancy by stating that the
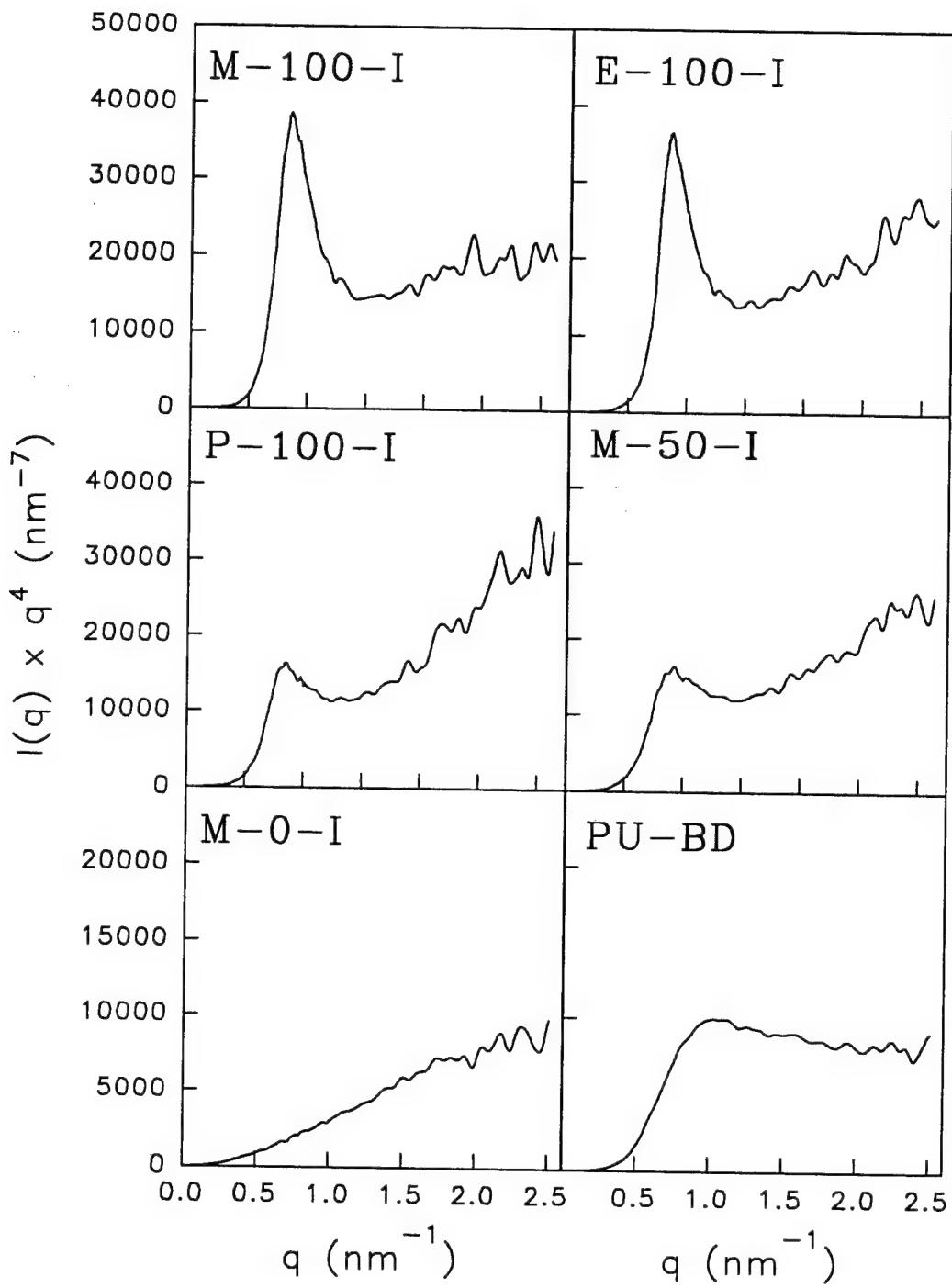
Figure III-8. Porod plots of SAXS data from Figure III-7.

PU cationomers have virtually no interfacial region. A more likely explanation is that isolated or associated iodine atoms within the hard-phase produce spikes in the electron density profile of the domain. Based on an ionic radius of 2.2Å, isolated iodine atoms would have an electron density of 1210 e^-/nm^3, whereas the average electron density of the fully phase-separated hard-segments are only 430-450 e^-/nm^3 (Table II-2).

For a lamellar system, an estimate of the interdomain spacing can be obtained from Bragg's law by weighting the scattered intensity by q^2. The results for PU-BD, and the R-100-I and M-###-I series of cationomers are plotted in Figure III-9. As in Figure III-7, the position of the maxima is nearly constant for all quaternized materials, while no peak is present for the unquaternized polymer M-0-I. An alternative method of estimating the interlamellar distance is to use the one-dimensional correlation function (CF), $\gamma(x)$, given by Equation II-3. Spacings are determined from the position of the first maxima in $\gamma(x)$ as shown in Figure III-10. As seen in Table III-3, results of the two methods are in reasonable agreement, with spacings determined from the CF slightly lower. Bragg spacings vary from 9.5-10.0 nm, while distances determined from the CF analysis range from 8.9-9.4 nm. Interlamellar distances of the two-phase PU cationomers do not appear to be a function of alkyl group or ionic content. The latter result is consistent with a morphological investigation of PU cationomers by Lipatov et al.;[33] and provides further evidence that the SAXS peak does not result from arrangements of ionic groups, since the inverse of the distance between ionic aggregates would be expected to scale with the ion concentration.[77]
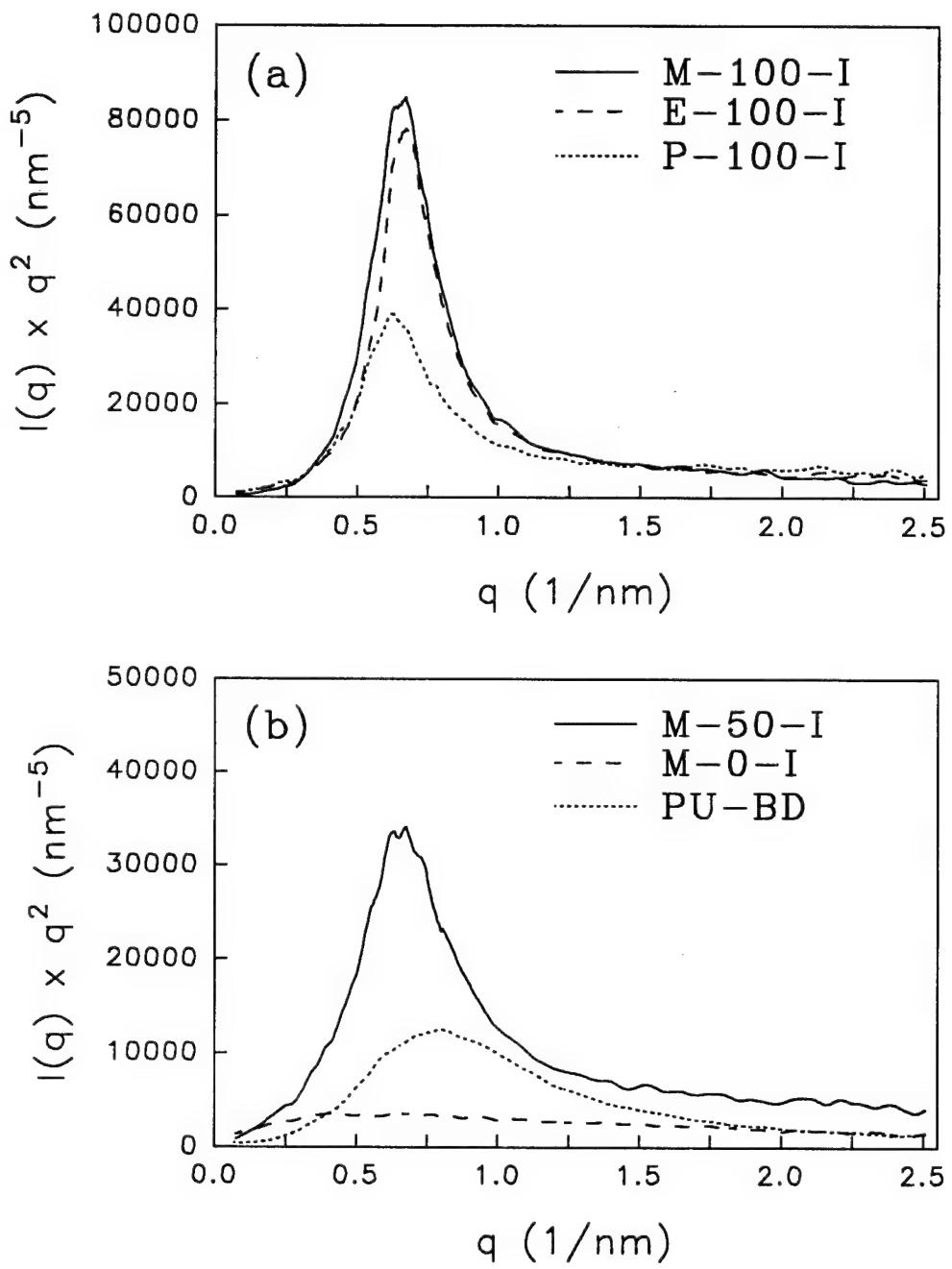
Figure III-9. Plots of $q^2I(q)$ vs q for determination of the interlamellar Bragg spacing. (a) and (b) same as Figure III-7.
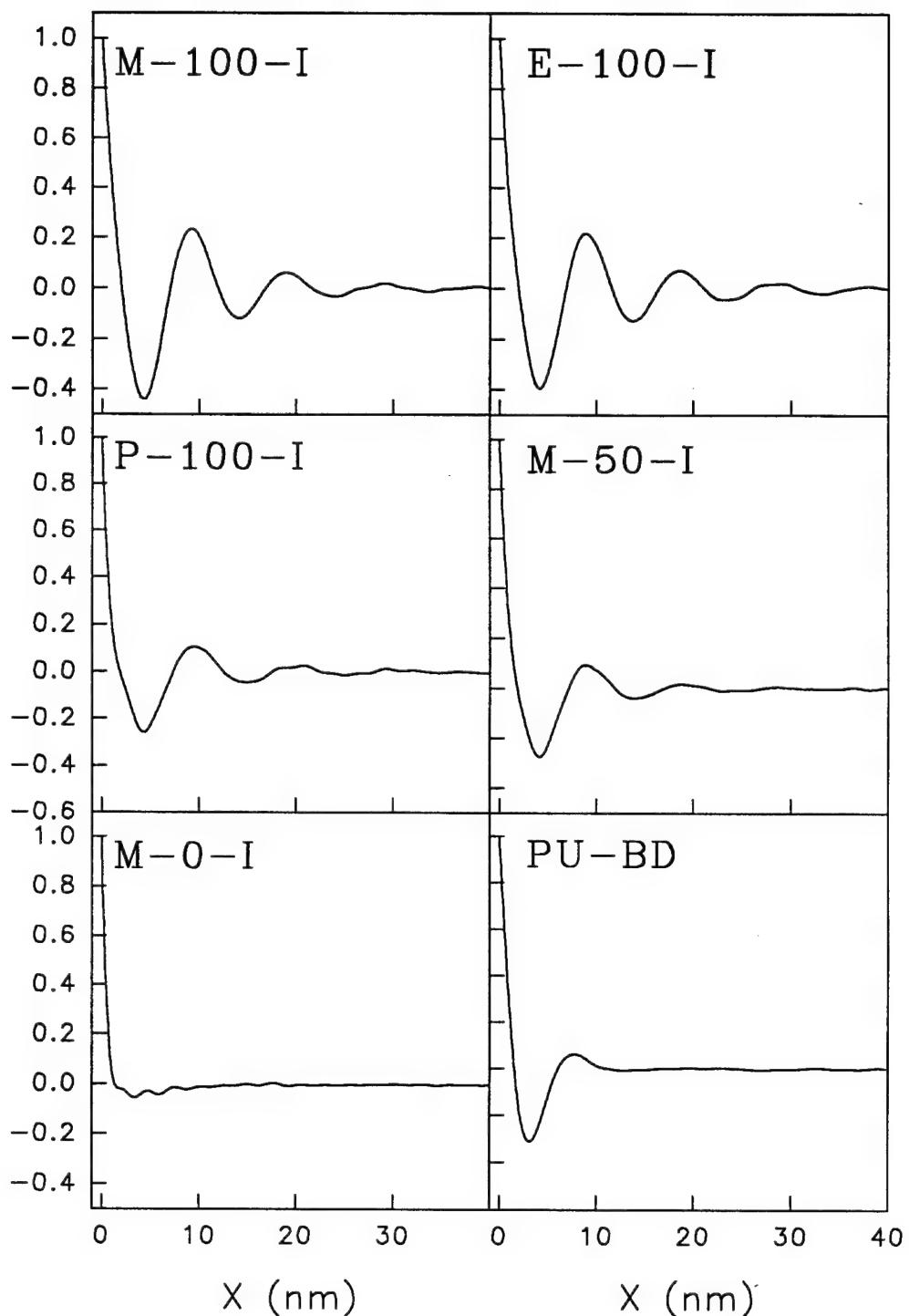
Figure III-10. One-dimensional correlation functions of PU-BD, and the R-100-I and R=methyl series of polyurethane cationomers.

Table III-3
Interdomain Spacings (nm) for PU Cationomers

Sample	Correlation Distance 1-D $\gamma(x)$	Bragg Spacing $q^2I(q)$
M-100-I	9.2	9.7
M-50-I	8.9	9.7
E-100-I	8.9	9.5
P-100-I	9.4	10.0
PU-BD	7.8	8.0

A semi-quantitative measure of the degree of phase separation in two-phase materials can be obtained from SAXS by the ratio $\overline{\Delta\rho^2}/\overline{\Delta\rho^2}_{id}$. Results for the PU cationomers and PU-BD are summarized in the last column of Table III-4, with calculation of the ratio as follows. First, the mean-square variance of the electron density, $\overline{\Delta\rho^2}$, is calculated from the experimental invariant, Q/V, using Equation II-4. The mean-square electron density fluctuation for a completely phase-separated copolymer, $\overline{\Delta\rho^2}_{id}$, is then calculated from Equation II-5 and data of Table II-2.

Ratios of 0.67-0.78 for the R-100-I cationomers indicate a higher degree of phase separation than in M-50-I or PU-BD. This result is consistent with DMTA and DSC results, but the relationship between alkyl group and phase mixing (P-100-I $\approx$ M-100-I > E-100-I) does not agree with earlier results. However, determining the degree of phase separation with this approach is limited by errors in background subtraction, extrapolation of experimental data to high scattering vectors according to Equation II-7, and the assumptions used in calculating $\overline{\Delta\rho^2}_{id}$.

C. Summary

The morphology and properties of polyurethane cationomers with pendant trialkylammonium groups were investigated as a function of ion content, alkyl group length, and neutralizing anion. Results of DSC, DMTA and tensile testing showed that ionic content had the greatest effect on phase separation and mechanical properties. Bulky pendant groups of DAP and TAPI, attached to asymmetric carbon atoms, prevented crystallization in the hard domains. Consequently, little or no phase separation was

Table III-4

Phase Separation as Estimated from SAXS Invariant

Sample	Q/V (nm^{-6})	$\overline{\Delta\rho^2}$ (nm^{-6})	$\overline{\Delta\rho^2_{id}}$ (nm^{-6})	$\overline{\Delta\rho^2}/\overline{\Delta\rho^2_{id}}$
M-100-I	45000	2280	3460	0.66
M-50-I	32000	1620	3370	0.48
E-100-I	43000	2180	2810	0.78
P-100-I	35000	1770	2650	0.67
PU-BD	14000	710	1620	0.44

evident in the unionized materials. As the level of quaternization was increased, phase separation greatly improved as evidenced by an extension of the rubbery plateau, a lowering of the soft-segment T_g, and an increase in the tensile modulus.

The effect of the alkyl group length was secondary to the ion content, with the strength of the ionic interactions following the relationship R=methyl > R=ethyl > R=propyl. Stronger interactions generally resulted in improved phase separation, and an extension of the rubbery plateau to higher temperatures. Within the range studied, the type of neutralizing anion had little effect on phase separation or mechanical properties.

SAXS and tensile results suggest that while ionic interactions are the primary driving force for phase separation, they produce a microstructure not typical of ionomers, but rather more closely related to the lamellar morphology of a conventional urethane of MDI/BD/PTMO. Different levels of phase mixing were also evident in SAXS profiles, but the interlamellar spacing of the two-phase PU cationomers was not affected by the ion content or alkyl group.

Chapter IV. Investigation of the Room Temperature Annealing Peak

A. Introduction

When performing the general characterization experiments of Chapter III, an interesting phenomenon was inadvertently discovered. If the PU cationomers were stored at room temperature for a period of approximately 1 month in a desiccator filled with dry calcium sulfate, DSC scans showed a small endotherm centered near 70°C. This endotherm was not present in unannealed cationomers or the unionized R-0-I polymers, and did not reappear during subsequent cooling and heating cycles in the DSC. Similar "room temperature annealing peaks" were reported in other ion-containing polymers, most notably the well-known commercial ionomer Surlyn®, nearly 20 years ago.[78]

The tradename Surlyn® covers several copolymers of ethylene and methacrylic acid (E-MAA) with various ion contents and neutralizing metal ions. E-MAA was one of the first ionomers to be studied, and small-angle X-ray scattering investigations of E-MAA provided the first direct evidence of microphase separation in ionomers.[79] Marx and Cooper reported that a room temperature annealing endotherm in E-MAA was centered at approximately 50°C, and had a breadth of approximately 20°C.[78] The authors attributed the endotherm to the melting of crystallites formed from short imperfect polyethylene chains. Annealing at various temperatures above 40°C caused a second endothermic peak centered 20-50°C above the annealing temperature. This feature was assigned to lamellar thickening, and its temperature dependence annealing temperature was shown to be qualitatively similar to the lamellar thickening endotherm normally found in intermediate and high density polyethylene.[80]

The assignment of the first peak to polyethylene crystallite melting was challenged by Tadano et al.[81,82] In plots of specific volume versus temperature, a peak was found at the temperature corresponding to the DSC endotherm, whereas crystalline melting would normally cause a discontinuity. Also, the change in the wide-angle X-ray scattering (WAXS) pattern after room temperature annealing was very small, and considered not large enough to correspond to the DSC endotherm. Other factors, such as an insensitivity of the peak position to annealing temperature, supported the conclusion that the assignment of polyethylene crystallite melting was incorrect.

Tadano and co-workers attributed the room temperature annealing peak to an order-disorder transition within the ionic aggregates, i.e. melting of ionic crystallites. Since WAXS is unlikely to show crystalline order within the aggregates even if it exists (ionic domains comprise only a small volume fraction of the ionomer, and the aggregates are so small that insufficient translational symmetry exists to cause Bragg reflections), obtaining direct evidence of an ionic order-disorder transition has been difficult. EXAFS studies were performed in order to determine the local order in zinc-neutralized E-MAA as a function of temperature.[83] The Zn-O first-shell coordination distance R was slightly smaller at 105°C than at room temperature. At the higher temperature, the authors' analysis also determined that the first-shell coordination number N and the Debye-Waller factor σ increased. However, the rise in coordination number is inconsistent with the decrease in R, since studies of coordination shells in inorganic Zn-O compounds have shown that R increases from about 1.95-1.98 Å to 2.00-2.02 Å to 2.06-2.10 Å as the coordination of zinc changes from fourfold to fivefold to sixfold.[84] Neutralization with

a combination of zinc and 1,3-bis(aminomethyl) cyclohexane (BAC) caused a slight distortion in the local environment of zinc atoms as evidenced by an increase in breadth of the first-shell peak, which was attributed to an increase in the Debye-Waller factor. At 105°C a shoulder at low R was apparent, which the authors attributed to Zn-N coordination in the first shell. The peak due to Zn-O coordination remained in the same position, but the intensity of the peak decreased with increasing temperature. According to the analysis, the decrease in intensity was caused by an increase in the Debye-Waller factor, while the coordination number remained constant.

These authors have used a number of other analytical techniques to investigate the effect of room temperature annealing on E-MAA ionomers, including: tensile testing,[82] far-infrared spectrometry,[85] DC conductivity,[86] dielectric relaxation,[87] and dynamic mechanical analysis.[88] Perhaps the strongest evidence for ionic crystallite ordering was the gradual increase in tensile modulus that occurred upon room temperature annealing. The modulus increased nearly an order of magnitude, and the increase correlated with the area of the DSC annealing peak. Far-infrared spectra showed a decrease in the frequency of the Zn-O vibration near 250 cm^{-1} above the transition temperature. DC conductivity experiments showed an anomaly near 50°C after room temperature annealing. Dielectric relaxation spectra do not seem to be sensitive to the transition, since no clear change occurred in either ϵ' or ϵ'' at temperatures around the annealing endotherm. However, spectral features associated with the melting of polyethylene crystallites were very broad and could have obscured the transition. Only phase-separated materials exhibited a

DMTA transition on annealing at room temperature, while the DSC thermograms of both two-phase and one-phase ionomers showed an endotherm.

Room temperature annealing of E-MAA has also been investigated as a function of the neutralizing cation.[89] An endothermic peak, centered between 40 and 60°C, appeared upon storage for all cations studied (H^+, Na^+, K^+, Mg^{2+}, Zn^{2+}, Cu^{2+}, Mn^{2+} and Co^{2+}). If BAC was added to the polymer, the type of neutralizing cation affected the behavior of the tensile modulus. In all cases the modulus initially increased with added BAC, but materials neutralized with Mn^{2+} showed a decrease in modulus above 0.5 mol of BAC per mol of carboxylate, while the modulus in materials neutralized with Zn^{2+}, Cu^{2+} and Co^{2+} either continued to increase or remained approximately constant.[90]

The addition of BAC to zinc-neutralized E-MAA caused the DSC room temperature annealing peak to increase in area and shifted the position to slightly higher temperature.[81] When equimolar amounts of methacrylic acid and BAC were mixed in hexane, followed by evaporation and subsequent storage for 7 days at room temperature, an endothermic peak developed at 60°C. The as-cast mixture exhibited no peak, similar to the behavior of the ionomer.

Thirteen different amines were added to E-MAA neutralized with 0.2 mol of zinc per mol of carboxylate (the remaining groups remained in the acid form) to test the effect of amine type.[91] Compounds with two or more amine groups were more effective in increasing the modulus, which suggests such compounds acted as cross-linking agents. Primary and secondary amines increased stiffness more than tertiary amines, and more

rigid and higher boiling amines resulted in ionomers with a higher modulus than their lower boiling counterparts. However, polymeric amines decreased the modulus. With some amines, the tensile modulus correlated with the area of the annealing peak.

The discussions to this point have considered two hypotheses for the room temperature annealing peak in ionomers: polyethylene crystallite melting, and an order-disorder transition of the ionic aggregates. Another conceivable explanation for the phenomenon is absorption of water from the atmosphere. A series of papers by Painter and Coleman[92-95] found that the absorption of small amounts of water in E-MAA, which occurred even when the samples were stored over anhydrous calcium sulfate, dramatically affected the infrared absorption spectra. Upon initial cooling from the melt, relatively sharp bands were found in the region from 1500 to 1600 cm^{-1} for E-MAA ionomers fully neutralized with a metal cation. After annealing for many days or weeks at room temperature, these sharp peaks were replaced by a broad featureless band centered near 1550 cm^{-1} (the exact position depended on the metal cation). The investigators conclusively showed that this dramatic change in the infrared spectra was due to water absorption. E-MAA ionomers neutralized with zinc did not show this effect; however, the 1500 to 1600 cm^{-1} region of the spectra in the original, unannealed sample was already broad and featureless. Only one set of DSC curves (for a Ca^{2+} neutralized ionomer) was presented, and a similar room temperature annealing peak was evident after storage for 84 days.[93] Infrared results for this sample later showed the presence of absorbed water.

The effect of large amounts of water absorption on the room temperature annealing peak in E-MAA ionomers has also been studied,[96] with the quantity of absorbed water determined from the weight loss after drying under vacuum at 450 K. In this study, the authors discovered that a small amount of residual water was very strongly bound to the cation. The position of the room temperature annealing peak shifted from 341 K to approximately 330 K as the water content increased from 0.16 mol H_2O/mol MAA to 0.5 mol H_2O/mol MAA. Over this same range, the area of the endothermic peak also decreased rapidly with increased water. As the amount of absorbed water increased further, both the location and the area of the peak remained constant. In this recent paper, Tadano and co-workers also presented a revised model for the ionic order-disorder transition. By analogy with sodium hexanoate, they proposed that the endothermic peak formed on annealing at room temperature was due to a combination of ionic crystallite melting and melting of short methylene segments attached to the ionic groups.

As discussed in Chapter III, results from DMTA and DSC showed that the asymmetric carbon of TAPI and DAP prevents hard segment crystallization. Further, the molecular weight of the PTMO used in the present studies is insufficiently low for the soft segments to crystallize within the multiblock copolymer. Consequently, the room temperature annealing endotherm in these PU cationomers can not be attributed to melting of organic-polymer crystallites. In this chapter, DSC and EXAFS temperature studies were used to determine if either formation of ionic crystallites or water absorption was the source of this endotherm.

70

B. Results and Discussion

The room temperature annealing peak is demonstrated for the PU cationomers by the DSC scans of Figure IV-1. Many of the same characteristics described for the E-MAA ionomers are displayed. In the unquaternized material, only the mixed hard segment-soft segment glass transition discussed in Chapter III was observed. The unannealed, fully quaternized samples displayed only a soft-phase glass transition near -50°C. To reiterate, the absence of a hard-phase glass transition in these materials was not surprising since the DSC scans of amorphous PUs often show no evidence of a transition. After annealing for 54 days at room temperature in a desiccator containing dry calcium sulfate, the initial DSC scans of the PU cationomers clearly showed a new endothermic peak centered at approximately 60°C for M-100-Br and near 80°C for M-100-I. The second DSC scans, which were collected following a rapid quench from 150°C, showed no evidence of the endothermic peak.

B.1. Qualitative effect of temperature on EXAFS spectra. To further investigate the origin of this peak, EXAFS experiments were performed over the temperature range of the DSC endotherm to examine the change in local environment around the anion. The M-100-Br samples used in the EXAFS experiments were also stored in a desiccator over dry calcium sulfate. A short example of the analysis procedure for EXAFS data is illustrated as follows for the bromine cationomer at 25°C. The raw μt vs E data shown in the upper portion of Figure IV-2 was converted to $\chi(k)$ vs k, and weighted by k^2 as shown at the bottom of Figure IV-2. Determination of $\mu_0(E)$ and normalization was done by fitting the $\mu(E)$ curve to a cubic spline with three sections.

71
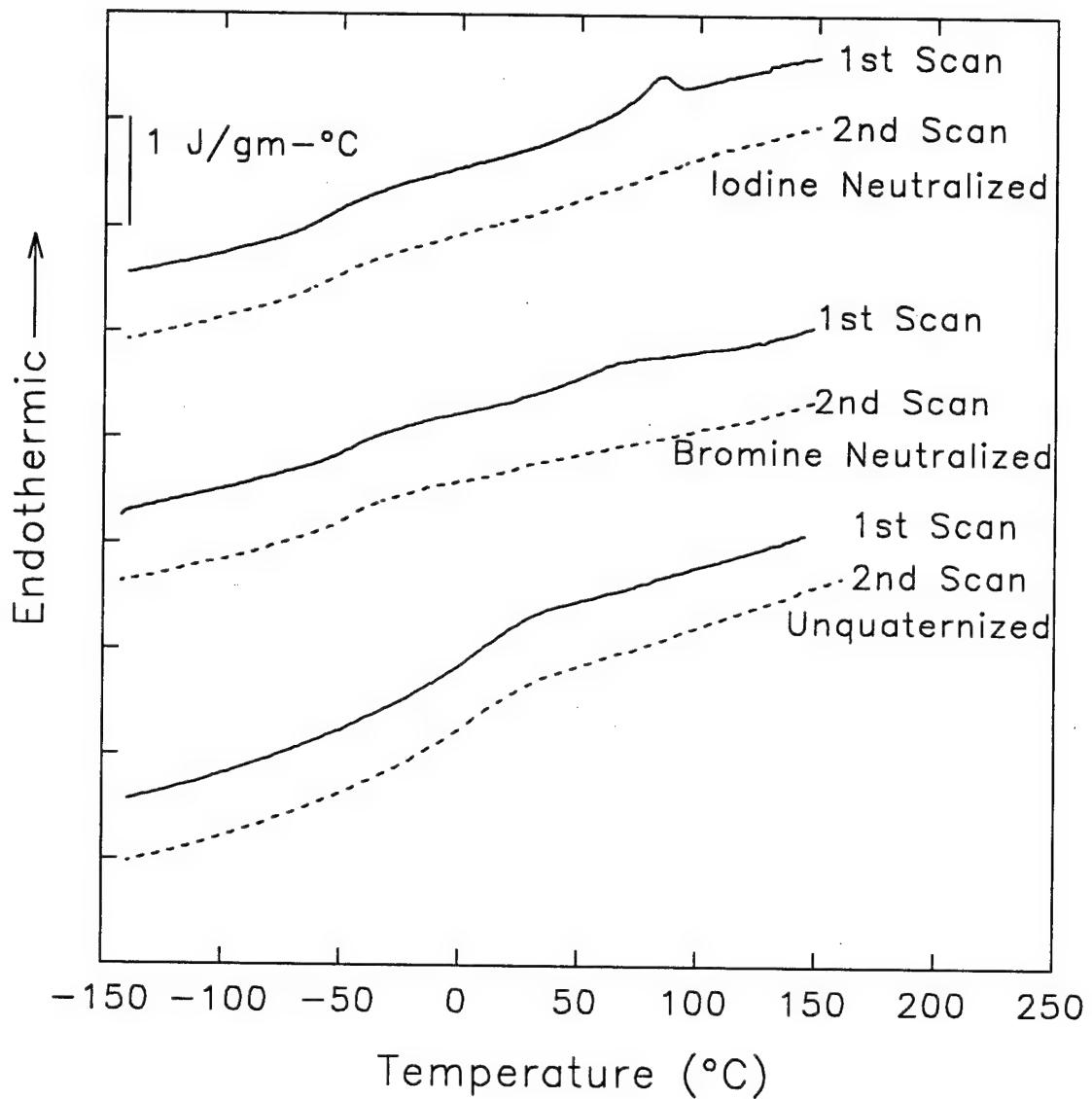
Figure IV-1. DSC results. Polymers were solution cast from DMAc, thoroughly dried in a vacuum oven, and stored in a desiccator containing dry calcium sulfate for 54 days.
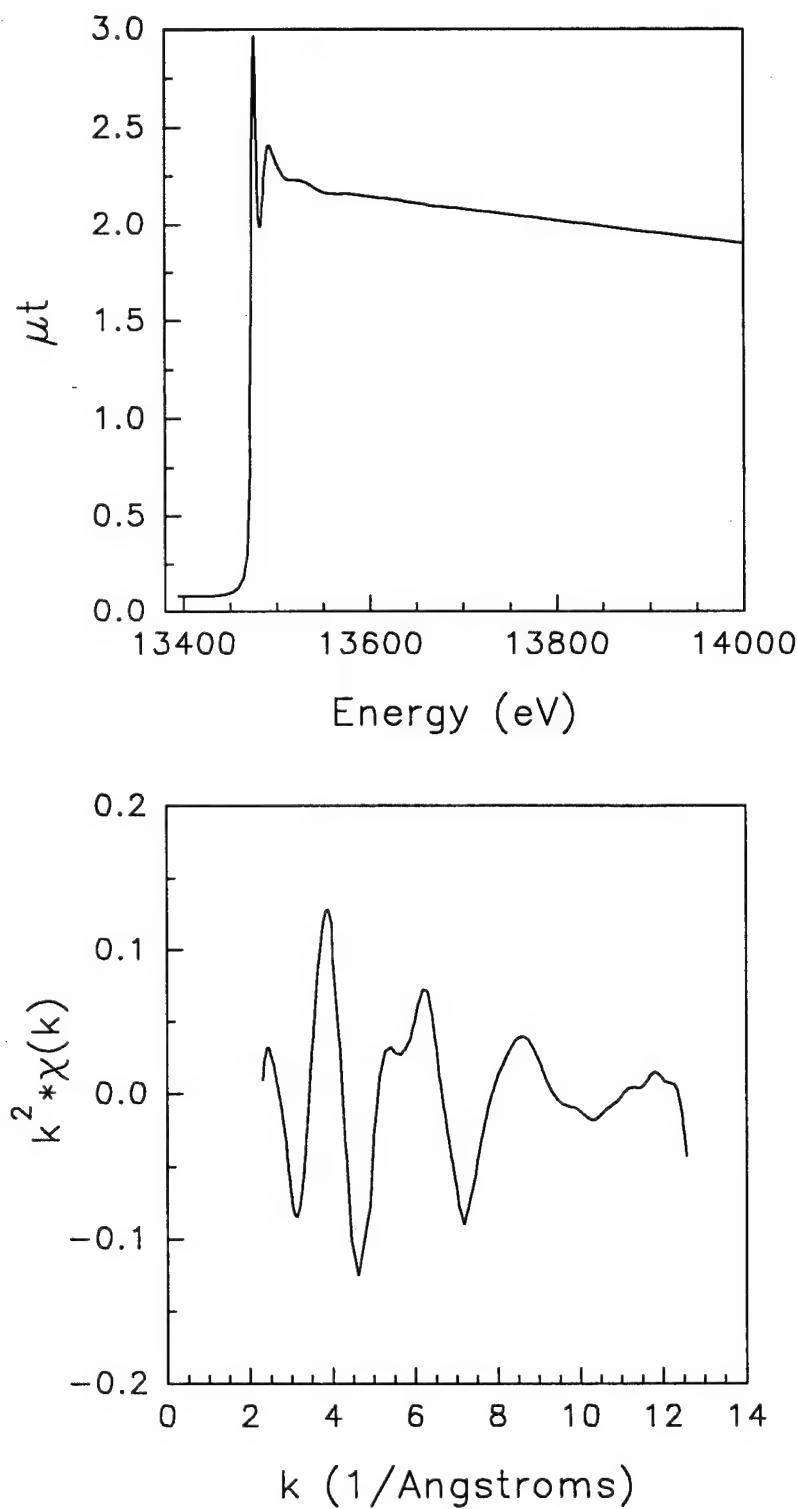
Figure IV-2. (Top) raw μt vs E data, and (bottom) conversion to $k^2\chi(k)$ vs k for M-100-Br at 25°C.

Because of the simple features in the XANES region, the data was truncated only 20 eV above the edge, which corresponds to $k \approx 2.3$ Å^{-1}. Upper energy truncation at $k = 12.5$ Å^{-1} was necessary because of noise above this value in some data sets. Fourier transformation of the $k^2\chi(k)$ vs k curve resulted in the radial structure function (RSF) shown in Figure IV-3. The units of the abscissa of the RSF are angstroms, but the peaks are shifted from the true interatomic distances as indicated in Equation II-8, hence a subscript F is used to differentiate this distance from the actual interatomic distance R. Individual peaks were isolated using a Hanning function and back-transformed for further data analysis. At all temperatures, the regions of isolation for the bromine cationomer were 0.62-1.8 Å for the first-shell peak and 2.1-2.9 Å for the second-shell peak. An identical analysis procedure was used for the model compounds.

Because a visual inspection of the RSF can give qualitative information about the coordination shells around an atom, Figures IV-4 and IV-5 show the changes in the RSF as the temperature was raised to 105°C. As indicated in Figure IV-1, this temperature region encompasses the DSC endothermic annealing peak. The RSF consists of 2 peaks, which means that there were at least two different coordination shells around the bromine anion. The peak at lower R_F was essentially unaffected by the change in temperature, while the second-shell peak decreased in height and the position shifted slightly towards lower R_F as the temperature increased. The small changes in the RSF indicate that the increase in temperature caused only minor changes in the local environment. Within the range investigated, temperature apparently had no effect on the first coordination shell. The shift to lower R_F in the second peak suggests that the distance between the bromine
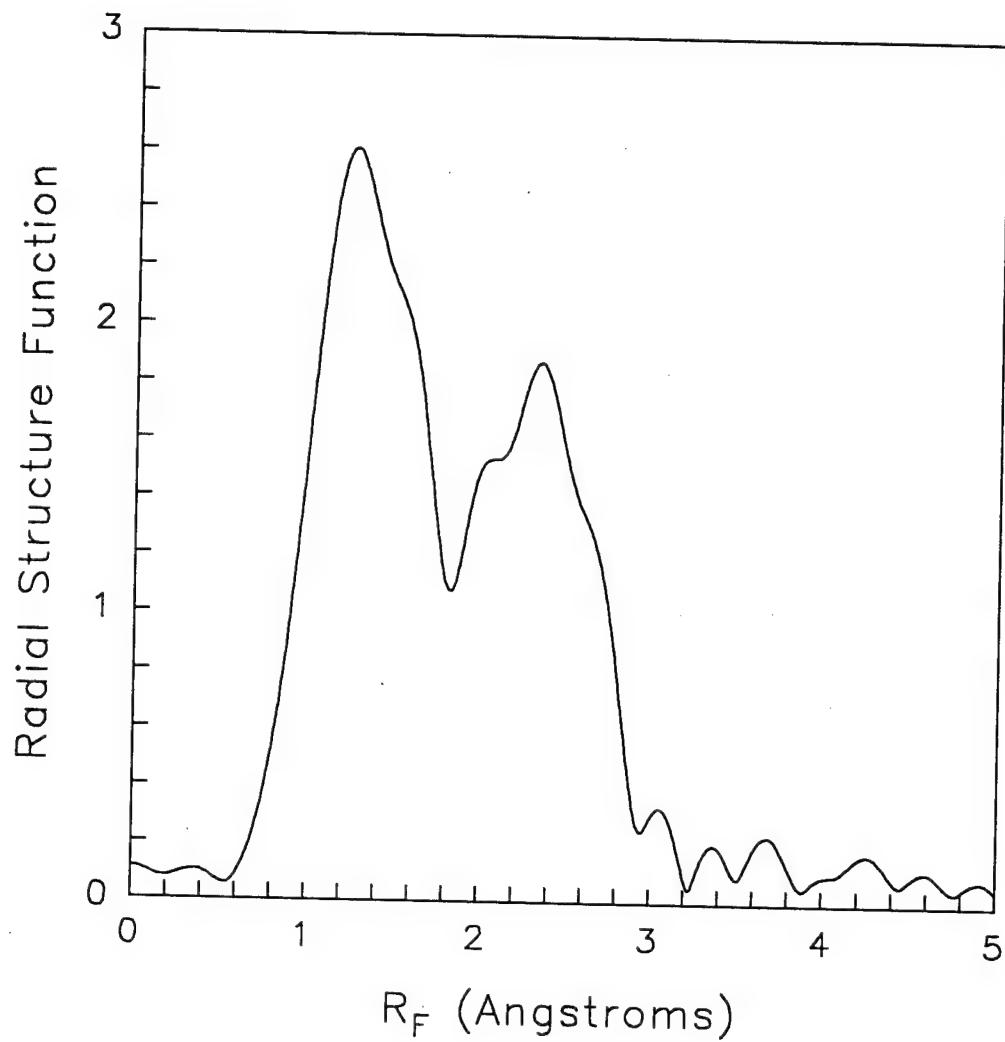
Figure IV-3. RSF for M-100-Br at 25°C. This plot is the Fourier transform of the bottom plot in Figure IV-2.
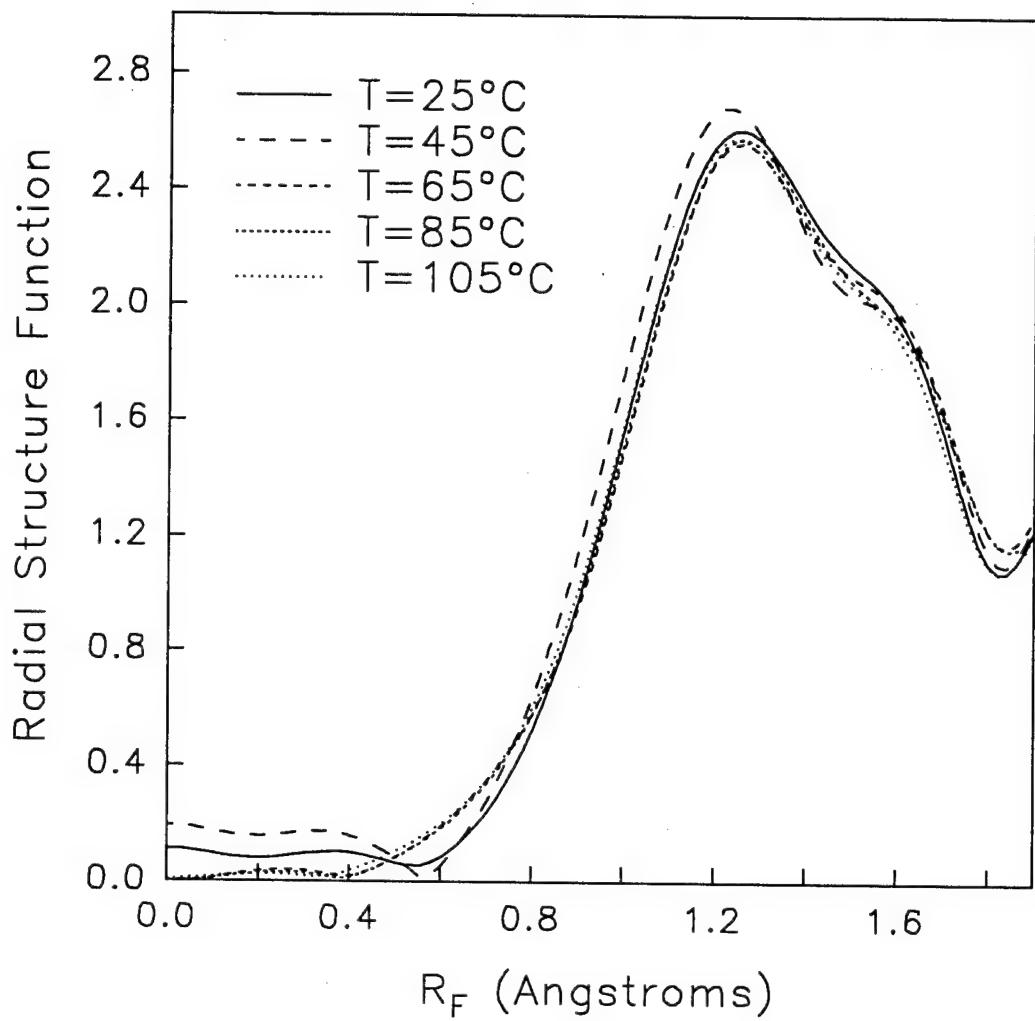
Figure IV-4. RSF of M-100-Br at various temperatures, where both scales have been expanded to highlight the first coordination shell.
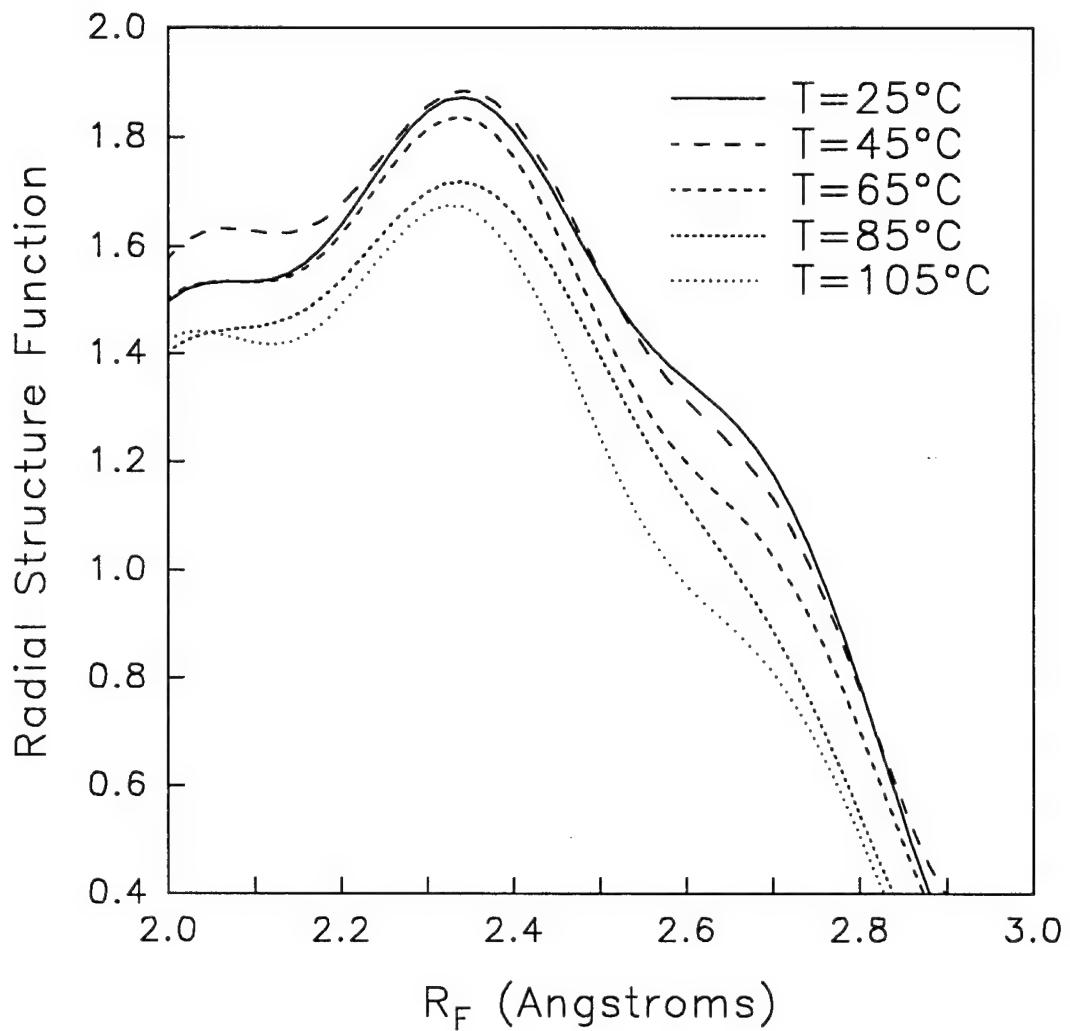
Figure IV-5. Same as Figure IV-4, except both scales are now expanded to highlight the second coordination shell.

atom and the second coordination shell may have decreased, but further analysis indicated that the change in R was not outside of experimental error. The decrease in height of the second peak establishes that either the number of atoms in this coordination shell decreased, or the Debye-Waller factor increased.

B.2. Effect of temperature on coordination shell parameters. As will be discussed in detail later, both coordination shells were probably comprised of more than one type of atom and/or the shell consisted of one atom at a large distribution of distances. In either case, the ratio method cannot generally be applied to coordination shells with such characteristics. However, application of the ratio method in the present study seemed to give legitimate results, since analysis suggested that nothing changed within experimental error except the number of atoms in the second shell. Figure IV-6 shows the results of the analysis for the first shell using the ratio method; no statistically significant changes were observed in either the Debye-Waller factor or the coordination number as the temperature increased. Error bars were calculated assuming no changes in the first-shell parameters, and represent two standard deviations. The percentage errors agree well with a much more careful calculation of the error in nickel and zinc-neutralized sulfonated polystyrene ionomers.[97] As the temperature increased, one would have expected an increase in the Debye-Waller factor. However, as was shown for lead[98] and confirmed in this study, the increase of σ^2 over a temperature range of less than 100°C is not greater than the experimental error. R also did not change significantly with temperature.

78
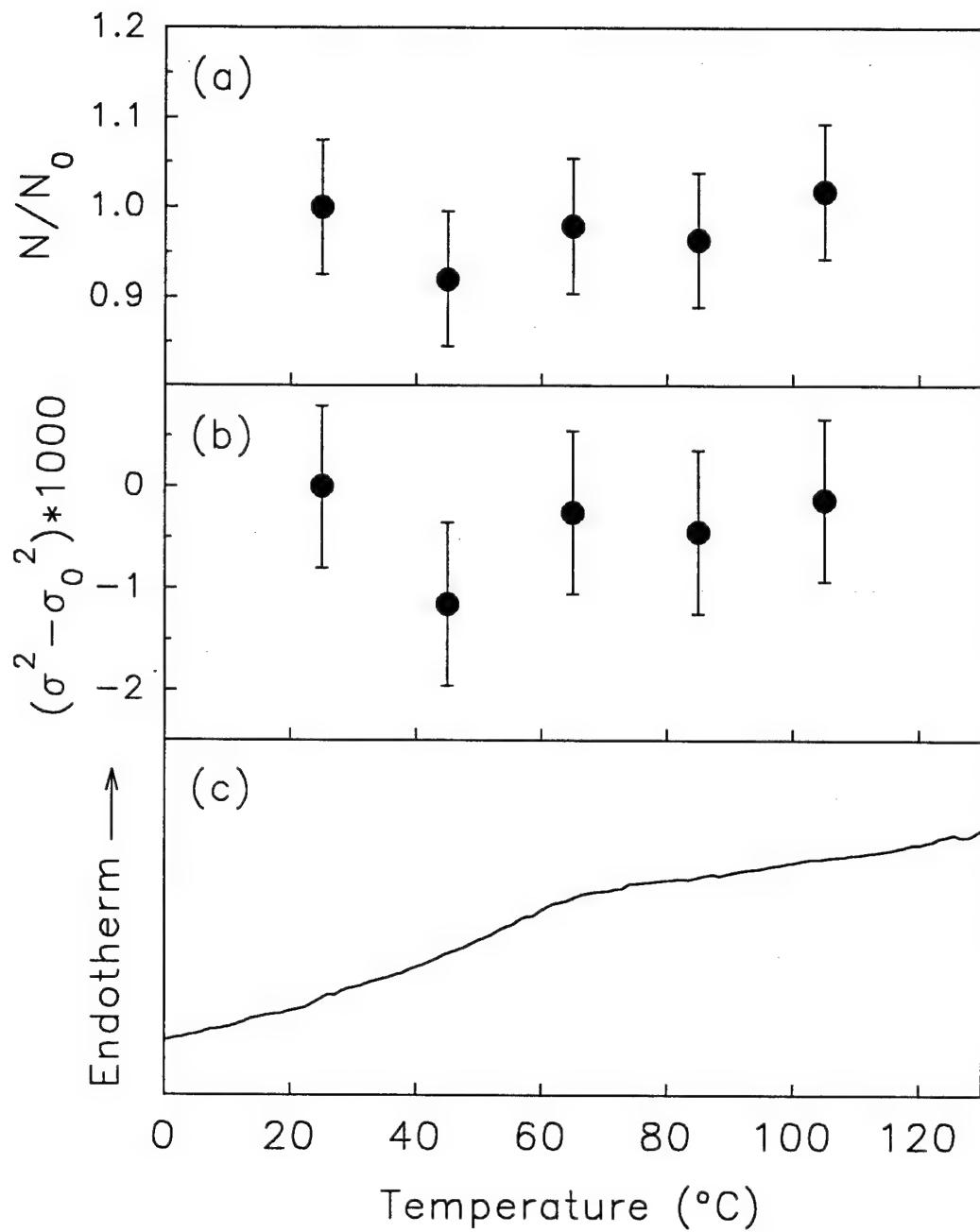
Figure IV-6. Results of the ratio method for the first shell using the data at 25°C as the reference: a) ratio of effective coordination numbers; b) difference in the square of the Debye-Waller factors; c) DSC thermogram of a sample prepared and stored under identical conditions, with the scan taken within 1 day of EXAFS data collection. Notice the temperature range of the EXAFS data encompasses the endothermic peak.

For the second shell, Figure IV-7 indicates that the coordination number decreased over the temperature range of the DSC endotherm. If the second shell consisted of more than one type of atom, but only one type of atom left, the fraction of departing atoms would be even greater than the vertical scale indicates. By varying the analysis procedure slightly (for example truncating at $k = 10$ Å^{-1}), the vertical scale was altered in magnitude; however, the effective coordination number always decreased with increasing temperature. The behavior of the Debye-Waller factor was dependent on the analysis conventions; it was either constant or decreased with temperature. Since a decrease in the Debye-Waller factor increases the RSF peak height, the decrease in the second-shell peak height was solely a result of a change in coordination number. Finally, the same general trends were observed in data from a second sample with a lower signal-to-noise ratio; the first shell was unaffected by temperature, while the second shell showed a decrease in peak height at increased temperatures which the ratio method attributed to a decrease in N/N_{ref}.

In E-MAA, the first and only coordination shell in EXAFS studies[83] was oxygen, which did not allow unambiguous assignment of the change in coordination environment to either water evaporation or crystallite melting. However, the data in that paper seems to support the former more than the latter. For materials with BAC, one would expect a decrease in RSF peak height if water were leaving the coordination shell in E-MAA and nitrogen were entering the coordination environment of zinc, which agrees with experimental observation. The introduction of nitrogen into the local environment of water-free zinc as a result of an ionic crystallite melting process is much more difficult to rationalize, since charge neutrality must be maintained and the constancy of the radius

80
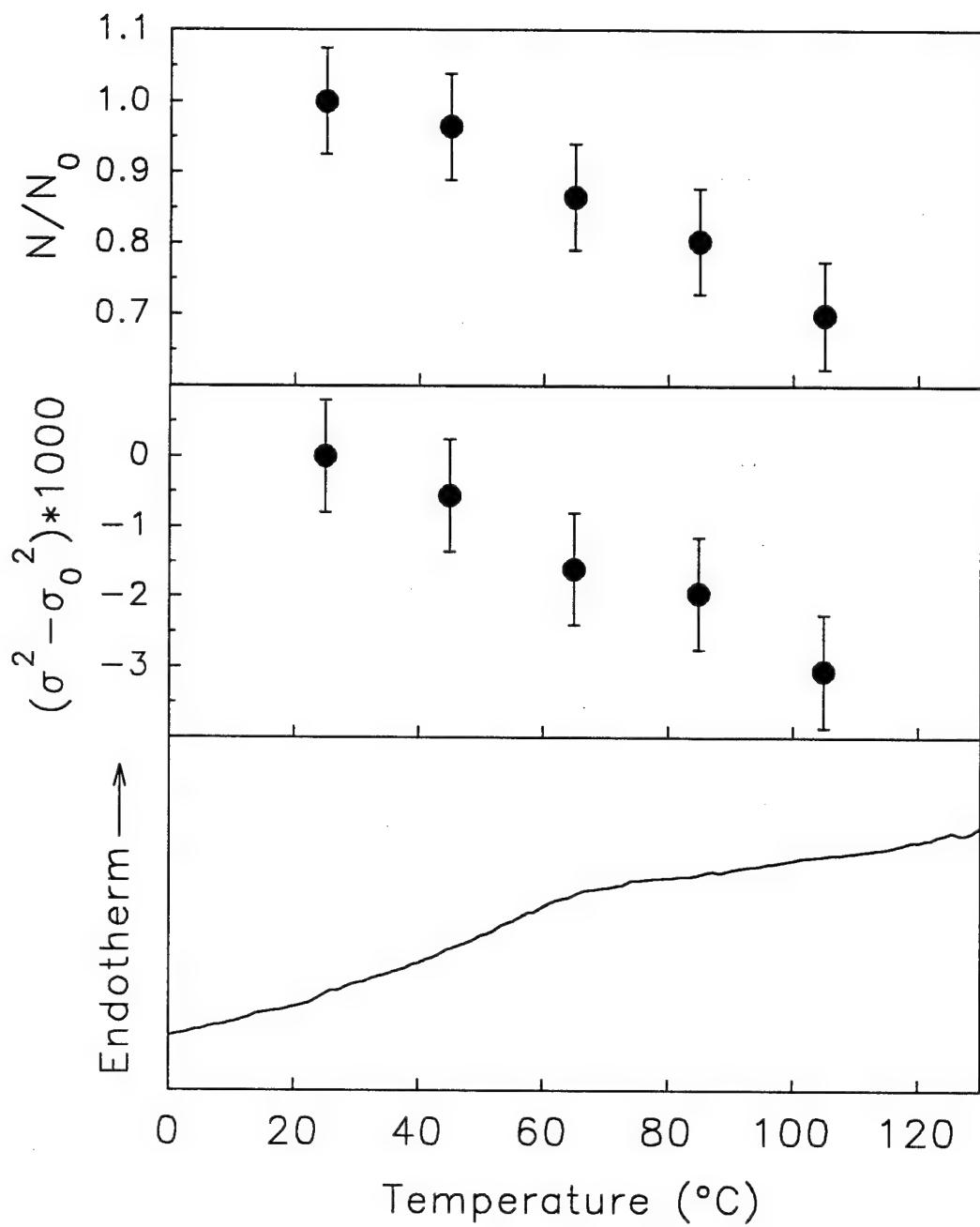
Figure IV-7. Same three plots as in Figure IV-6, except for the second shell.

81

suggests that the coordination number was unchanged. For materials without BAC, the observed relative insensitivity of the RSF to temperature would be expected with either water evaporation or aggregate melting, and therefore cannot be used to distinguish between the two possibilities.

An EXAFS study of lead as the temperature was raised through the melting transition[98] suggests that the changes in EXAFS spectra seen in the present investigation and the previous E-MAA study are not consistent with ionic crystalline melting. The only consequence of melting in the EXAFS signal of lead was a discontinuous decrease in the coordination number, which the authors argued was caused by a 5 order of magnitude increase in the diffusion coefficient. Atoms rapidly moving from one site to another will not contribute to the Fourier transformed EXAFS signal, since the data do not extend to zero wavenumber. In the ionomers, one would expect little or no change in the diffusion coefficients of the atoms located in the first or second shells upon hypothetical ionic crystallite melting. One would therefore not expect any change in the first or second shells of the RSF if the endotherm was related to an ionic order-disorder transition, which certainly contradicts the experimental observations in both EXAFS studies.

B.3. Simulated spectra of model bromine-containing compounds. Additional quantitative analysis of the EXAFS patterns was completed using the simulation package FEFF5®. A comparison of EXAFS patterns at the bromine K-edge of CBr_4 and $NaBrO_3$ to simulations showed that both the positions and number of atoms in at least the first shell can be predicted accurately, with only the Debye-Waller factor and the amplitude reduction factor as fitting parameters. E_o for the experimental data was determined by

using the ratio method with the simulated spectrum as the reference data. The fitting results using the known crystal structures for CBr_4 and $NaBrO_3$ are given in Table IV-1, while a graphical comparison of the RSFs are given in Figures IV-8 and IV-9. For CBr_4, the agreement is excellent for all three peaks even though the crystal structure of this compound is quite complicated.[99] However, the calculated value of the Debye-Waller factor for the first shell is physically unrealistic. A slightly worse fit can be obtained by increasing the Debye-Waller factor for the first shell, decreasing S_0^2, and increasing the Debye-Waller factor for the second shell. In $NaBrO_3$, the agreement of the experimental RSF with the simulated pattern using the known crystal structure[100] was not as good, but once again the agreement for the first shell is excellent.

Based on the discussion of EXAFS theory in Chapter II, the amplitude reduction factor should only depend on the central atom. As expected, the factor was constant within experimental error for the two standards. It should be emphasized that in spite of some differences, fits of experimental and simulated RSFs for the two model compounds were generally excellent. For example, using only four adjustable parameters (E_o, σ^2 for the first and second shells, and S_0^2) the fit in Figure IV-8 for CBr_4 was obtained. Also, the values for S_0^2 were reasonable since S_0^2 should be between 0.7 and 1.0.[101] Further simulations in our laboratory of other model compounds, where bromine is not the absorbing atom, have shown that FEFF5® is generally quite accurate in quantitative prediction of the first two shells using reasonable fitting parameters;[97,102] in fact the disagreement in the higher shells of $NaBrO_3$ was somewhat surprising.
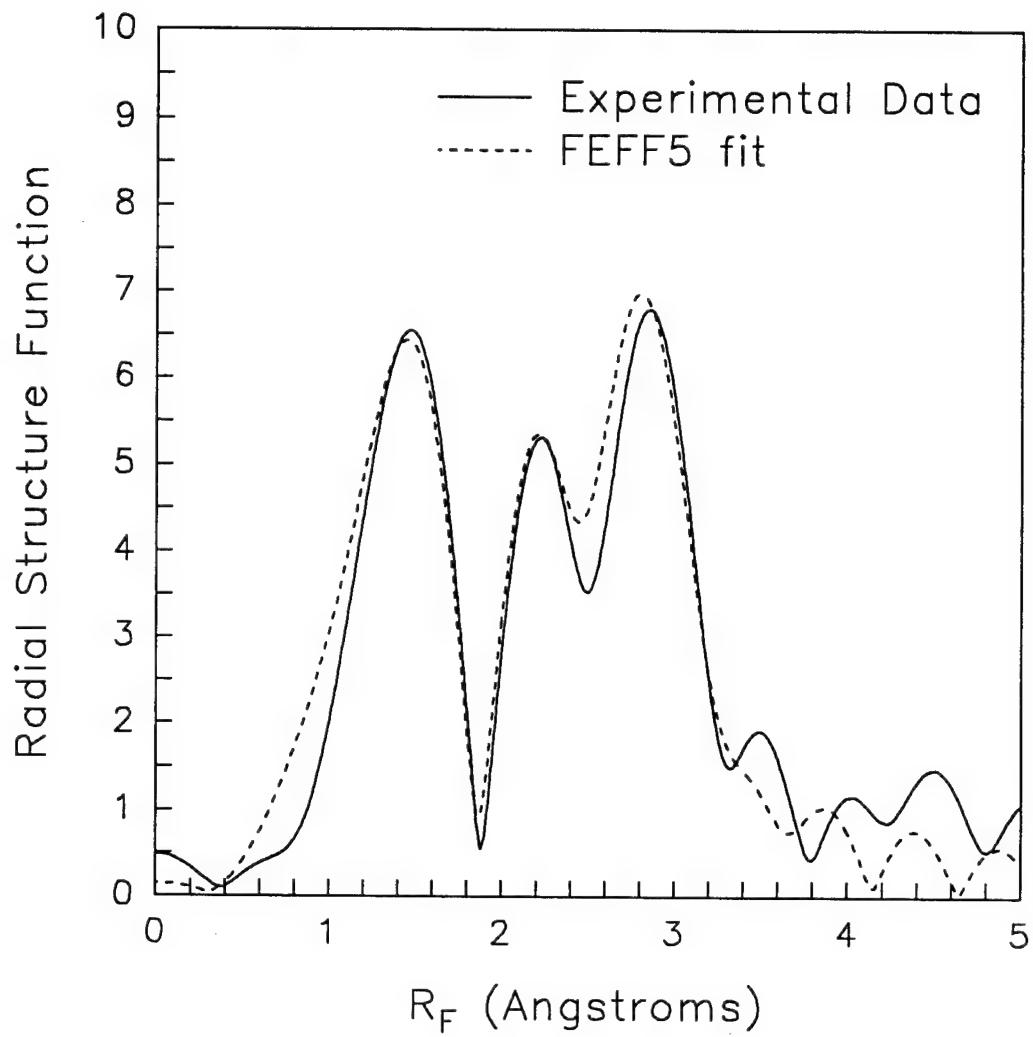
Figure IV-8. Comparison of RSFs for experimental data of CBr_4 and the FEFF5 fit using the parameters listed in Table IV-1.
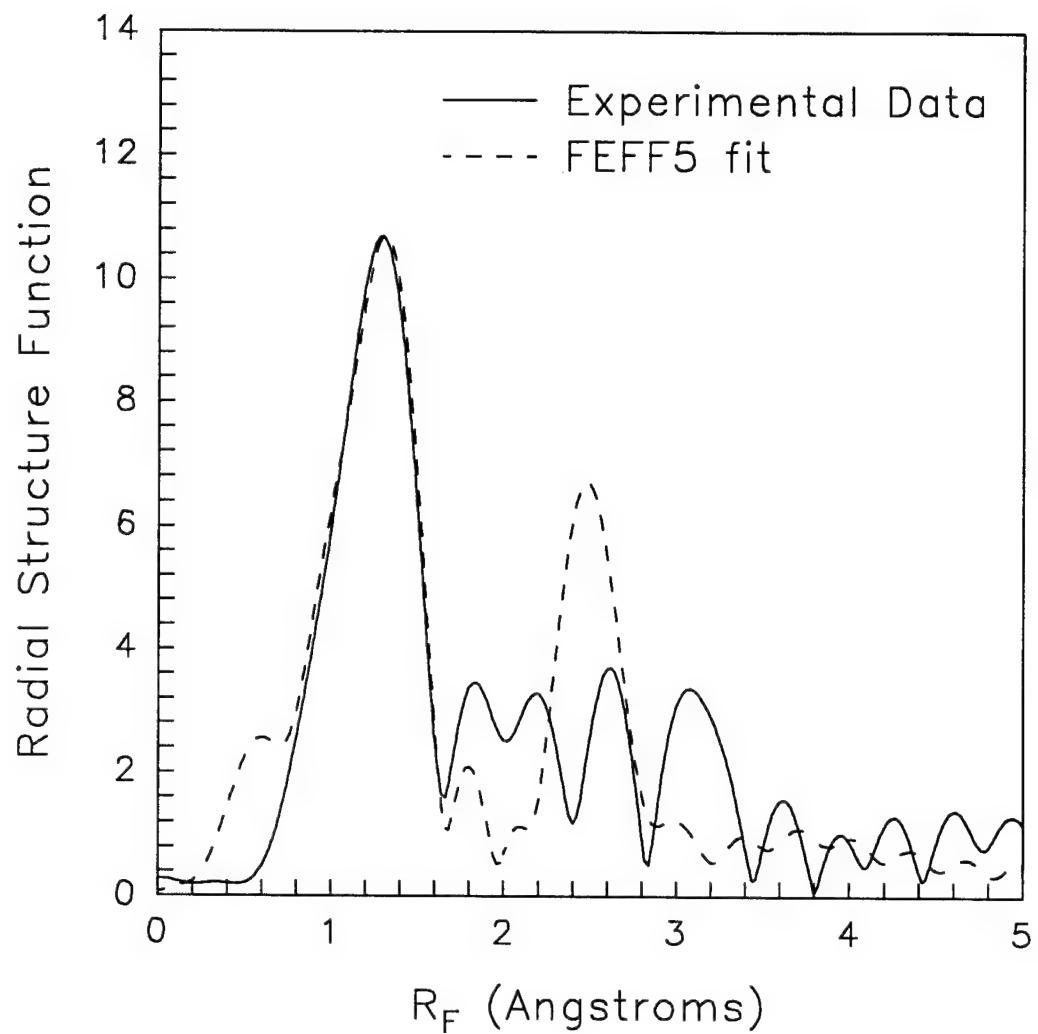
Figure IV-9. Comparison of RSFs for experimental data of $NaBrO_3$ and the FEFF5 fit using the parameters listed in Table IV-1.

Table IV-1
EXAFS Parameters[a] of Model Compounds

Compound and Shell	S_0^2	E_0 (eV)	R (Å)	N	σ^2 (Å²)
CBr$_4$[b]	0.85	13480			
C-Br			**1.925**	**1**	0
Br-Br			**3.126**	**3**	0.008
NaBrO$_3$[c]	0.785	13470			
Br-O			**1.65**	**1**	0.004
Br-O			**2.97**	**2**	
Br-Na			**3.82**	**1**	

[a]Parameters in bold were fixed based on published crystal structures; plain text parameters were fitted.

[b]CBr$_4$ actually has four different Br-C distances and 16 different Br-Br distances which correspond to four distinct molecules within the unit cell. One of these molecules was used in the simulation. Because the arrangements are very similar, the change in the simulated pattern was small if a different molecule was used.

[c]The second and third shells for NaBrO$_3$ did not have the same qualitative features as the experimental data as seen in Figure IV-9, therefore no fitting of these shells was performed.

EXAFS spectra of tetramethylammonium bromide were also collected. Because of time constraints, these spectra were collected at CHESS rather than SSRL. Unfortunately, the signal-to-noise ratio of the data sets was much poorer than for M-100-Br and the other model compounds, so data sets for $N(CH_3)_4Br$ were truncated at $k=8$ Å^{-1}. Radial structure functions for two different samples are shown in Figure IV-10. The relative error was quite large, but a quick inspection of the ordinate scale indicates that the amplitude of the EXAFS oscillations were extremely small. The reproducibility of the position and number of peaks indicates that the features in the RSFs are real, but the rather large differences in relative intensities of the peaks are a result of the error associated with the extremely weak EXAFS signals.

The interpretation of the spectra in Figure IV-10 presents quite a problem. According to the published crystal structure,[103] the first shell for bromine should be comprised of three carbons at a distance of about 2.9 Å. FEFF5® simulations indicate that the Br-C distance in Figure IV-10 is approximately 1.95 Å, which is nearly identical to the ionic radius of Br⁻, and very close to the Br-C distance in CBr_4. Based on the good agreement of simulations in the other two standards, it is extremely unlikely that FEFF5® is in error. Another possibility is that the crystal structure may be incorrect. For this compound, WAXS is only sensitive to Br atoms since the scattering power of bromine is much higher than that of carbon or nitrogen. Therefore, the Br-C crystallographic distance in Reference 103 was inferred from the unit cell of the atoms coupled with the position of the bromine atoms. Raman spectra of tetramethylammonium salts have shown that the $N(CH_3)_4^+$ tetrahedral is greatly distorted after the introduction of halide atoms,[104]
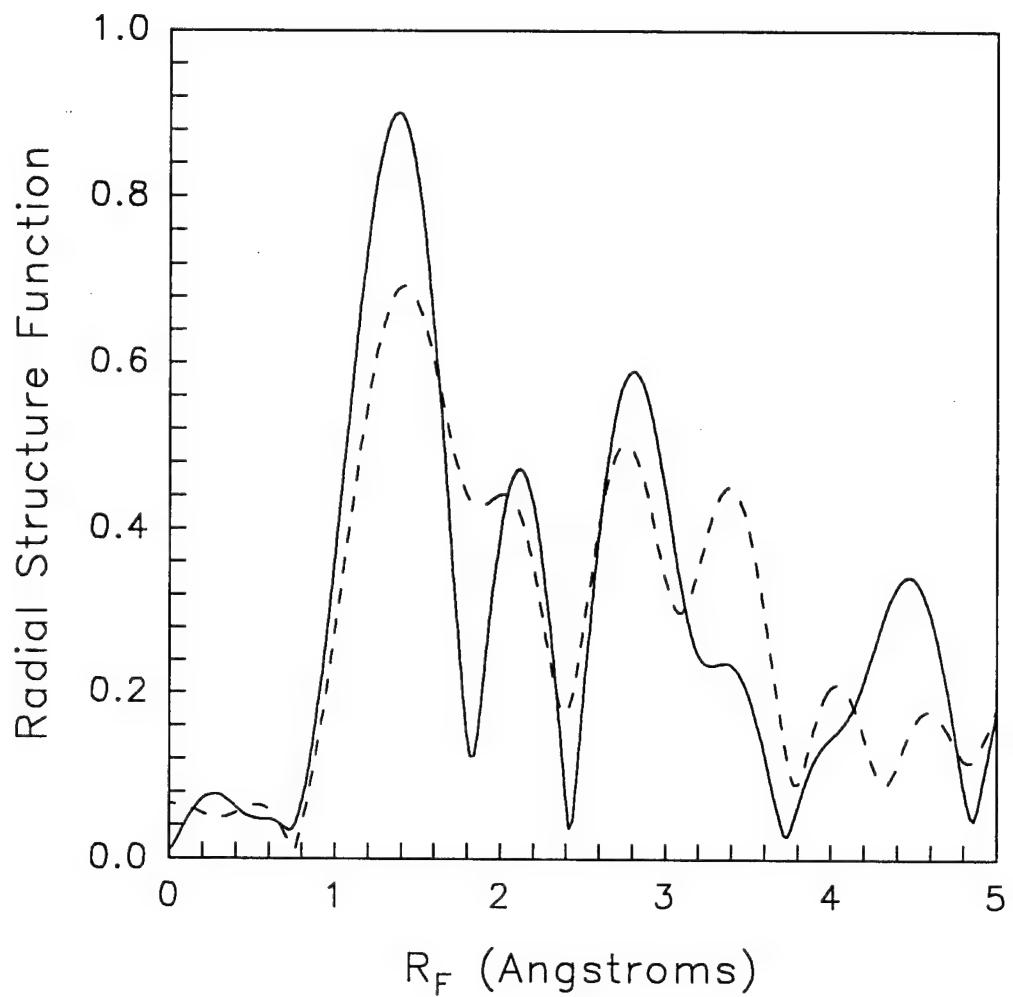
Figure IV-10. RSF for two samples of $N(CH_3)_4Br$ from data collected at CHESS. Different line styles are used only to improve viewing.

which supports the hypothesis that the simple interpretation of the WAXS patterns may led to an incorrect Br-C distance. The EXAFS results of both $N(CH_3)_4Br$ and M-100-Br suggest that the C-Br distance may be much closer than previously thought, and the bond between bromine and the tetramethylammonium group must be at least partially covalent, which is not inconceivable on the basis of the Raman results. The experimentally observed second-shell distance of 2.8 Å is reasonable for the distance between bromine and the ammonium nitrogen, given a first-shell distance of 1.95 Å.

However, the fitted value of $S_0^2=0.07$ is much too small to suggest that this simple interpretation is correct. The reasonable values of S_0^2 obtained for the other standards again suggest that software error is unlikely. Another explanation would be that a small percentage (about 10%) of the bromine atoms are in the postulated covalent-bonded structure, while the remainder of the atoms are in the published crystal structure having ionic character. This model cannot fully describe the experimental results either, since a Br-C distance of 2.9 Å for the 90% of the molecules in an ionic configuration would produce a large peak near the observed second-shell peak, and thus S_0^2 still would have to be extremely small. A plausible explanation is that the Br-C bond has both covalent and ionic character, with rapid fluctuations between the two structures. As shown by Stern et al.,[98] an atom which hops between sites will not exhibit EXAFS oscillations since the analysis does not include data near zero wavenumber. However, such a model is not easily simulated, and thus at this time the extremely small amplitude reduction factor remains unexplained. The important conclusions for this investigation are that the peaks in the $N(CH_3)_4Br$ standard are real, the peaks in the standard and

M-100-Br are close to the same positions, and the peak heights for both the standard and the cationomer are much smaller than predicted.

The data used to create Figure IV-3 were truncated at k=8 Å^{-1}, and a RSF was created to compare the N(CH$_3$)$_4$Br standard with the cationomer. As shown in Figure IV-11, the first-shell peak is in the same position in both spectra, but the second-shell peaks are shifted. As discussed previously, the data quality for the standard is poor, and this undoubtedly accounts for some of the shift. The presence of water in the cationomer would also shift the second peak position, as will be discussed below. Without better quality data for the standard, the difference in peak heights between the cationomer and the standard cannot be addressed. From the chemical structures, one would predict that the local environment in the cationomer and standard are nearly identical, but the stronger oscillations in the cationomer could indicate differences more substantial than expected.

B.4. Simulated spectra of M-100-Br. The first shell in the cationomer is probably composed of carbon. On the basis of stoichiometry and tetrahedral symmetry, one would expect three carbon atoms per bromine atom. Simulations indicate that if the first shell is composed of carbon, there are 0.5 carbon atoms for every bromine atom. Therefore, FEFF5® simulations of a hypothetical Br-C first shell do not agree completely with the experimental RSF; however, the choice of any other atom in the first shell also suffers from this discrepancy in peak heights. In addition, the width of the first-shell peak, particularly the marked asymmetry towards higher R$_F$, indicates at least two different Br-C distances. Based on the peak and shoulder positions, the range in the Br-C
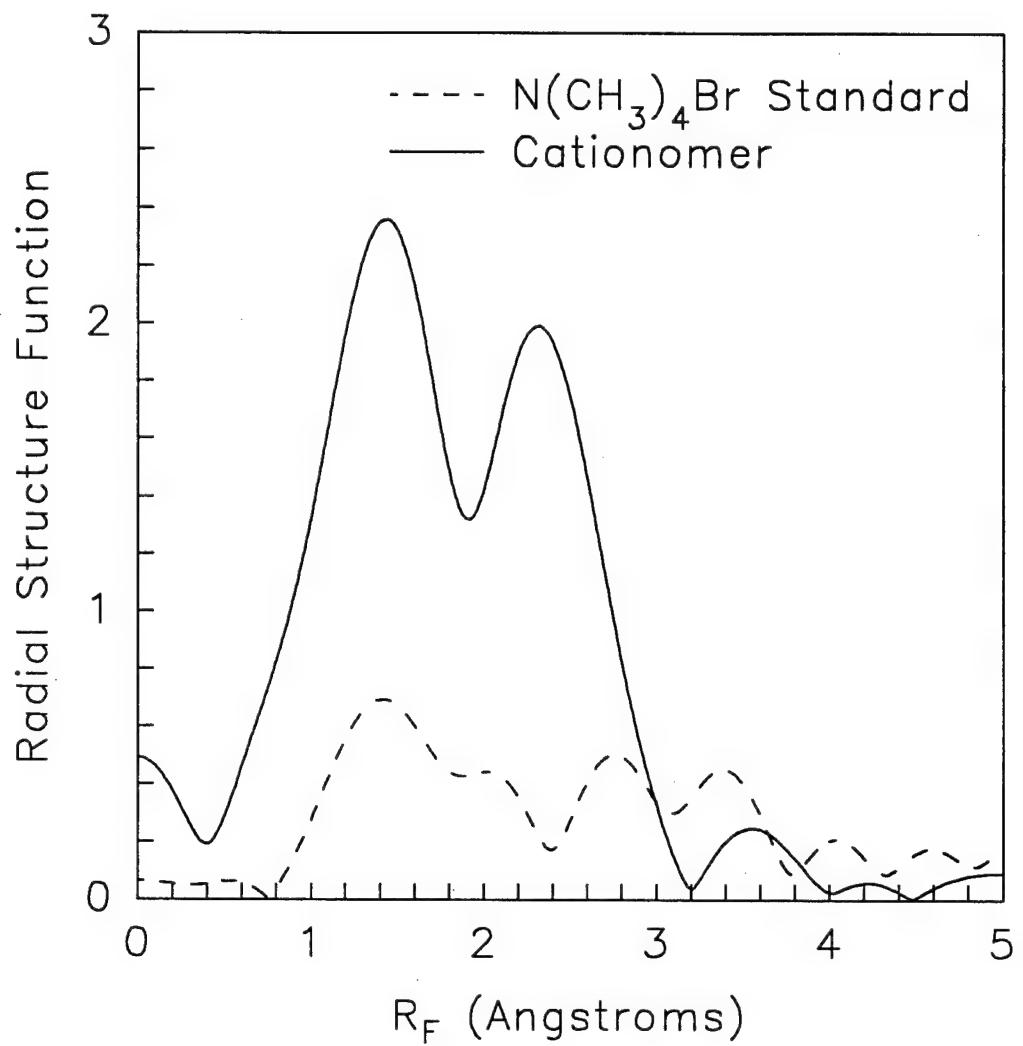
Figure IV-11. Comparison of the RSFs for M-100-Br and $N(CH_3)_4Br$. The RSF for the cationomer is not identical to Figure IV-3 because the raw data were truncated at $k=8Å$ for this figure.

distance seems to be 1.92 to 2.05 Å. Figure IV-12 shows a simulation of three carbon atoms at 2.02 Å with a second shell consisting of one Br-N atom at a distance of 2.33 Å, which is the absolute minimum distance for Br-N based on space filling calculations using published C-N bond distances and the proposed distance to the first shell.

In the second shell, simulations demonstrate that Br-C, Br-N and Br-O all produce RSF peaks at nearly the same R_F for a given R. Since carbon, nitrogen and oxygen are the only logical possibilities for the second shell, the middle of the broad second shell corresponds to a distance of approximately 2.8 Å. The width of the second-shell peak suggests that either the second shell is composed of one atom at more than one distance, or more than one type of atom. The discussion that follows shows that the second-shell peak of the RSF results from at least two different types of atoms, one of which is oxygen from water. A Br-O distance of 2.8 Å is reasonable given the respective radii of water and bromine.

B.5. Vacuum drying experiments. As previously discussed, the changes in the EXAFS spectra of M-100-Br with temperature can not be rationalized by ionic crystallite melting, but appear consistent with water evaporation. An incomplete understanding of the cation local environment hinders proof of the supposition that the room temperature annealing peak results from water absorption. To further prove this hypothesis, a sample was allowed to anneal in a desiccator for approximately 9 months. The sample was then dried for one week in a vacuum oven at approximately 1 torr and 20°C, which is below the annealing endotherm. Since the melting process is essentially independent of pressure in the range 1-760 torr, one would expect no change in either the EXAFS spectra or DSC
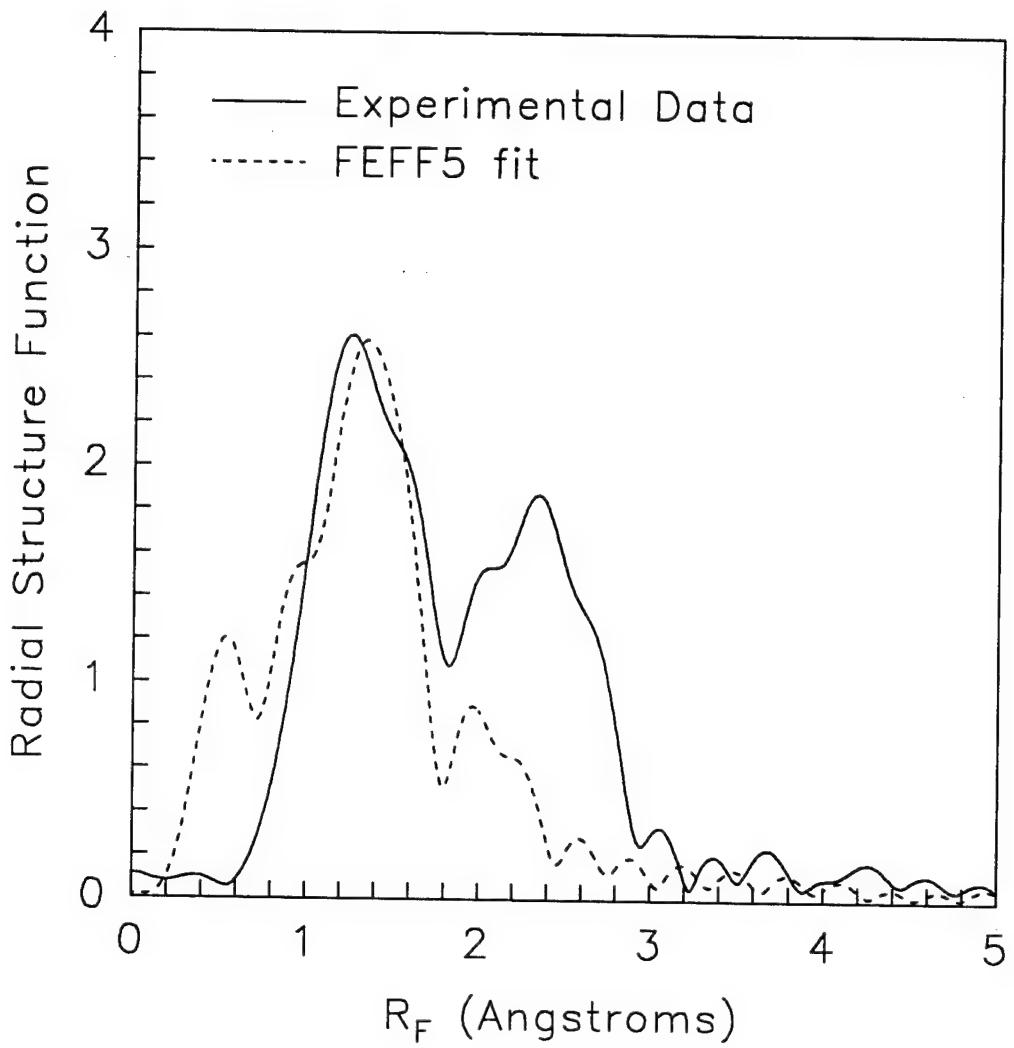
Figure IV-12. FEFF5 simulation of the RSF in Figure IV-3 using a Debye-Waller factor of 0.005 for both shells and $S_0^2=0.13$. To match intensities of the first-shell peak, an atypical value of S_0^2 was used in simulations. As discussed in the text, the RSF peak heights of both M-100-Br and the model compound $N(CH_3)_4Br$ were lower than predicted.

thermograms after this treatment if the transition were due to ionic crystallite melting. In order to facilitate mass transfer of water, the sample was prepared in the form of flakes rather than compression molded discs. As shown in Figure IV-13, EXAFS patterns collected at CHESS of the cationomer before and after vacuum drying at 20°C agree qualitatively with data collected at SSRL as a function of temperature. Specifically, the second-shell peak decreased in magnitude upon vacuum drying or upon heating, while the first-shell peak was essentially unchanged. The peak positions for both shells shifted more for the vacuum dried sample than the heated sample. A higher initial water content for the sample in the vacuum drying experiment, as indicated by the ratio of the first- to second- shell peak heights in Figure IV-13 as compared to Figures IV-4 and IV-5, could explain the less pronounced shifts for the heated sample. The dramatic position shift of the second-shell peak before and after vacuum drying also supports the premise that the second shell in Figure IV-3 is due to at least two atoms.

Even more convincing that the room temperature annealing peak was due to water comes from the result that no endothermic peak was found in DSC scans of the vacuum dried material. Finally, a weight loss of 0.84% was measured after drying, which corresponds to 0.5 H_2O molecules per bromine atom. The RSF peak height of FEFF5® simulations for a Br-O coordination shell located at 2.8 Å, with 0.5 oxygens for every bromine atom, was consistent with Figures IV-3 and IV-13 using reasonable values for the Debye-Waller factor and S_0^2. Therefore, in spite of the questions concerning the underlying structure, these findings conclusively show that the room temperature annealing peak in these cationomers is caused by water absorption.
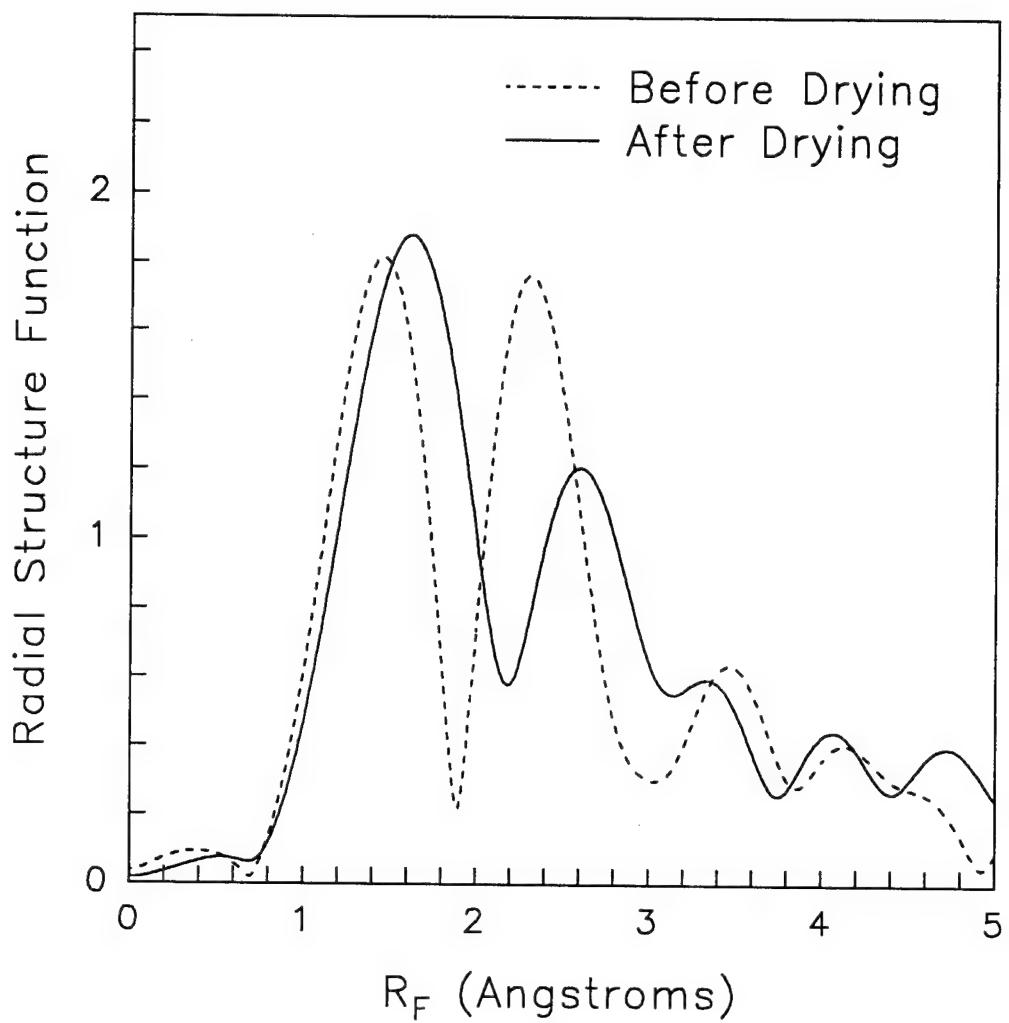
Figure IV-13. RSF of M-100-Br before and after drying for 1 week in a vacuum oven at room temperature and approximately 1 torr.

B.6. Second look at previous E-MAA ionomer studies. In light of the conclusion that the room temperature annealing peak of the polyurethane cationomers results from water absorption, data presented in References 81-91 and 96 were reexamined. Certain observations in those papers also seem to support a mechanism of water desorption rather than ionic crystallite melting as the cause of the endotherm.

More specifically, (1) when E-MAA was annealed at room temperature, a DMTA transition in E" coincident with the DSC endotherm appeared, but did not appear after annealing at -5°C.[88] Since there is no evidence of a change in the structural state of E-MAA between the two temperatures, this result is difficult to rationalize in terms of crystallite melting. However, if water absorption was the cause, then the low absolute humidity of air at -5°C could explain the absence of the DMTA transition at this temperature.

(2) The temperature of the annealing endotherm in E-MAA was essentially independent of the type of metal cation. If the endotherm is due to ionic crystallite melting, then one would expect some dependence on metal cation type, since the melting point of similar small molecule compounds consistently varies with the metal cation. For example, the oxides of sodium, copper, zinc and magnesium melt at 1275, 1326, 1975 and 2850°C, respectively. Similarly, the carbonates of lithium, sodium and potassium melt at 723, 851 and 891°C, respectively. If the endotherm were due to water absorption or crystallization of methylene segments, as proposed in the revised model,[96] then the temperature of the transition would likely be independent of the metal cation type and fall in the observed range of 50-80°C.

(3) The addition of BAC increased the area of the DSC endotherm.[81] Because of its amino groups, BAC would selectively partition to the ionic aggregates. It is difficult to explain how a bulky organic molecule increases the crystallinity within an aggregate but does not change the melting point, which must occur if the endothermic transition is attributed to ionic crystallite melting. In terms of water absorption, addition of BAC reduces the packing density of the aggregates and provides two amine sites that energetically favor water. Both factors would increase the affinity of the ionomer for water, and tend to support a hypothesis of water absorption rather than ionic crystallite melting as the cause of the room temperature annealing endotherm in E-MAA ionomers.

However, not all the results in these previous references support water absorption. Perhaps the strongest evidence against this interpretation was the dramatic change which occurred after cold drawing of annealed E-MAA.[89] Both the position and the area of the endothermic peak decreased substantially after cold drawing, which seems inconsistent with water absorption. Also, the recent introduction of a microcrystalline model that includes contributions from methylene sequences[96] raises possibilities not addressed in this investigation. With a more complex morphology which includes matrix crystallinity, more than one process may occur in E-MAA ionomers when annealed at room temperature, including secondary crystallization of the matrix and water absorption. Unfortunately, EXAFS may be of little use in analogous investigations of E-MAA ionomers, since the carboxylate oxygen atoms are likely not distinguishable from the oxygen atoms of water.

C. Summary

Temperature-dependent EXAFS studies of M-100-Br have shown that a DSC endotherm centered near 60°C, which appeared when the cationomer was annealed for a few weeks at room temperature, correlated with a change in the second shell of the local environment surrounding bromine, while the first shell was unaffected. Although the details of the local environment could not be fully explained, EXAFS results indicated that water was leaving the second coordination shell of the anion. When the cationomer was vacuum dried at a temperature below the endotherm, a small but measurable weight loss was found. Drying the sample in this manner also eliminated the DSC endotherm, and produced EXAFS spectra qualitatively similar to those obtained during heating. These results strongly suggest that the endothermic peak contains contributions from the energy change associated with water vaporization along with the energy change associated with water leaving the immediate coordination environment of the bromine ion.

Elimination of ionic crystallite melting as a probable mechanism for the room temperature annealing endotherm is important to the fundamental understanding of PU cationomers, since formation of ionic crystallites would necessitate the presence of ionic aggregates, and all other evidence in this thesis indicates that the ionic groups of PU cationomers do not aggregate. This study also emphasizes the extreme hydrophilicity of ionomers, since the observed water absorption occurred in samples stored over dry calcium sulfate. Such water sensitivity has also been noticed in EXAFS studies of carboxy-telechelic polyisoprenes[105] and sulfonated polyurethane ionomers.[106]

Chapter V. Fourier Transform Infrared Temperature Studies

A. Introduction

In Chapter III, the morphology and properties of the PU cationomers were investigated. Results showed that the bulky pendant groups, attached to asymmetric carbon atoms, prevented crystallization in the hard domains. Consequently, little or no phase separation was evident in the unionized polymers. On quaternization, dramatic improvements in phase separation and mechanical properties were observed. The Young's modulus and tensile strength were found to increase by as much as two orders of magnitude, and the temperature at which the polymer underwent viscous flow was increased by over 100°C. Although differential scanning calorimetry and dynamic mechanical analysis suggested that ionic interactions were the primary driving force for phase separation in the cationomers, results of small-angle X-ray scattering and tensile testing indicated a lamellar morphology typical of conventional polyurethanes with semi-crystalline hard segments. Further, there was no evidence of ionic aggregation within the lamellae. This led to the question: If ionic functionality is responsible for the tremendous improvement in mechanical properties, but there appears to be no ionic aggregation, what are the specific interactions or physical crosslinks in these materials?

Specific interactions in polyurethanes, particularly hydrogen bonding, have been extensively studied using infrared spectroscopy. Investigators have sought correlations between the type or extent of hydrogen bonding in the polyurethane and its molecular structure,[107-117] degree of phase separation,[109,112,115,117,118-123] response to deformation,[111,118,124,125] or thermal transitions.[110,113,115,121,126-129] Knowing the specific

location along the polymer chain of the various functional groups that participate in hydrogen bonding makes such investigations possible. In conventional segmented polyurethanes, the hydrogen atom of the N-H group in the urethane linkage is the proton donor. A number of proton acceptors are usually present including the urethane carbonyl and alkoxy oxygens, and ester or ether groups which may be incorporated in the soft segments. Hydrogen bonds are indicated by a shift in the stretching frequency of the proton donor or acceptor to lower energy versus the value observed when the group is "free" (i.e. not hydrogen bonded).

Far fewer infrared studies have been performed on PU cationomers. Dietrich *et al.*[26] noted a shift of the N-H band in a segmented PU cationomer to lower frequencies on quaternization, and suggested the shift was likely attributable to an increase in the number of hydrogen bonds formed, as coulombic forces aligned the urethane linkages of neighboring polymer chains. In a study of oligourethanes with terminal amine groups, Lipatov and co-workers[34] reported similar infrared results. In addition to a frequency shift of the N-H band, they observed that on ionization a high fraction of N-H groups remained hydrogen bonded, while most of the carbonyl groups became free. Although quantitative interpretation of the spectra was not attempted, the results supported a redistribution of N-H hydrogen bonds from the urethane carbonyl to the iodine ion. In a later paper on multiblock PU cationomers,[33] they postulated a wide array of interactions that included ionic aggregation, N-H to anion bonding, and attractions between the positive charge of the ammonium group and urethane carbonyls. In a number of PU cationomers, Chan and Chen[38-41] noted similar changes in the N-H and carbonyl regions

on quaternization. However, interpretation of the carbonyl band was complicated by contributions from the glycolate ion used to neutralize the quaternary amine.

In this Chapter, Fourier transform infrared (FTIR) temperature studies were completed on the M-###-I polyurethane cationomers. Spectral deconvolution was used to obtain semiquantitative information on the distribution of hydrogen bonds as a function of temperature and ion content. The results for each polymer were related to its chemical structure, thermomechanical properties, and morphology. Such information was used to gain further insight into the nature of the specific interactions, the arrangement of ions within the lamellae, and the mechanism of the upper transition in dynamic mechanical thermal analysis.

B. Results

Room temperature spectra for the M-###-I cationomers are shown in Figure V-1. Close examination of the spectra reveals that on ionization no new vibrations, only relative changes in intensity or position of bands, are observed. Two main spectral regions are of interest in this study; N-H stretching from 3150 to 3500 cm^{-1}, and the amide I absorption band (commonly referred to as carbonyl stretching) from 1650 to 1800 cm^{-1}. In this section, the effect of temperature on the two spectral regions is presented. Results are then discussed for each polymer in terms of its chemical structure and morphology.

B.1. N-H Stretching Region. FTIR spectra of the N-H stretching region, obtained during heating from 30-180°C, are shown for each of the three PU cationomers

101
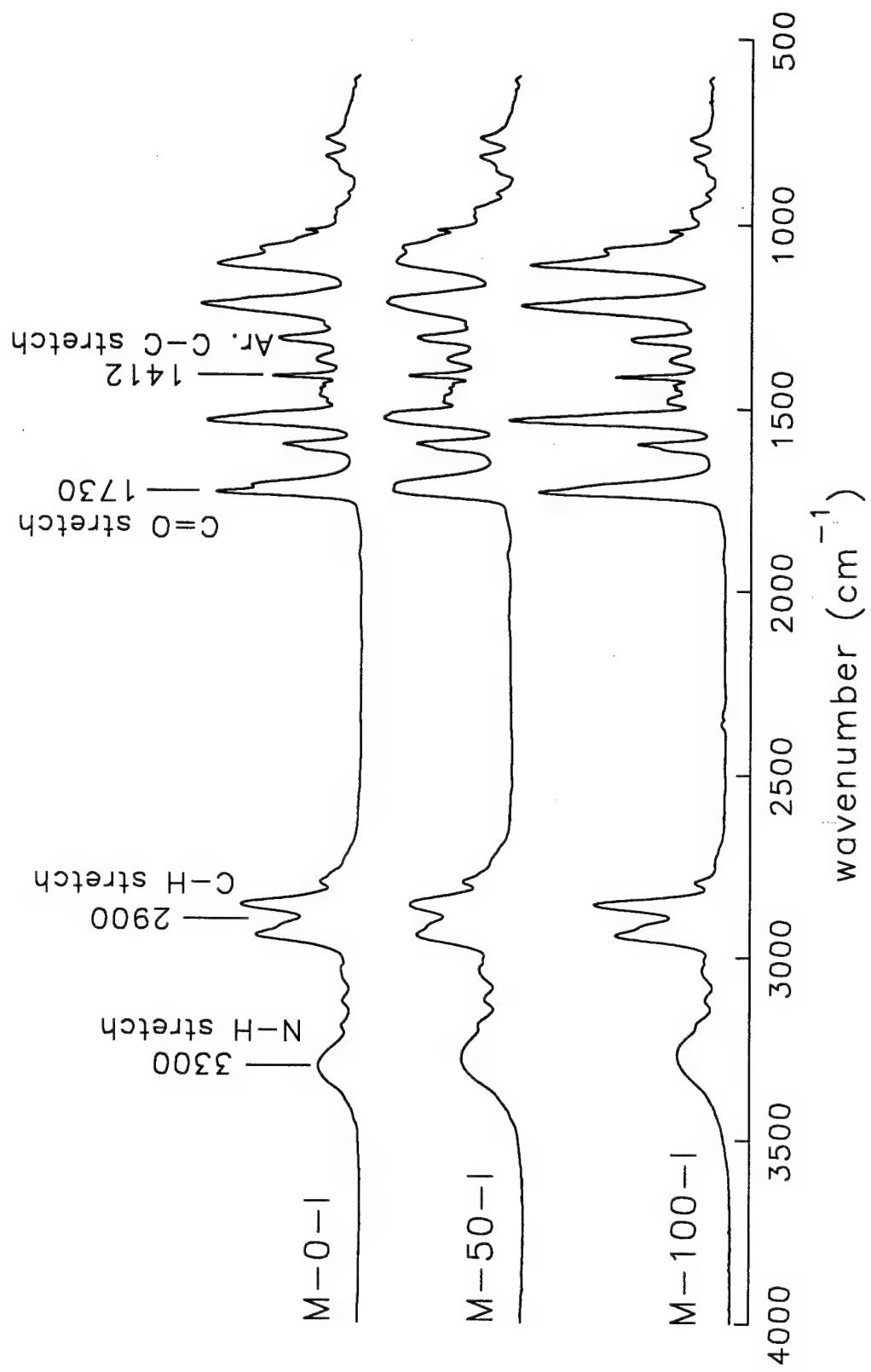
Figure V-1. Room temperature spectra of the cationomers with pendant trimethylammonium groups as a function of ion content.

in Figures V-2 to V-4. Looking first at the room temperature spectrum of sample M-0-I, one can readily identify at least four bands. The broad absorption centered at approximately 3300 cm^{-1} is assigned to hydrogen bonded N-H groups, while the free N-H stretch appears as a small shoulder at 3445 cm^{-1}. Bands at 3400 and 3180 cm^{-1} are attributed to overtones of fundamental vibrations in the carbonyl region. Again looking at only room temperature spectra, the hydrogen bonded band broadens and shifts to lower frequencies with increasing ion content. This shift in position of the band maximum corresponds to an increase in the average strength of the hydrogen bond at higher ion concentrations.

For the unquaternized polymer M-0-I, Figure V-2 shows that the band associated with hydrogen bonded N-H groups broadens and shifts to higher frequency as the temperature increases. A substantial decrease in band area is also evident. Similar trends have been observed in model polyurethane hard segments,[121,130] and in segmented polyurethanes with amorphous[127] or semi-crystalline[125-127,129] hard segments. A clearly different behavior is observed in the quaternized polymers, M-50-I and M-100-I, of Figures V-3 and V-4, respectively. At intermediate temperatures, one can see that the broad band earlier attributed to hydrogen bonded N-H groups is in fact two bands. The position of the band at higher wavenumbers matches closely that observed in a variety of non-ionic polyurethanes, and will be referred to hereafter as a "traditional" hydrogen bond. The second band, lower in frequency by some 50-100 cm^{-1}, is assigned to N-H stretching where the N-H groups are hydrogen bonded to the iodine anion. A lower frequency vibration is consistent with this assignment, since a greater hydrogen bond
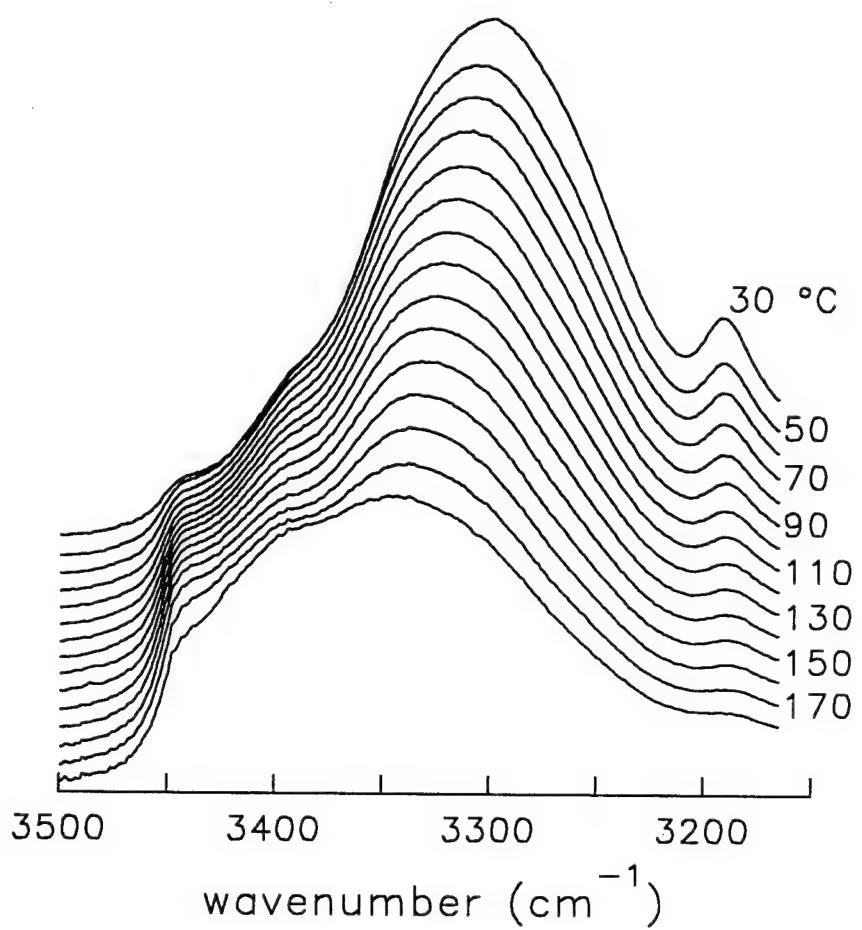
Figure V-2. FTIR spectra of M-0-I in the N-H stretching region as a function of temperature from 30 to 180°C.
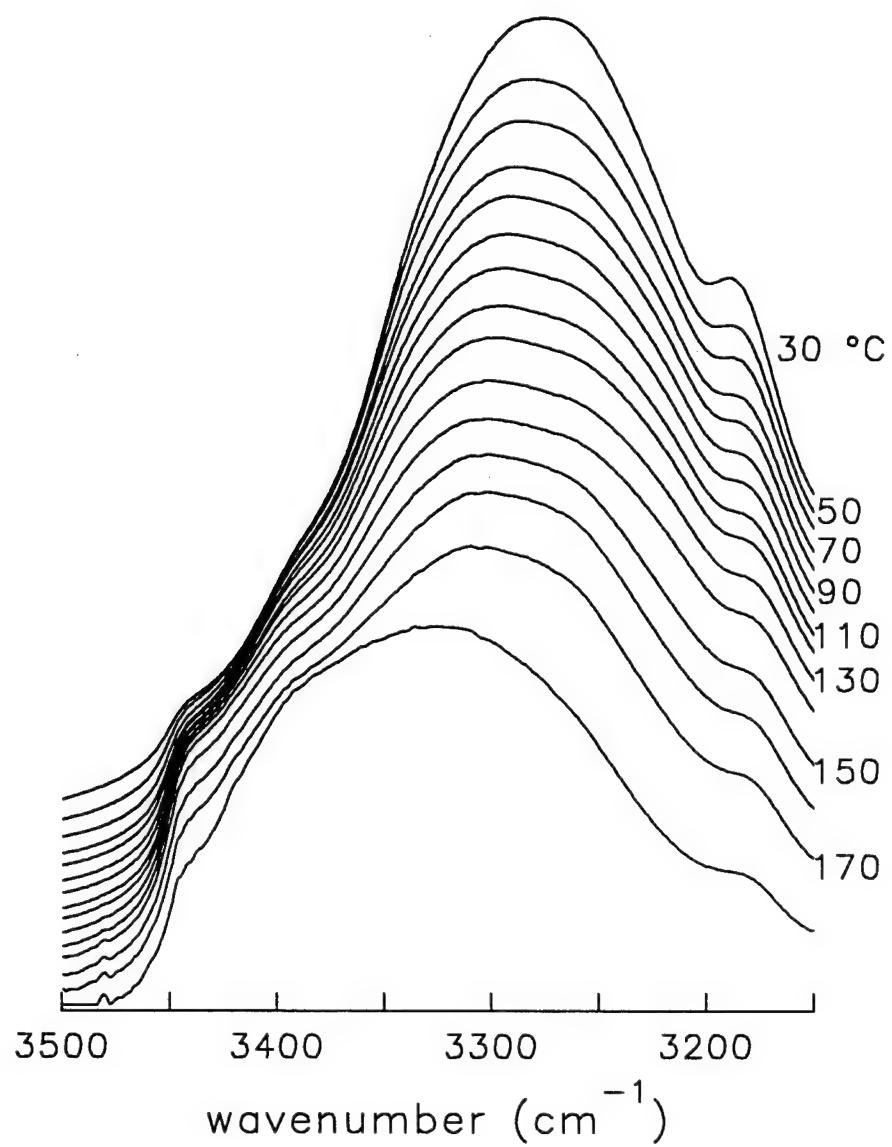
Figure V-3. FTIR spectra of M-50-I in the N-H stretching region as a function of temperature from 30 to 180°C.
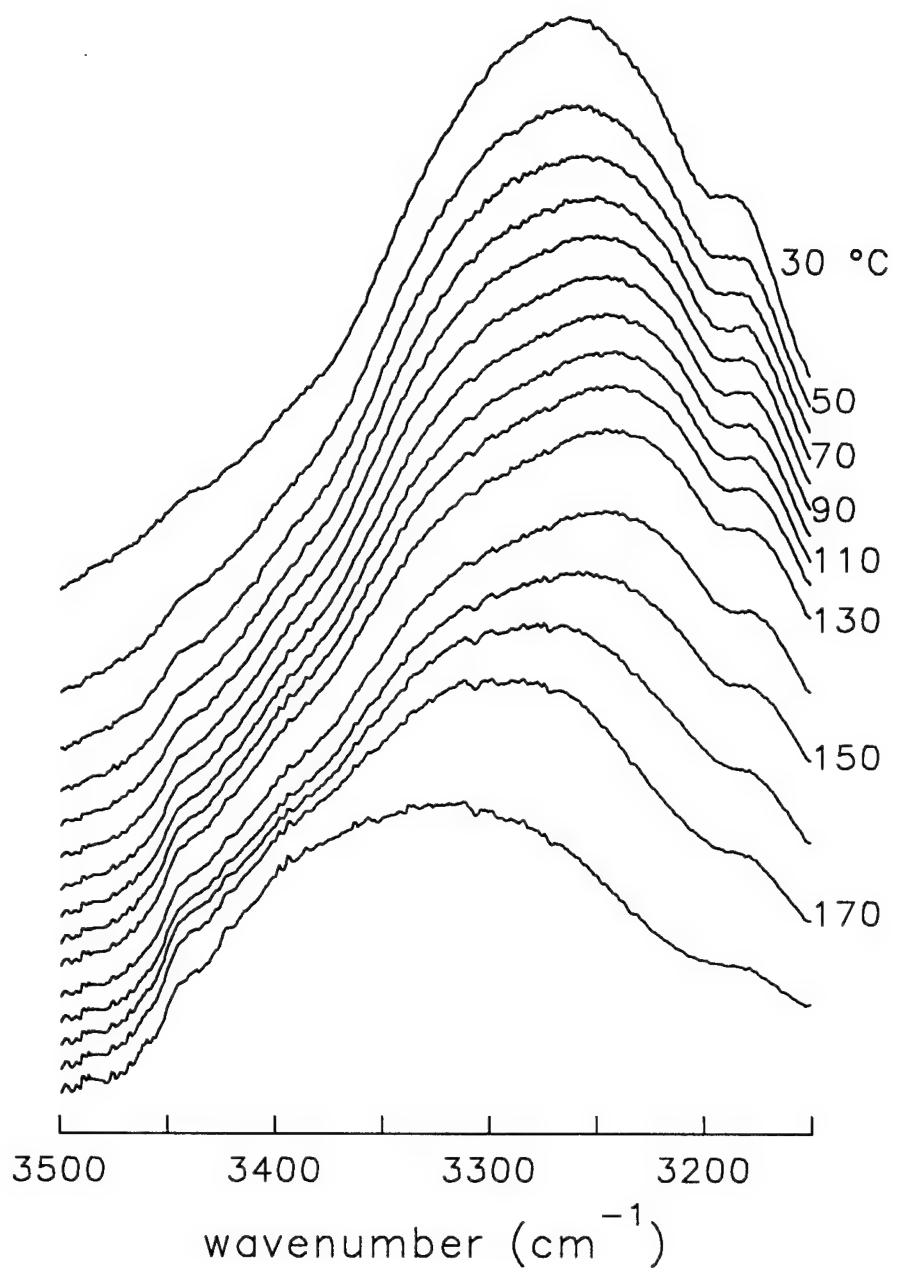
Figure V-4. FTIR spectra of M-100-I in the N-H stretching region as a function of temperature from 30 to 180°C.

energy would be expected with a halide ion as compared to carbonyls or ethers. An analogous shift has been reported for hydrogen bonding of alcohols to low molecular weight compounds containing halide ions.[131,132] Band assignments for the N-H region (and the carbonyl region discussed below) are summarized in Table V-1.

Reversibility of the results of Figures V-2 to V-4 was tested by heating samples to 180°C, and acquiring spectra on cooling. As shown in Figure V-5 for M-100-I, the process is clearly not reversible from 180°C. In fact, the N-H region of the final spectrum at 30°C resembles an initial spectrum of M-0-I more closely than an initial spectrum of M-100-I. Not surprisingly, dequaternization was verified in the PU cationomers at elevated temperatures through measurement of the iodine content, as shown in Chapter VI. The N-H stretching region of the infrared spectrum appears to be very sensitive to even small levels of dequaternization. Figure V-6 shows a mere 2% weight loss for the cationomer M-100-I in thermogravimetric analysis up to 200°C. Since the time scale of the FTIR cooling experiment and TGA are comparable, the dramatic difference between the initial and final spectra of Figure V-5 is therefore likely accompanied by a loss of no more than 15% of the ammonium groups. Through trial and error, the maximum temperature for complete reversibility of the observed changes in infrared spectra during heating was determined. As shown in Figure V-7, spectra obtained during cooling the PU cationomers from 140°C closely match those obtained during heating at all temperatures.

Deconvolution of the N-H stretching region was completed on spectra up to 140°C using the curve-fitting program PeakFit® available from Jandel Scientific. Limits of the
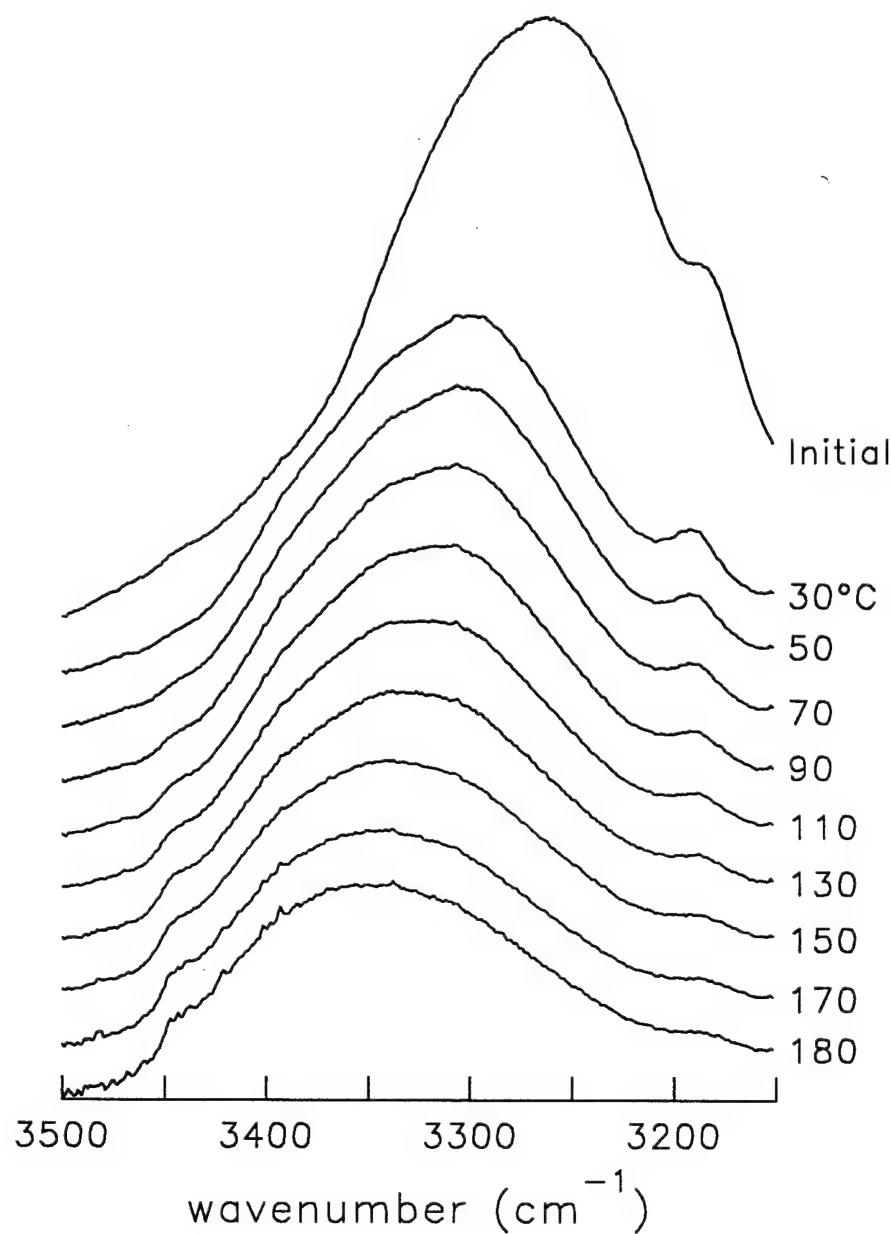
Figure V-5. The N-H stretching region of M-100-I recorded as a function of decreasing temperature from 180°C. An 'Initial' spectrum of M-100-I, taken at room temperature prior to heating, is included for comparison.
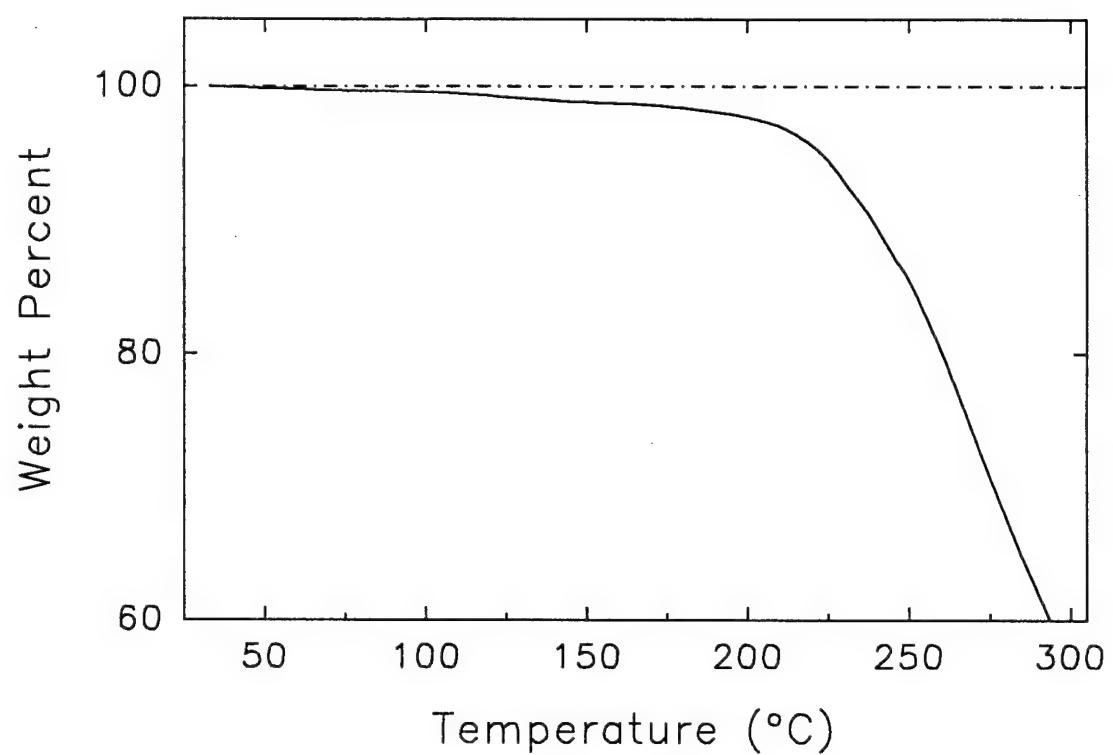
Figure V-6. Thermogravimetric analysis of the cationomer M-100-I in dry nitrogen at a scan rate of 3°C per minute.
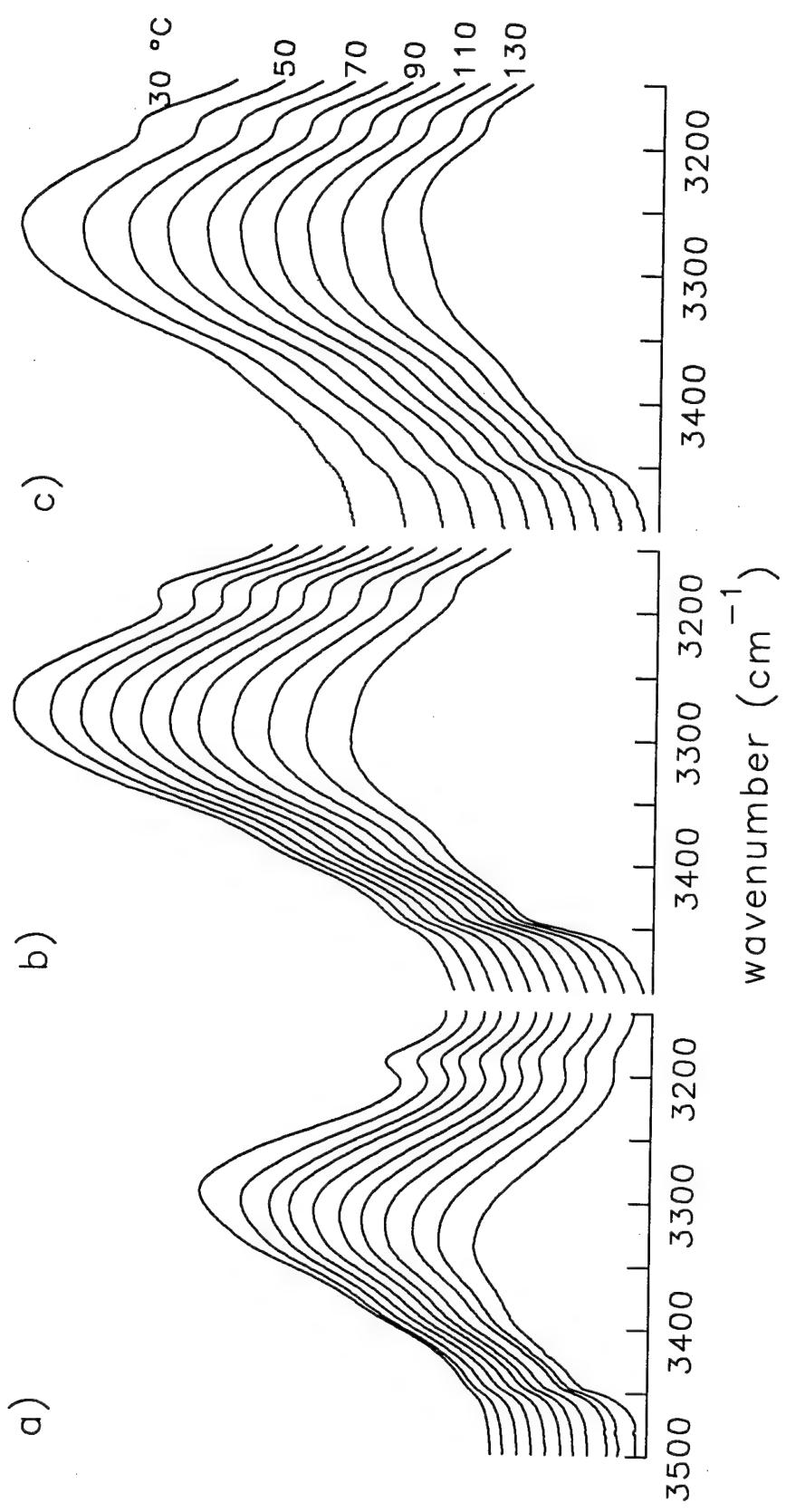
Figure V-7. FTIR spectra in the N-H stretching region for a) M-0-I, b) M-50-I, and c) M-100-I as a function of decreasing temperature from 140°C.

Table V-1
Summary of Relevant Band Assignments

Assignment	Frequency (cm^{-1})	Occurrence
N-H stretching region	~ 3150-3500	
free N-H	3445	M-O, M-50, M-100
N-H bonded to anion	3260	M-50, M-100
N-H bonded to ether[a]	3300	M-0
N-H bonded to carbonyl	3326	M-O, M-50, M-100
C=O stretching region	~ 1650-1800	
free C=O	1736	M-O, M-50, M-100
hydrogen bonded C=O	1710	M-O, M-50, M-100
Aliphatic C-H stretching	2820-2980[b]	
Aromatic C-C stretching	1412	

[a] Band likely comprised of N-H bonded to ether and carbonyl groups.
[b] Arbitrarily defined limits of region for use in normalization.

curve-fit were set at 3250 and 3500 cm^{-1} for M-0-I, and 3210 and 3500 cm^{-1} for M-50-I and M-100-I, to avoid the low frequency overtone vibration at 3180 cm^{-1}. Gaussian functions were assumed for the three bands of M-0-I (assigned to the free and "traditional" hydrogen bonded N-H groups, and the overtone vibration at 3400 cm^{-1}), and the four bands of M-50-I and M-100-I (same three as M-0-I, plus the band assigned to N-H groups hydrogen bonded to the anion). The PeakFit® program determines the best fit of the experimental data by varying the frequency ν, width at half-height FWHM, and area of each band using the Marquardt-Levenberg algorithm. Coefficients of determination were greater than 0.999 for all three samples at all temperatures. In spite of the excellent fits (Figure V-8), quantifying the distribution of the different types of N-H groups is not possible. The absorptivity coefficient, α, of the N-H and O-H stretching vibrations has been shown to be a strong function of frequency.[130,133-136] In this study, the frequency of the vibration for bands associated with N-H groups hydrogen bonded to anions and "traditional" proton acceptors vary significantly with temperature. Also, the absorptivity coefficient likely varies enough across the frequency range of some bands that a proper shape can not be assigned, with the result that any peak deconvolution may be invalid. This was of particular concern in the present study where a number of N-H stretching bands are unusually wide. In fact, not curve fitting the N-H region at all was contemplated, since the reader may be tempted to "use the numbers" to obtain quantitative information. Hopefully the cautionary discussion above is sufficient

112
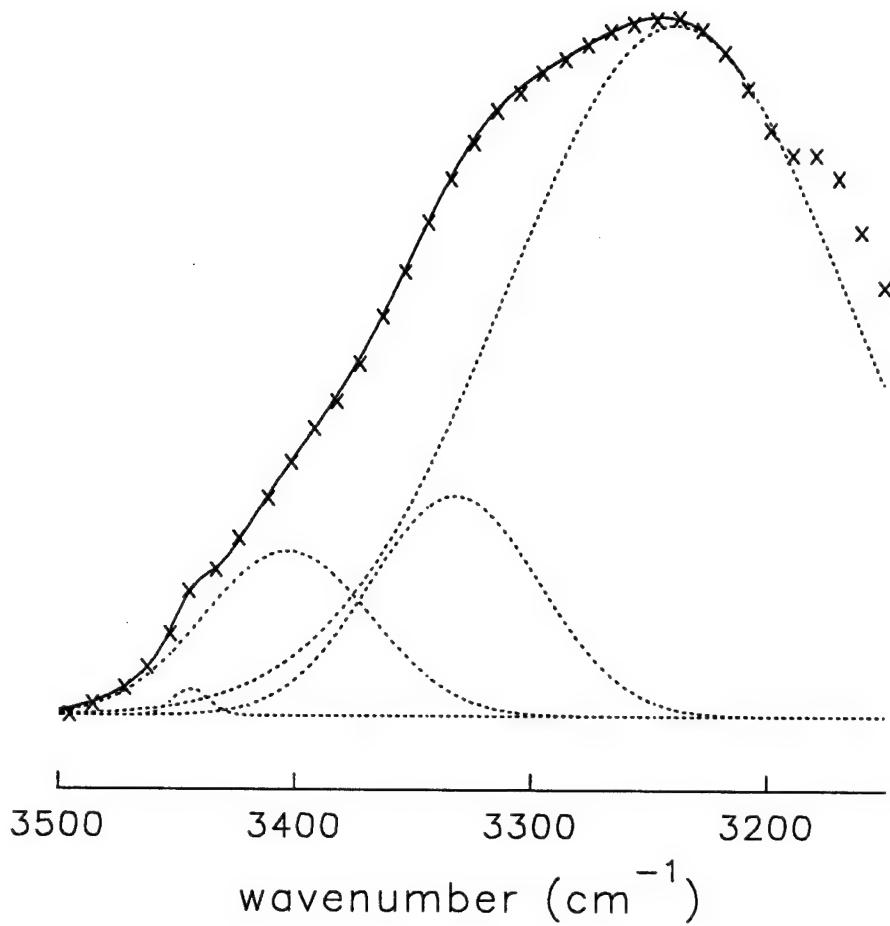
Figure V-8. Typical deconvolution of the N-H stretching region into four gaussians. The solid line is the analytical function over the limits of the curve-fitting procedure, while the x's mark the experimentally obtained absorbance every 10 cm^{-1}.

to prevent such overinterpretation of the data. With the extensive overlap of bands in the N-H stretching region, curve fitting was performed to aid the eye of the reader in seeing trends.

Optimum parameters for curve fitting the N-H stretching region of the PU cationomers from 30-140°C are given in Table V-2, with area changes displayed graphically in Figure V-9. In cases where a band contributed only a small fraction of the total N-H stretching absorbance, one or more of the band attributes were fixed to aid convergence (as indicated by an * in Table V-2). Smooth trends with temperature, and relative agreement of band positions between the different samples, impart some level of confidence in the results. The position of the high-frequency overtone is quite consistent between samples, ranging from 3401-3404 cm^{-1} at room temperature and increasing smoothly to 3410-3414 cm^{-1} at 140°C. In all three polymers, the FWHM of the overtone changes considerably with temperature, and not always in the same direction. Predicting the absorbance of two-phonon bands is difficult, so the changes in band width with temperature could be real; however, they may also be a consequence of the previously discussed limitations in curve fitting broad band shapes.

The frequency of the free N-H vibration was also relatively insensitive to temperature and ion content, varying from 3438 to 3445 cm^{-1} at 30°C and by only a few wavenumbers between 30°C and 140°C. The small absorbance of this band complicated its deconvolution in all spectra. For sample M-100-I, the FWHM ranged from approximately 14-25 cm^{-1} during a first pass of curve-fitting, displaying no clear trend with temperature. In subsequent curve-fitting of M-100-I, the FWHM of the free band
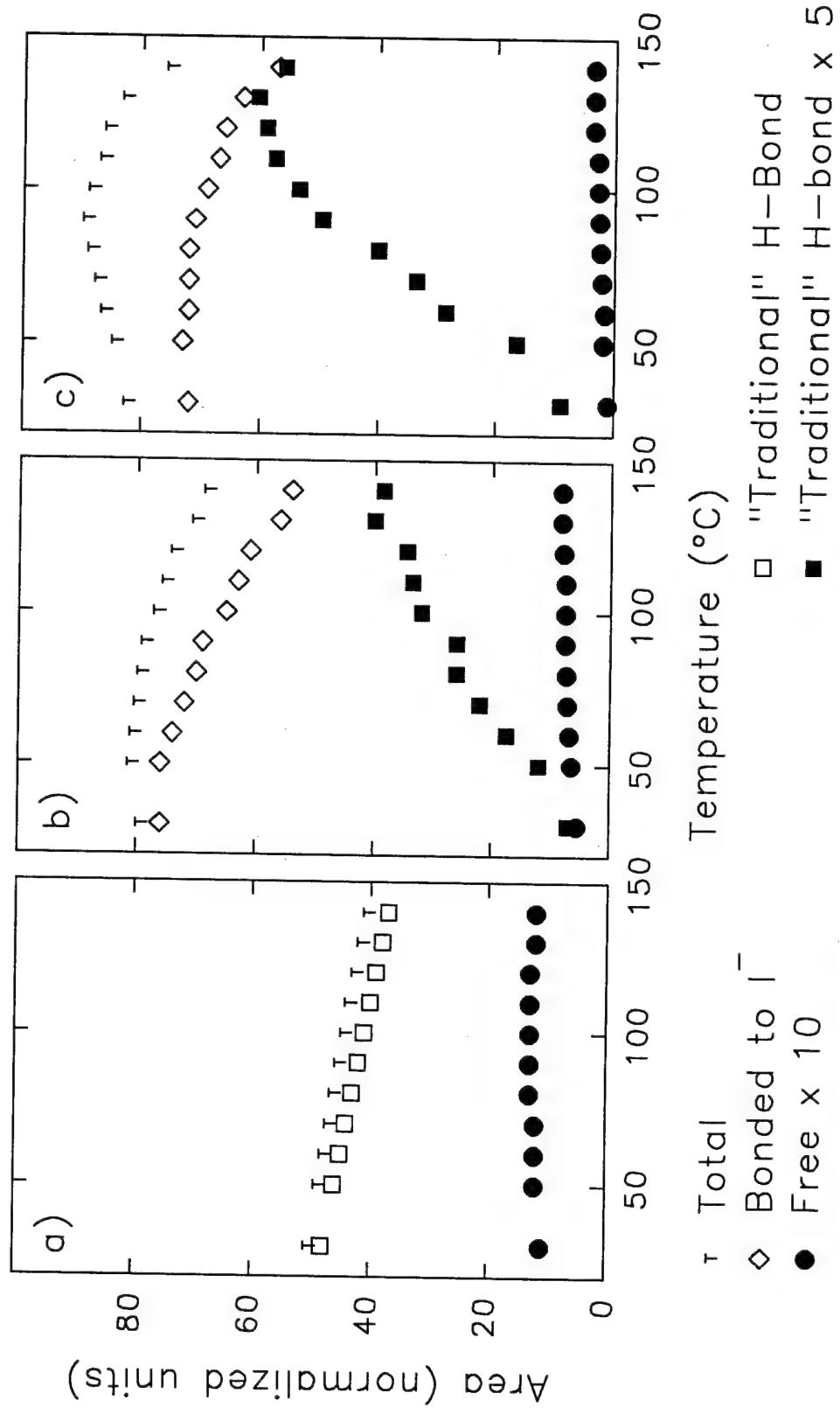
Figure V-9. Normalized areas of assigned bands in the N-H stretching region as a function of temperature from 30 to 140°C for a) M-0-I, b) M-50-I, and c) M-100-I. Note that areas for two bands have been multiplied by constants to improve intelligibility.

Table V-2
Curve-Fitting Parameters for the N-H Stretching Region

Sample	(°C)	free N-H			overtone		
		ν (cm^{-1})	FWHM (cm^{-1})	Area	ν (cm^{-1})	FWHM (cm^{-1})	Area
M-0	30	3438	39	1.1	3401	28	0.7
	50	3439	34	1.2	3403	30	1.0
	60	3439	33	1.2	3404	31	1.1
	70	3440	31	1.2	3405	32	1.2
	80	3440	29	1.3	3407	33	1.4
	90	3441	28	1.3	3408	35	1.5
	100	3442	26	1.3	3410	36	1.6
	110	3442	25	1.3	3411	37	1.8
	120	3442	24	1.3	3412	38	1.8
	130	3443	23	1.2	3413	39	1.9
	140	3443	23	1.2	3414	41	1.9
M-50	30	3441	25*	0.55	3404	41	1.0
	50	3441	25*	0.64	3404	45	1.4
	60	3441	25	0.68	3404	47	1.9
	70	3441	24	0.72	3404	49	2.3
	80	3442	24	0.74	3405	52	2.9
	90	3442	24	0.76	3406	54	3.2
	100	3442	23	0.76	3408	58	4.0
	110	3442	22	0.76	3409	59	4.3
	120	3442	22	0.80	3410	60	4.6
	130	3442	22	0.82	3410	61	5.0
	140	3442	22	0.82	3412	62	5.3
M-100	30	3445	18†	0.11	3402*	105*	7.9
	50	3445	18†	0.18	3402	105	7.4
	60	3444	18†	0.16	3401	104	7.9
	70	3445	18†	0.21	3401	93	7.9
	80	3444	18†	0.24	3401	88	7.8
	90	3445	18†	0.26	3402	84	7.7
	100	3444	18†	0.28	3403	83	7.9
	110	3443	18†	0.29	3406	79	7.2
	120	3444	18†	0.35	3408	77	7.1
	130	3443	18†	0.35	3409	75	6.9
	140	3443	18†	0.35	3410	74	6.3

†Fixed at average value obtained during first pass of curve-fitting.

Table V-2
(Continued)

Sample	(°C)	"traditional" N-H H-bond			N-H H-bonded to I⁻		
		ν (cm⁻¹)	FWHM (cm⁻¹)	Area	ν (cm⁻¹)	FWHM (cm⁻¹)	Area
M-0	30	3300	131	48			
	50	3305	134	46			
	60	3308	135	45			
	70	3310	137	44			
	80	3312	138	43			
	90	3314	139	42			
	100	3317	141	41			
	110	3319	143	40			
	120	3321	144	39			
	130	3324	146	38			
	140	3326	149	37			
M-50	30	3326*	55	1.4	3272	174	76
	50	3328	65	2.4	3272	183	76
	60	3330	72	3.5	3270	187	74
	70	3333	77	4.4	3269	190	72
	80	3334	79	5.2	3268	191	70
	90	3335	79	5.2	3268	194	69
	100	3337	82	6.4	3266	193	65
	110	3338	84	6.7	3265	194	63
	120	3340	85	6.9	3265	195	61
	130	3341	89	8.0	3263	193	56
	140	3344	89	7.7	3266	191	54
M-100	30	3326*	56	1.8	3262	175	72
	50	3326	65	3.3	3255	177	73
	60	3326	73	5.7	3249	175	72
	70	3328	75	6.7	3247	176	72
	80	3330	78	8.0	3244	174	72
	90	3331	82	9.9	3241	172	71
	100	3332	84	10.7	3239	172	69
	110	3335	87	11.5	3238	172	67
	120	3336	88	11.8	3236	173	66
	130	3338	90	12.1	3237	173	63
	140	3340	91	11.2	3240	172	57

*Parameter fixed based on observed trend with temperature.

was fixed at the average value of 18 cm^{-1} obtained from the first pass. The free N-H band of sample M-50-I displayed a near-constant FWHM (22-25 cm^{-1}) over the temperature range, while the FWHM of M-0-I varied more than might be expected. Since the frequency of the free N-H vibration does not vary significantly, the area of the band is directly related to the number or concentration (but NOT fraction) of free N-H groups, under the reasonable assumption that the absorptivity coefficient is not a function of temperature over the experimental range. However, based on the uncertainties in area determination the relative error in area was estimated as on the order of 50%, and therefore any trend in number of free N-H groups with temperature can not be stated with confidence for any of the PU cationomers. On the other hand, the observed trend of decreasing concentration of free N-H groups with increasing ion content appears to be real. Since all absorbances have been normalized to the area of the C-H stretch, and the three PU cationomers have approximately the same concentration of C-H groups, a direct comparison is valid.

As the temperature is increased from 30 to 140°C, the frequency of the "traditional" hydrogen bonded band for M-100-I increases regularly from 3326 to 3340 cm^{-1}. This indicates a decrease in the average hydrogen bond strength with increasing temperature. At the same time, the FWHM increases from 56 cm^{-1} to 91 cm^{-1}. At all temperatures, fitted values of ν and FWHM for M-50-I nearly duplicate those for M-100-I. In a FTIR study of hydrogen bonding in a model PU hard segment, Coleman and co-workers[130] reported an almost identical frequency shift from 3321 to ~3342 cm^{-1} over the same temperature range. They also noted a comparable trend in the FWHM, and

interpreted it as a narrowing of the distribution of hydrogen bond strengths on crystallization; however, this explanation is not satisfactory for the amorphous PU cationomers. The frequency and FWHM of the "traditional" hydrogen bonded N-H band for the unionized polymer showed similar temperature dependencies, but the actual values differ. This dissimilarity between the unquaternized and ionized cationomers is pursued further in the Discussion section. The area of the "traditional" hydrogen bonded N-H stretching band for sample M-0-I decreases by about 25% as the temperature is increased from 30 to 140°C. It is difficult to say whether or not this corresponds to a decrease in the number of hydrogen bonded N-H groups, since the absorptivity coefficient decreases with increasing frequency as the temperature is raised. In contrast, the band area for the quaternized polymers increases roughly six-fold from 30 to 140°C. This change can be conclusively attributed to an increase in the concentration of N-H groups hydrogen bonded to traditional proton acceptors, since the absorptivity coefficient for the band is decreasing as its area increases. In fact, this means that the concentration of "traditionally" hydrogen bonded N-H groups for M-50-I and M-100-I increases by an even greater factor than the factor of six shown for the band area in Figure V-9.

At the same time, one can see that as temperature is increased the area of the band assigned to N-H groups hydrogen bonded to the anion decreases. Since the total number of N-H groups in the sample is constant with temperature, this must correspond to a decrease in the number of anion-bonded N-H groups. In other words, as the temperature is increased there is a shift in hydrogen bonding of the N-H groups from the anion to traditional proton acceptors. From Figure V-9, one also observes that the area of the

band assigned to anion-bonded N-H groups constitutes a large fraction of the total area, particularly near room temperature. Although this likely indicates that most of the N-H groups are bonded to the anion, the absorptivity coefficient of this band is greater than any other band in the N-H stretching region. As with the "traditional" hydrogen bonded N-H band of M-50-I and M-100-I, the trend in band area with temperature is in the opposite direction of the trend for the absorptivity coefficient. From 30 to 140°C, the frequency shifts smoothly from 3272 to 3266 cm^{-1} and from 3262 to 3240 cm^{-1} for samples M-50-I and M-100-I, respectively. The decrease in ν at higher ion content indicates that the average energy of the N-H to anion bond is greater for polymer M-100-I than for M-50-I. Similarly, the decrease in ν with increasing temperature for both M-50-I and M-100-I suggests an increase in the average bond strength at higher temperatures. This result is somewhat puzzling, but could be explained by assuming that weaker N-H to anion bonds are the first to be transformed to "traditional" hydrogen bonds.

B.2. C=O Stretching Region. FTIR spectra of the carbonyl stretching region, taken during heating from 30-180°C, are shown for the M-###-I cationomers in Figures V-10 to V-12. All spectra appear to be composed of two bands, although there is considerable overlap at higher temperatures. The narrower band centered at about 1736 cm^{-1} is assigned to stretching of free carbonyl groups, while the band at approximately 1712 cm^{-1} is attributed to hydrogen bonded carbonyl groups. These positions are very close to those obtained by Boyarchuk and co-workers[137] for urethane elastomers in dilute and concentrated carbon tetrachloride solutions, respectively. A number of previous investigators have assigned the carbonyl stretch at roughly 1712 cm^{-1}
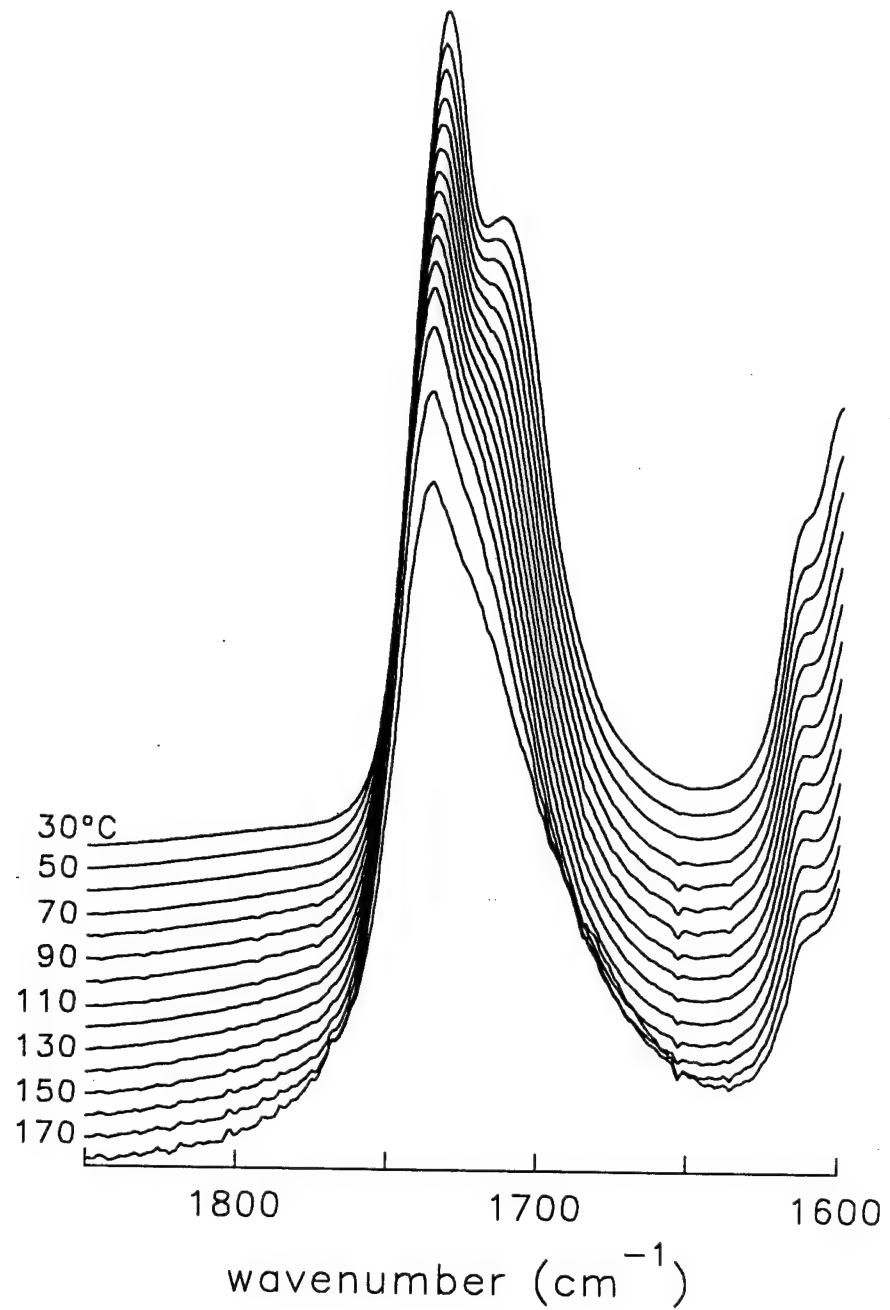
Figure V-10. FTIR spectra of M-0-I in the C=O stretching region as a function of temperature from 30 to 180°C.
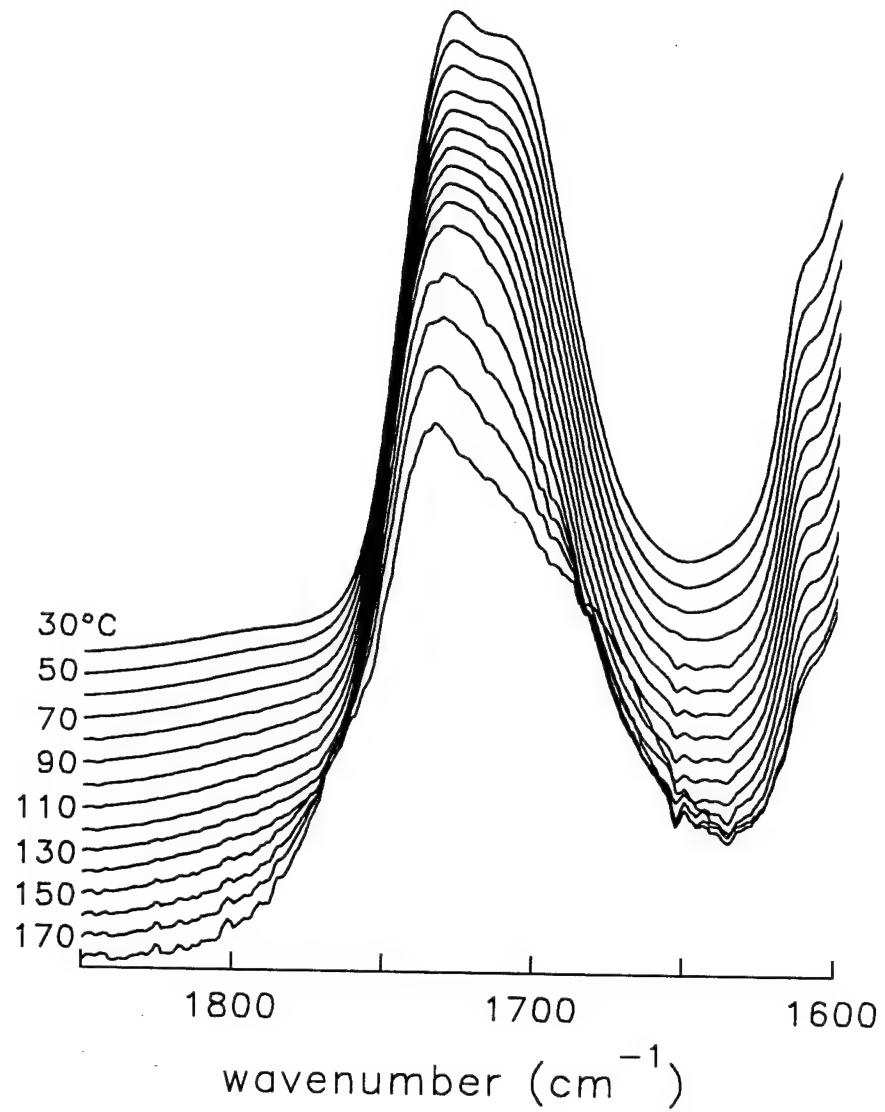
Figure V-11. FTIR spectra of M-50-I in the C=O stretching region as a function of temperature from 30 to 180°C.
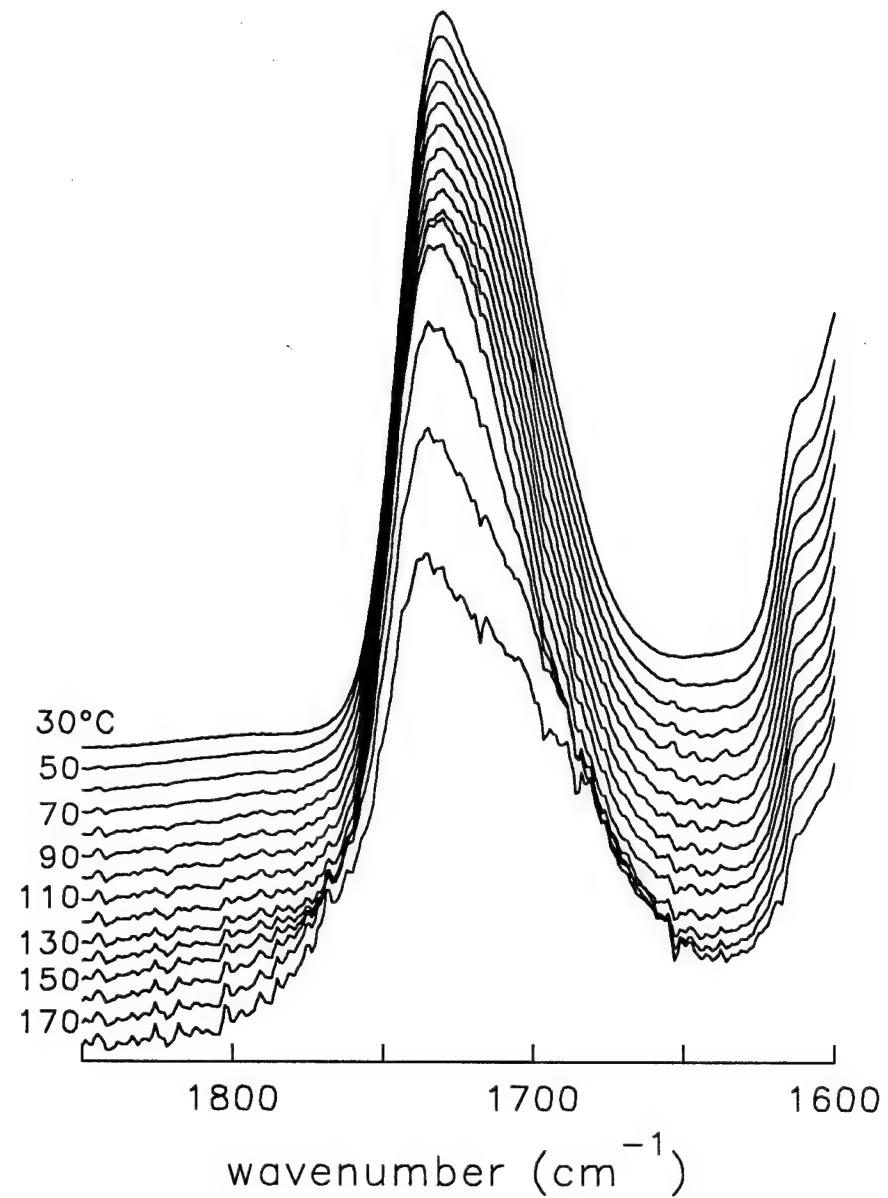
Figure V-12. FTIR spectra of M-100-I in the C=O stretching region as a function of temperature from 30 to 180°C.

to hydrogen bonding in disordered regions (i.e. urethane linkages of interfacial regions or "dissolved" in the soft phase).[113,130,138] In these same studies, a third carbonyl band at a lower frequency ranging from 1684 to 1702 cm^{-1} has been attributed to stronger hydrogen bonds in ordered or crystalline regions. Quite expectedly, the ordered hydrogen bonded carbonyl band is not observed in the amorphous materials of this study. Zharkov et al.[139] recently suggested that the amide I band of segmented polyurethanes consisted of no less than five absorption bands, free carbonyls at 1740 and 1730 cm^{-1}, and hydrogen bonded carbonyls at 1725, 1713 and 1702 cm^{-1}. Discrimination of free and hydrogen bonded carbonyls is based on the type of proton acceptor (if any) to which the neighboring urethane N-H group is associated. It is certainly possible that the two carbonyl bands assumed in this study are combinations of bands identified by Zharkov and co-workers; however, the spectra of the PU cationomers showed no obvious traits which warranted such a differentiation. Further, possible two-component bands would not appear to compromise the more simplified division of "free" and "hydrogen bonded" groups.

The carbonyl region was also deconvoluted using the commercial software program PeakFit®. Limits of the curve-fit were set at 1685 and 1775 cm^{-1} for all three polymers, with best fits obtained using a Gaussian function for the free carbonyl and a Gaussian-Lorentzian sum for the hydrogen bonded carbonyl. Following a trial iteration of curve fitting in which all parameters were allowed to float, the Gaussian component of the hydrogen bonded carbonyl was fixed at the average value of 80%. The small contribution to the fitted region of the two bands around 1600 cm^{-1} was included by

visually assigning and fixing gaussian functions. Including this minor contribution was important, but clearly erroneous values could be assumed without affecting the fitted parameters of the carbonyl region. The PeakFit® program then determined the best fit of the experimental data by varying six parameters: ν, FWHM, and area for each of the two bands. Excellent fits were obtained (Figure V-13), with coefficients of determination greater than 0.999 for all three samples at all temperatures.

Optimum parameters for curve fitting the carbonyl stretching region, again limited to a maximum of 140°C to avoid results which might be complicated by dequaternization, are given in Table V-3. Consistency of results for the three M-###-I polymers lends credibility to the spectral deconvolution. The frequency of the free carbonyl band is nearly constant, at 1737 ± 2 cm^{-1}, over the entire experimental range of temperature and ion content. Likewise, the FWHM of the free carbonyl band varies by less than 1 cm^{-1} from 30 to 140°C for each of the three samples, although the band is somewhat narrower in sample M-0-I than in either of the quaternized polymers. As would be expected, the hydrogen bonded carbonyl band is wider by some 20 to 30 cm^{-1} since it represents a distribution of bond energies in an amorphous system. Comparable temperature dependencies are observed for the FWHM in all three samples, with the band of sample M-0-I again somewhat narrower. The frequency of the hydrogen bonded carbonyl stretching is also relatively insensitive to ion content, and increases regularly by 6 to 9 cm^{-1} from room temperature to 140 °C. Like the N-H stretching region, this increase in frequency corresponds to a decrease in the average hydrogen bond strength with increasing temperature.
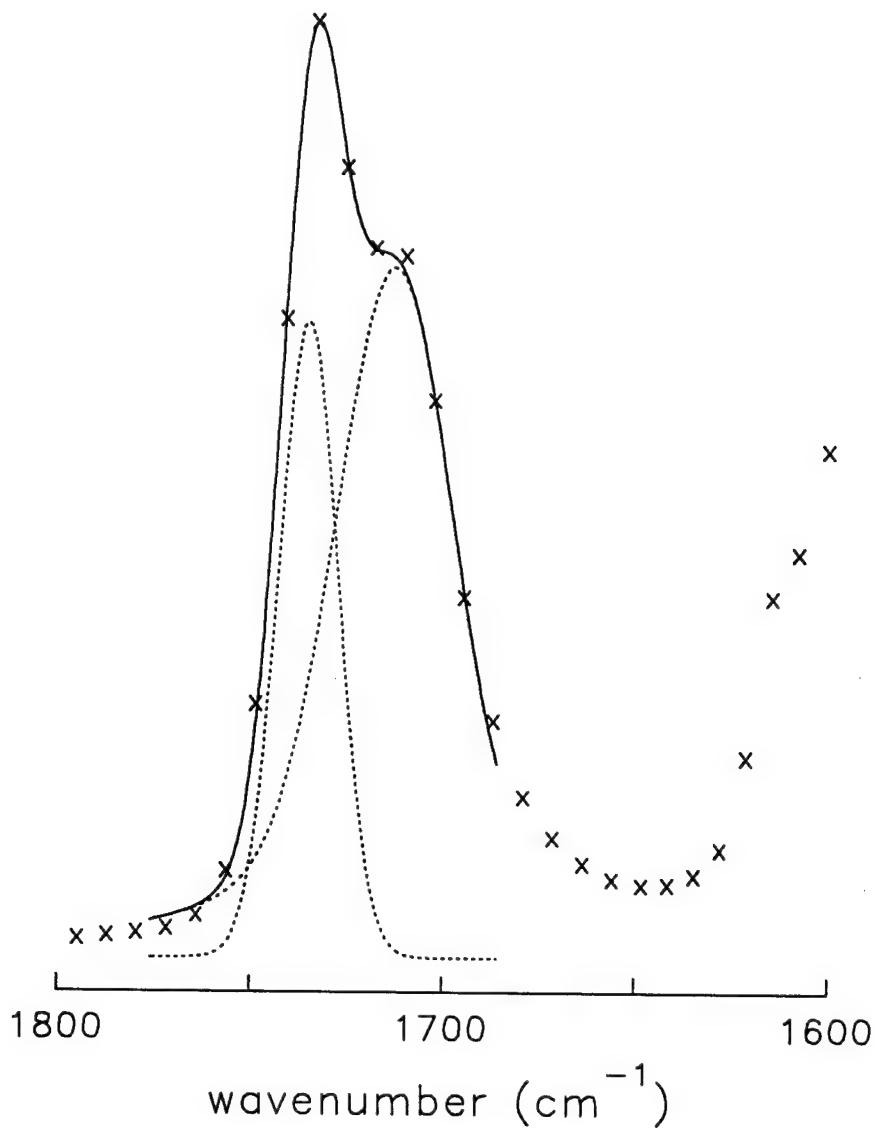
Figure V-13. Typical deconvolution of the carbonyl stretching region as described in the text. The solid line is the analytical function of the curve-fitting procedure, while the x's mark the experimental absorbance every 7 cm⁻¹.

Table V-3
Curve-Fitting Parameters for the C=O Stretching Region

Sample	(°C)	free C=O			H-bonded C=O		
		ν (cm^{-1})	FWHM (cm^{-1})	Area	ν (cm^{-1})	FWHM (cm^{-1})	Area
M-0	30	1736	19	18.0	1712	36	45
	50	1736	19	15.9	1714	38	49
	60	1736	19	15.3	1714	40	50
	70	1736	19	14.5	1715	41	51
	80	1737	19	13.7	1716	43	52
	90	1737	19	13.0	1717	44	52
	100	1737	19	12.7	1718	45	53
	110	1738	19	12.4	1719	46	54
	120	1738	19	12.2	1720	47	55
	130	1739	19	12.0	1720	47	56
	140	1739	19	11.7	1721	48	56
M-50	30	1737	25	14.4	1709	45	42
	50	1737	25	12.8	1710	48	44
	60	1738	25	12.2	1711	49	45
	70	1738	25	12.0	1711	50	46
	80	1738	25	11.3	1712	51	48
	90	1738	24	10.2	1713	52	51
	100	1738	24	10.1	1713	53	51
	110	1739	24	9.8	1714	54	52
	120	1739	24	9.1	1714	55	53
	130	1739	24	8.4	1715	56	54
	140	1739	24	7.7	1716	57	55
M-100	30	1735	25	19.8	1711	44	45
	50	1735	25	18.5	1712	45	46
	60	1735	25	18.2	1712	46	47
	70	1736	25	17.9	1713	46	48
	80	1736	25	17.2	1713	47	49
	90	1736	25	16.9	1714	47	50
	100	1736	25	16.4	1714	48	50
	110	1736	25	16.0	1714	48	51
	120	1737	25	15.7	1715	50	52
	130	1737	25	14.9	1716	50	53
	140	1737	24	13.4	1717	51	56

In all three polymers the area of the free carbonyl band (A_F) shown in Figure V-14 decreases almost linearly with increasing temperature. A parallel increase in area with temperature is observed for the hydrogen bonded band (A_B). As compared to the N-H stretching region, the frequencies of the vibrations in the carbonyl stretching region do not shift as much with temperature, and the absorptivity coefficient is not as strong a function of ν. The band area changes of the carbonyl region are therefore directly related to an increase in the fraction of hydrogen bonded carbonyls with increasing temperature. This trend in the number of hydrogen bonded groups with temperature is counter-intuitive, and in the opposite direction of all (to the best of the author's knowledge) previously reported infrared temperature studies on PUs with either amorphous[128], mesogenic[113], or semicrystalline[109,121,125,129,130] hard segments. In Figure V-14, one can also see that the total area of the carbonyl region (A_T) increases with increasing temperature. Since the total concentration of carbonyl groups is constant for each sample, the changes in total area are caused by a greater absorptivity coefficient for the hydrogen bonded carbonyl (α_B) than for free carbonyls (α_F). Although this difference in α complicates calculation of the distribution of free and hydrogen bonded carbonyl groups, the fractions can be approximated by the following analysis. The total area as a function of temperature T is given by:

$$A_T(T) = A_B(T) + A_F(T) \qquad (V-1)$$

Substituting the Beer-Lambert law, $A_i = \alpha_i C_i L$, for the integrated absorbance of each
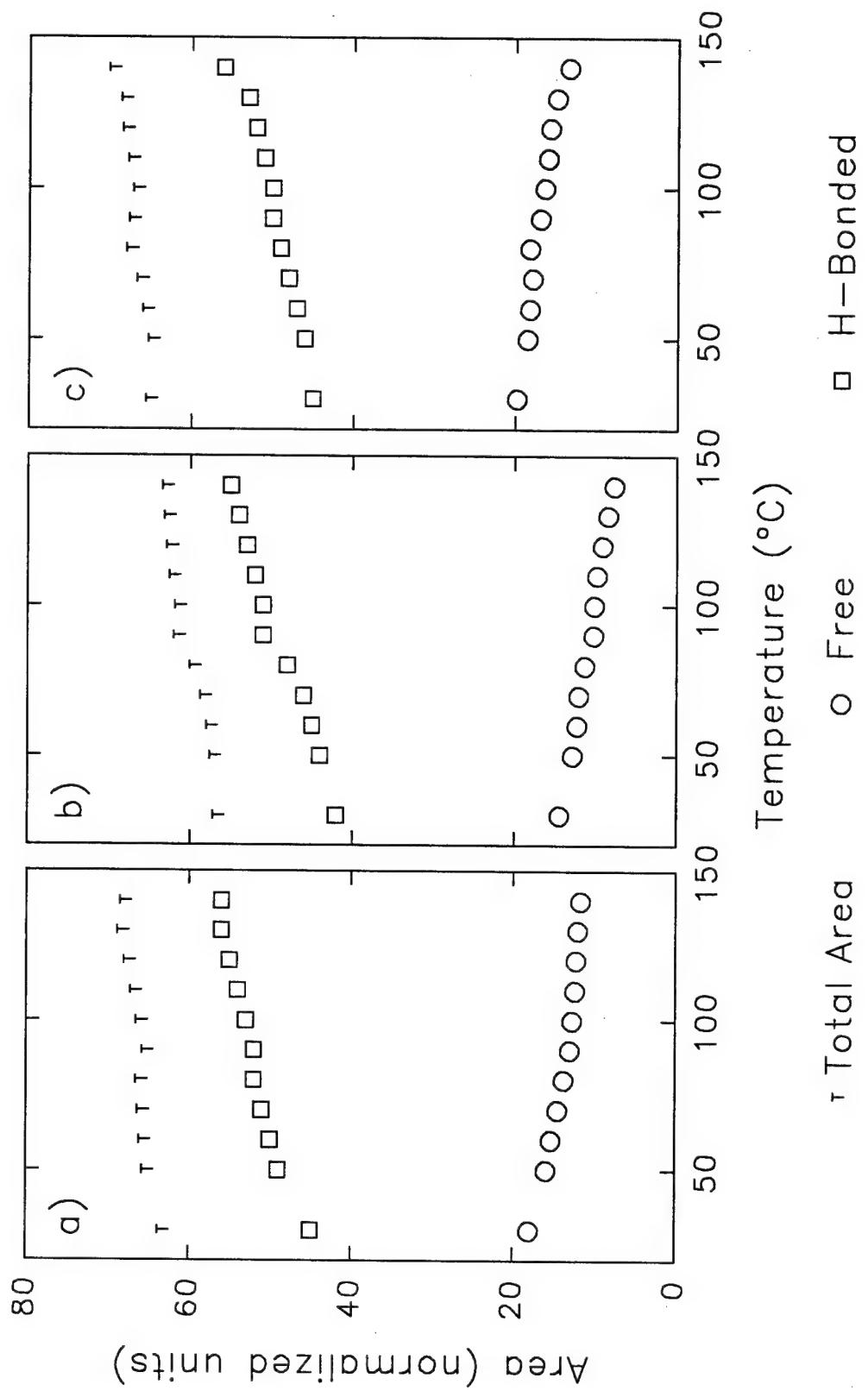
Figure V-14. Normalized areas of bands assigned to free and hydrogen bonded carbonyl groups as a function of temperature from 30 to 140°C for a) M-0-I, b) M-50-I, and c) M-100-I.

band as a function of the total concentration of functional groups C and path length L,

$$A_T(T) = CL [\alpha_B(T) X_B(T) + \alpha_F(T) (1 - X_B(T))] \qquad (V-2)$$

where $X_B(T)$ is the fraction of hydrogen bonded carbonyls. Since the results have already been normalized such that the CL product is a constant, $A_T(T)$ is constant only if $\alpha_B(T) = \alpha_F(T)$. In the present case $A_T(T)$ is not constant. However, we can define $r(T) = \alpha_B(T)/\alpha_F(T)$, $A_F^*(T) = r(T)A_F(T)$ and $A_T^*(T) = A_B(T) + A_F^*(T)$ such that:

$$A_T^*(T) = A_B(T) + r(T) A_F(T) = CL\alpha_B(T) \qquad (V-3)$$

If we then assume that α_B and α_F are constant with temperature, Equation V-3 shows that A_T^* will also be a constant, with the fractions of free and hydrogen bonded groups given by $X_F(T) = A_F^*(T)/A_T^*$ and $X_B(T) = A_B(T)/A_T^*$.

As indicated by Equation V-3, the ratio of the absorptivity coefficients r for each polymer can be obtained via a linear least-squares fit of $A_B(T)$ versus $A_F(T)$. Results of the analysis are displayed in Figure V-15, with the adjusted areas A_F^* and A_T^* determined from the average value of r=1.88 $\pm$ 0.29 for the three polymers. All values of A_T^* are within 2% of the average for each sample indicated by a short-dashed line. The occurrence of a near-constant adjusted total area, using a single value of r=1.88 for three polymers which contain widely differing ion contents, bestows some credibility to the technique. Further, the average ratio of absorptivity coefficients is in reasonable agreement with the value r=1.71 estimated by Coleman and co-workers[130] for a semicrystalline polyurethane homopolymer. The results of Figure V-15 suggest that at room temperature the fraction of free carbonyls is 0.43 for M-0-I, 0.39 for M-50-I, and
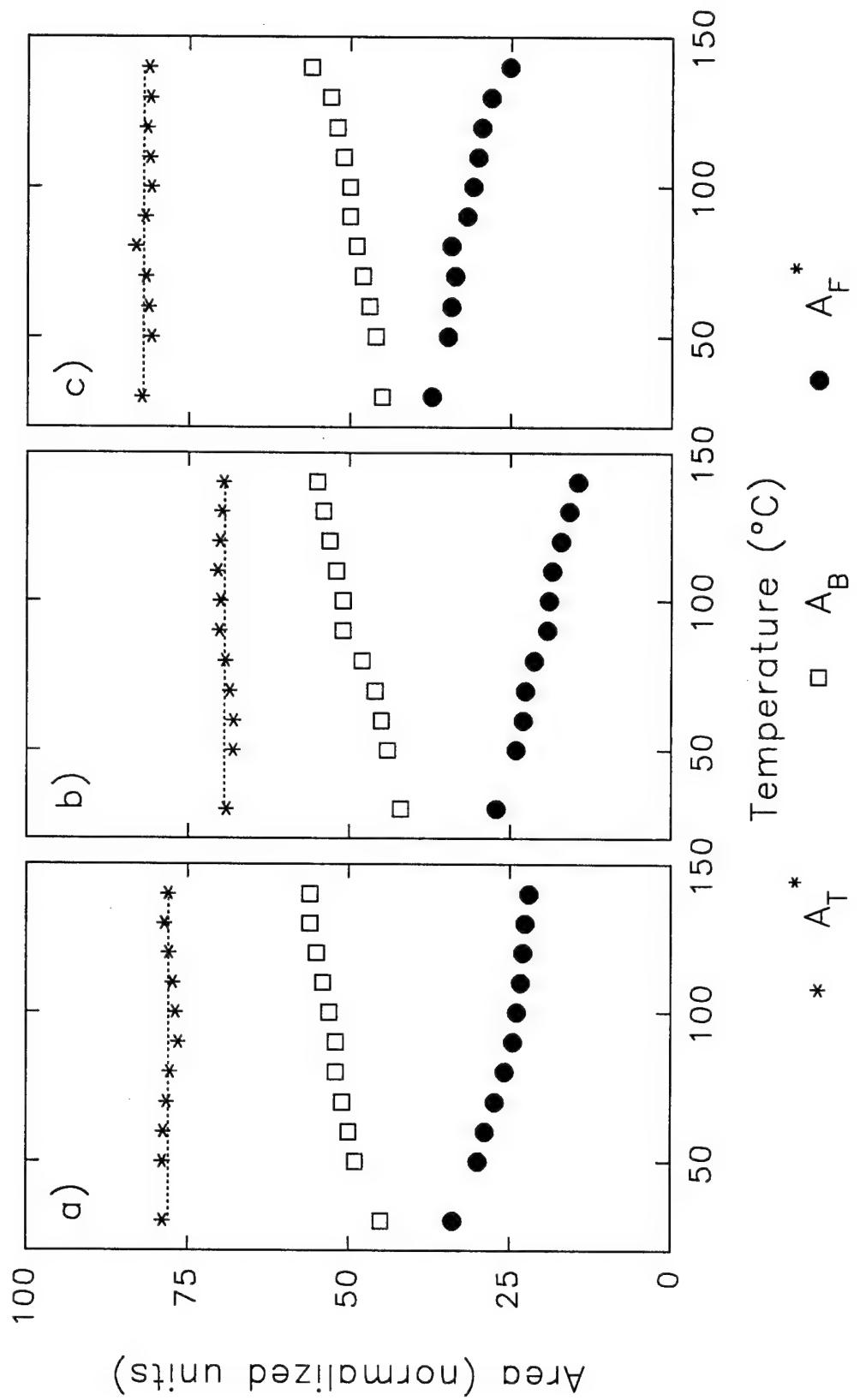
Figure V-15. Adjustment of areas in Figure V-14 for the inequality of the absorptivity coefficients of the free and hydrogen bonded carbonyl bands.

0.45 for M-100-I. A steady decrease in X_F is evident for all three polymers with increasing temperature, with the fraction of free carbonyls at 140°C approximately 0.28 for M-0-I, 0.21 for M-50-I, and 0.31 for M-100-I. Although comparable trends in the distribution of free and hydrogen bonded carbonyl groups with temperature are observed for all three polyurethanes, and indeed the actual fractions at all temperatures are strikingly similar, very different mechanisms are involved for the two quaternized polymers versus sample M-0-I.

C. Discussion

Results of the FTIR temperature experiments are discussed for each of the three PUs in terms of its chemical structure, morphology, and thermomechanical properties. For polymers M-0-I and M-100-I, a rough approximation of the distribution of various hydrogen bonds is sought using mass balances and the calculated fractions of free and hydrogen bonded carbonyl groups. Since the total number of N-H and C=O groups are equal, the following equality can be written:

$$C{=}O_{Free} + C{=}O_{N-H} = N{-}H_{Free} + N{-}H_{C=O} + N{-}H_{Ether} + N{-}H_{I^-} + N{-}H_{Others}$$

$$(V\text{-}4)$$

Known contributions to $N{-}H_{Others}$ include hydrogen bonding to urethane alkoxy oxygens and π orbitals of aromatic rings. Direct calculation of this contribution would of course be beneficial, but is unrealistic in the present investigation due to the complexity of the system. Some previous studies allow estimation of the relative importance of this term.

In a semicrystalline PU homopolymer (hard segment analog), Sung and Schneider[119] estimated that 10-25% of N-H groups were bonded to functional groups other than the carbonyl. With no soft segment in the material, the "other" is presumably alkoxy oxygens and π orbitals. However, in a later study on multiblock urethane copolymers,[128] their results indicate that only 10-15% of N-H groups are not bonded to carbonyls. They also state that this is an overestimate, since the fractions of hydrogen bonded and free carbonyls were determined from peak heights, and the band width of the former is greater than the latter. In this segmented PU, a number of the N-H groups are also likely bonded to oxygens of the 1000 molecular weight poly(tetramethylene oxide) soft segment, since some degree of phase mixing is certain with this oligomer. Coleman and co-workers[130] studied a different semicrystalline hard segment analog, and estimated that 11% of carbonyls were free at room temperature. This would be the maximum value of N-H_{Others} assuming no free N-H groups. Finally, Wang *et al.* recently suggested that the band at approximately 3400 cm^{-1} (which is attributed to a two-phonon vibration in this study) is in fact the stretching vibration of N-H groups hydrogen bonded to aromatic π orbitals.[140] They calculated that 3% of the N-H groups were bonded to π orbitals in an amorphous one-phase PU. From the results of these studies, the value of N-H_{Others} appears to be on the order of 10% for a wide variety of polyurethanes of varying chemistry and morphology.

C.1. Polymer M-0-I. At room temperature, approximately 57% of the urethane carbonyls in sample M-0-I were hydrogen bonded. Since N-H_{f^-} is zero for the unquaternized polymer, Equation V-4 indicates that 43% of N-H groups are either free

or bonded to ethers and "others". Although the fraction of free N-H groups can not be calculated with confidence, previous estimates[109,129,130,141] for α_B/α_F between 3.1 to 5.6 suggest a number far less than 43%. This implies that a substantial fraction of N-H groups in M-0-I are hydrogen bonded to ethers of the PTMO soft segment. Such a result is not surprising since results of Chapter III showed that this polymer is primarily a mixed hard-segment/soft-segment one-phase material. According to the stoichiometry shown in Figure II-1, there are roughly two times as many ether groups available as carbonyl groups if the polymer lacks phase separation. Further evidence for hydrogen bonding to ethers is obtained from the frequency of the N-H stretching vibration assigned to "traditional" hydrogen bonding. In sample M-0-I, ν is 3300 cm^{-1} at room temperature, as compared to 3326 cm^{-1} in both M-50-I and M-100-I. Using infrared spectra of segmented polyurethanes with monodisperse hard segments of varying length, Christenson and co-workers[112] assigned N-H stretches at 3321-3328 cm^{-1} and 3258-3265 cm^{-1} to N-H groups hydrogen bonded to urethane carbonyls and polyol ethers, respectively. They found that the band at ~3260 cm^{-1} increased in area with decreasing hard segment length, and was especially prominent in systems which lacked phase segregation. Also, the band was not observed in infrared spectra of the hard segment analogs. Through FTIR temperature studies, Lee et al.[122] also associated a band at 3295 cm^{-1} with N-H groups bonded to ethers in phase-separated polyurethanes. For sample M-0-I, we might therefore expect that the "traditional" hydrogen bonded band at 3300 cm^{-1} is a superposition of broad distributions attributable to N-H groups hydrogen bonded to ethers and

carbonyls. Evidence of a slight splitting of the two bands may in fact be present in the spectra of Figure V-7a obtained during cooling the unquaternized polyurethane from 140°C.

As the unquaternized polymer is heated from 30 to 140°C, the fraction of hydrogen bonded carbonyls increased from an estimated 0.57 to 0.72. To reiterate, this trend is in the opposite direction of that usually observed. If the only interactions present were N-H and carbonyl groups, the fraction of free N-H groups would have to decrease by 0.15 over the same temperature range. Although a trend in the number of free N-H groups with temperature cannot be stated with confidence, a decrease of 0.15 in the fraction of free N-H groups would certainly be evident and outside the range of experimental error, since probably no more than 15% of the N-H groups are free at 30°C. Further, a transformation of free to hydrogen bonded N-H groups with increasing temperature is inconsistent with equilibrium considerations. This discrepancy can be explained by again considering the bonding of N-H groups to ethers of the soft segment. As temperature is increased, the fraction of N-H groups hydrogen bonded to ether oxygens decreases, while the fraction hydrogen bonded to carbonyl groups increases. If the band assignments of Christenson and co-workers discussed in the preceding paragraph are correct, then an increase in ν with increasing temperature would be expected for the hypothesized redistribution of N-H hydrogen bonds. This is precisely what is observed for the "traditional" hydrogen bonded N-H stretching vibration of sample M-0-I. Finally, the proposed shift in N-H bonding from ether oxygens to urethane carbonyls is consistent with equilibrium considerations as outlined below. A simplified picture of the competing

equilibria can be represented by the hypothetical reaction

$$C{=}O \;+\; N{-}H_{\text{IIII}}OR_2 \;\rightleftharpoons\; N{-}H_{\text{IIII}}O{=}C \;+\; OR_2 \qquad\qquad (A)$$
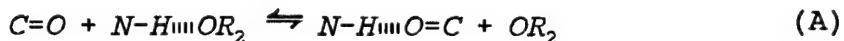
Reaction A can be considered a sum of the primary Reactions B and C

$$N{-}H_{\text{IIII}}OR_2 \;\rightleftharpoons\; N{-}H \;+\; OR_2 \qquad\qquad (B)$$

$$N{-}H \;+\; C{=}O \;\rightleftharpoons\; N{-}H_{\text{IIII}}O{=}C \qquad\qquad (C)$$
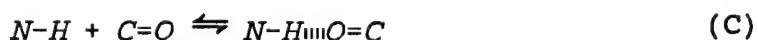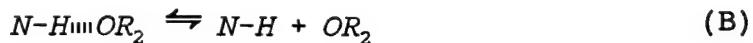
The greater frequency shift for N-H groups hydrogen bonded to ether oxygens, as compared to that for carbonyls, is evidence that the enthalpy of Reaction B is greater than the enthalpy of Reaction C. Hence, Reaction A is endothermic and the equilibrium position shifts to the right as temperature is increased.

C.2. Polymer M-100-I. Approximately 55% of the carbonyl groups in the fully ionized polymer are hydrogen bonded at room temperature. Although the fraction of free N-H groups can not be determined with any relative confidence, N-H$_{\text{Free}}$ appears negligible from the following crude analysis. The area of the free N-H stretching band is 0.13% of the total area of the N-H region. From the total areas of Figure V-9, the average absorptivity coefficient for the N-H stretching region, α_{ave}, of M-100-I is around 1.6 times greater than for M-0-I at 30°C. Using a conservative value of $\alpha_B/\alpha_F{=}6.2$ for the "traditional" hydrogen bond, then $\alpha_{\text{ave}}/\alpha_F$ is about 10 for M-100-I, and just over one percent of the N-H groups are free. Even if the area of the free N-H band (or the estimate of the ratio of absorptivity coefficients) is off by a factor of 2 or 3, N-H$_{\text{Free}}$ is only a few percent. N-H$_{\text{Ether}}$ is also assumed comparatively small, since results of

Chapter III indicate little phase mixing in the fully quaternized PU. If from these arguments, an estimate of 15% is made for the sum of N-H$_{Free}$ + N-H$_{Ether}$ + N-H$_{Others}$ in Equation V-4, then roughly 30% percent of the N-H groups are hydrogen bonded to the anions. As shown in the chemical structure of Figure II-1, the ratio of N-H groups to iodine atoms is 3:1, which suggests approximately one N-H group is hydrogen bonded to each anion. With no crystalline order in the hard domains, a loose arrangement of the hard segments with a number of possible interactions might be expected, as schematically depicted in Figure V-16. Such an arrangement, with a large number of relatively strong N-H to anion interchain associations, can satisfactorily explain the tremendous increase in tensile properties of the PU cationomers on ionization. In Chapter III, sample M-100-I exhibited a Young's modulus of 430 MPa as compared to 9.1 MPa for M-0-I, and 85 MPa for a conventional PU with semicrystalline hard segments and the same fraction of PTMO. An arrangement like Figure V-16 is also consistent with the earlier observation that no small-angle X-ray scattering peak exists that is attributable to ionic aggregation within the hard domains. If most or all of the iodine atoms are "coupled" to N-H groups, steric restrictions would reduce the likelihood of the ammonium groups aggregating.

When the temperature of M-100-I is increased from 30 to 140°C, the fraction of hydrogen bonded carbonyls increases from approximately 0.55 to 0.69. In the N-H stretching region, a parallel increase in the fraction of N-H groups hydrogen bonded to carbonyls is observed, while the concentration of N-H groups hydrogen bonded to iodine atoms decreases. Although we can not quantify the trends in the N-H region, the results
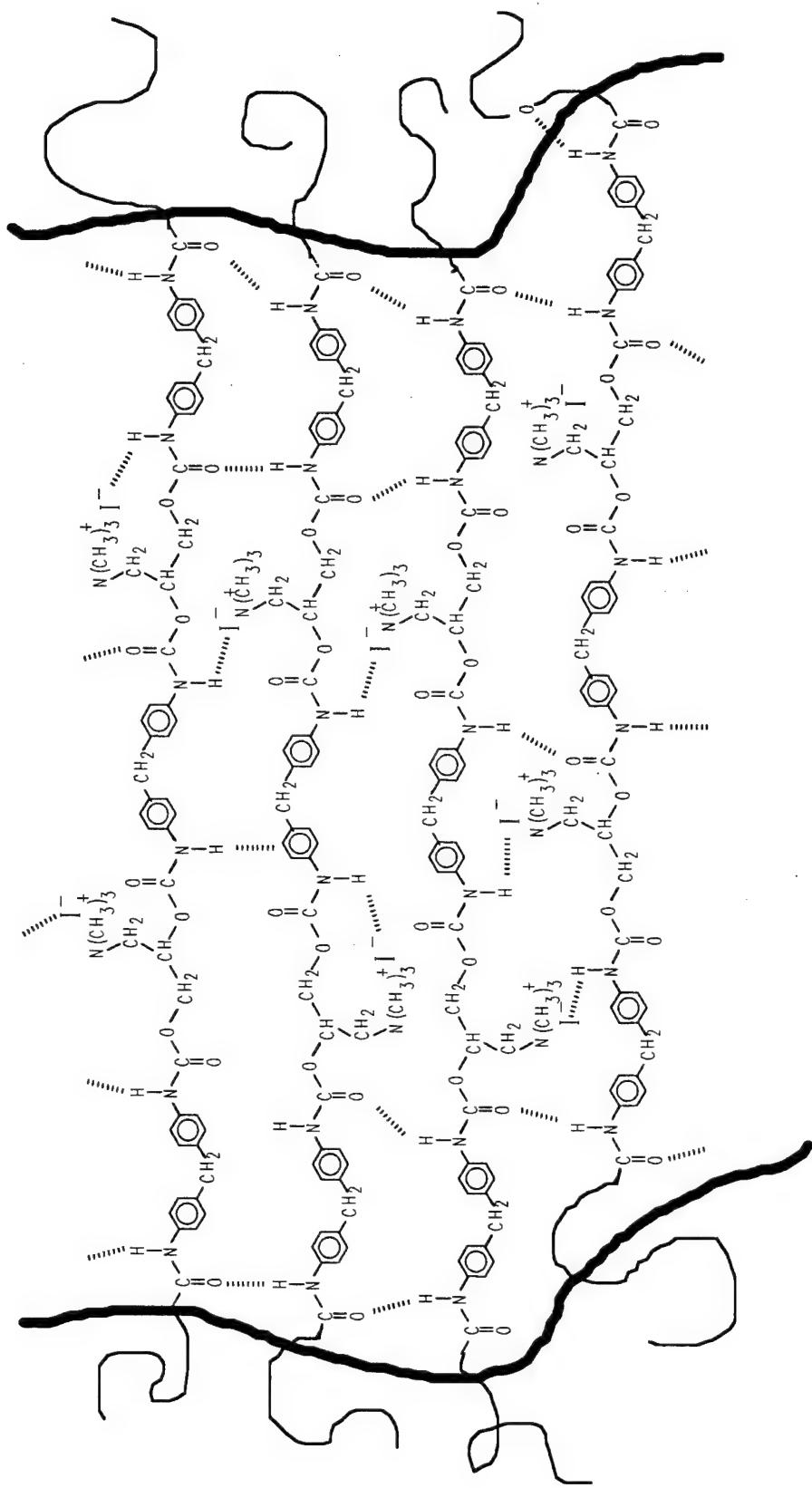
Figure V-16. Schematic of hydrogen bonding, and plausible packing arrangement, in polyurethane cationomer hard domains.

conclusively indicate a shift in the distribution of N-H hydrogen bonding from the anions to carbonyls with increasing temperature. The results of Figure V-7c show that the process is reversible to at least 140°C, just above the upper transition in the DMTA scan of Figure V-17. An analogous explanation to Reactions A-C can be given for the shift in N-H bonding at elevated temperatures, since the frequency of the anion-bonded N-H stretching vibration is also lower than for N-H groups hydrogen bonded to carbonyls.

C.3.   Polymer M-50-I.   Results from Chapter III suggested a two-phase morphology, with considerable phase mixing, for the 50% quaternized polymer. This prohibits even a crude mass balance like that employed for M-0-I or M-100-I, since Equation V-4 contains too many unknown terms. In spite of this limitation, some important observations can still be made. First, sample M-50-I again shows an increase in the number of hydrogen bonded carbonyls on heating. Fractions of 0.61 at room temperature and 0.79 at 140°C are somewhat higher than for the fully ionized cationomer, an outcome that might be expected since fewer anions are available for bonding to N-H groups in the lower ion content PU. Secondly, a shift in N-H bonding from the iodine atoms to the carbonyl groups again appears to be the most prominent change on heating, confirming the results of sample M-100-I. Finally, since the changes are reversible to at least 140°C, and the upper DMTA transition of M-50-I is well below this temperature, these results conclusively indicate that the flow transition for the PU cationomers is also reversible and therefore not caused by dequaternization. In fact, the evidence suggests that the interchain N-H to anion bonds are the primary interaction which "holds the polymer together," so the flow transition is likely a direct consequence of the observed
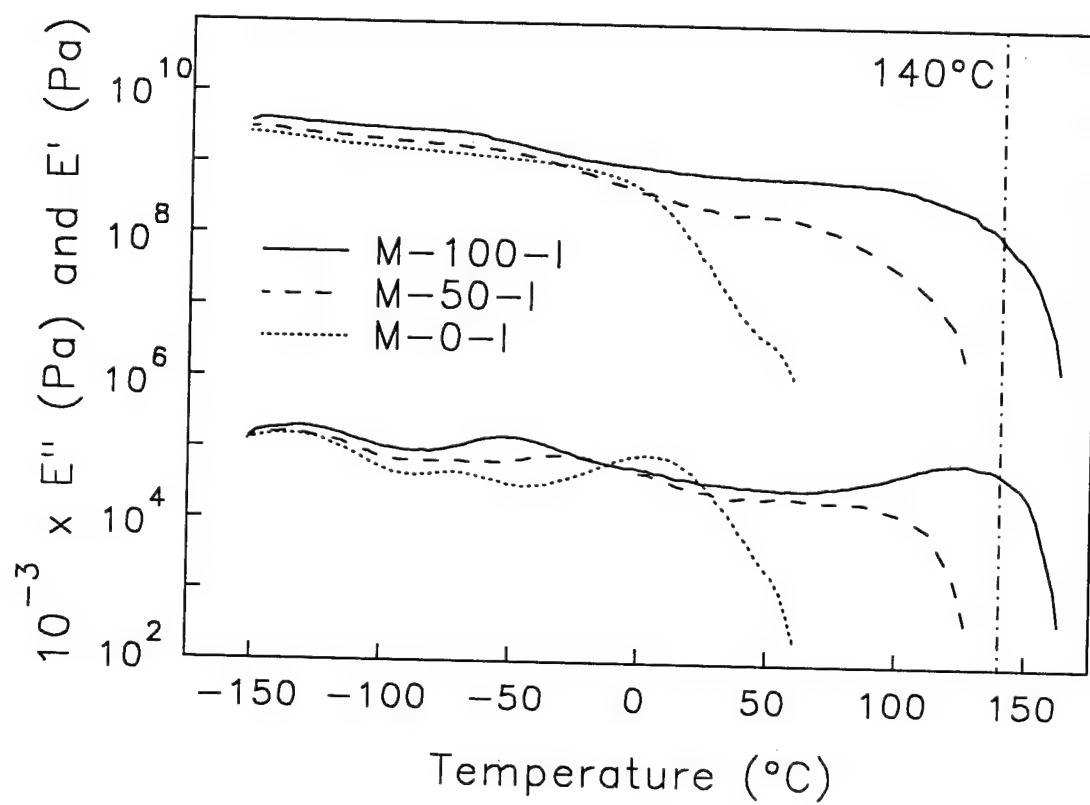
Figure V-17. E' and E" for the M-###-I polymers. Data were replotted from Figures III-1 to III-3. The vertical dot-dash line at 140°C demarcates the approximate maximum temperature at which the infrared spectra are reversible.

change in N-H bonding at elevated temperatures. This statement could not be made from the results for M-100-I, where flow and dequaternization (although slight) occur simultaneously.

D. Summary

The carbonyl stretching region of the infrared spectra of all three PUs display two bands, attributed to hydrogen bonded and free carbonyl groups. For sample M-0-I, the N-H stretching region contains bands assigned to free and "traditional" hydrogen bonded N-H groups. The unquaternized sample is one-phase, and thus the "traditional" hydrogen bonded band likely contains contributions from N-H stretching vibrations where urethane carbonyls and soft-segment ethers are the proton acceptors. In the N-H region of the infrared spectra of the quaternized polyurethanes M-50-I and M-100-I, most of the "traditional" proton acceptors are urethane carbonyls, since these materials are microphase separated. An additional N-H stretching band, assigned to N-H groups hydrogen bonded to the anions, is also observed. The N-H to anion bond is stronger than the "traditional" hydrogen bond, and these interchain ties are apparently the specific interaction responsible for the microphase separation and excellent mechanical properties of the PU cationomers. A semiquantitative N-H group balance for the fully ionized cationomer suggests that roughly one N-H group is bonded to each anion; aggregation of ionic groups within the hard domains is therefore unlikely, though not precluded.

In all three polymers, the fraction of free carbonyl groups decreases with increasing temperature. This trend is in the opposite direction of conventional PUs with

semicrystalline hard segments. A redistribution of N-H hydrogen bonding on heating, from the ether groups to urethane carbonyls, is proposed to explain this result for the unquaternized PU. In M-50-I and M-100-I, a similar change occurs with hydrogen bonding of N-H groups shifting from the anion to carbonyl groups with increasing temperature. Both events are fully reversible to a maximum temperature of approximately 140°C, beyond which dequaternization of the ammonium groups becomes significant. Although there were no obvious transitions in the infrared temperature spectra which directly correlate with the upper transition in dynamic mechanical thermal analysis, results strongly suggest that the flow transition in the PU cationomers is associated with this steady shift in N-H bonding from the anion to carbonyl groups.

Chapter VI. Investigation of the Microphase Separation Transition

A. Introduction

In the preceding Chapter, results of FTIR temperature studies suggested that the specific interaction responsible for the substantial increase in mechanical properties of the PU cationomers is hydrogen bonding of urethane N-H groups to the neutralizing anion of the trialkylammonium group. Further, the viscous flow transition in dynamic mechanical thermal analysis appears related to the observed shift in N-H bonding from the anion to urethane carbonyls at elevated temperatures. Also, results presented in Chapter III showed that the unquaternized precursor polymer is essentially a one-phase material. This raises the obvious question: If hydrogen bonding between N-H groups and anions is the primary driving force for microphase separation in these polymers, and the number of N-H to anion bonds diminishes at elevated temperatures, then do the PU cationomers pass through a microphase separation transition (MST) at temperatures near the onset of viscous flow?

The MST or order-disorder transition has been extensively studied in diblock and triblock copolymers. Various experimental techniques such as small-angle X-ray scattering (SAXS),[142-150] differential scanning calorimetry (DSC),[151,152] and melt rheology[153-160] have been used to distinguish between homogeneous and heterogeneous morphologies. In spite of their commercial importance, far fewer investigations of the MST have been reported for segmented PU elastomers. Using a combination of SAXS and DSC, Koberstein and co-workers[18,19] concluded that the onset of microphase mixing in polyurethanes with hard segments of MDI and butanediol (BD) was at temperatures

below the melting point of the microcrystalline hard domains (T_m). Isothermal crystallization below the apparent MST temperature (T_{MST}) occurred within the confines of existing hard domains, since microphase separation preceded crystallization. At temperatures between T_{MST} and T_m, hard segment crystallization took place from a homogeneous melt.[18] Koberstein and Galambos also investigated the origin of multiple melting endotherms in this material.[22] Simultaneous SAXS-DSC experiments, and wide-angle X-ray diffraction profiles at various temperatures, suggested that the endotherms were associated with distinct crystal populations of different melting points. Since the melting occurred at temperatures above T_{MST}, melted hard segment material at each endotherm spontaneously mixed with the soft microphase. The onset of microphase mixing was indicated in SAXS results by a drastic decrease in the invariant over a temperature range of 30-40°C, and a coincident sharp increase in the long period, with complete disappearance of the interference peak above T_m.[18,22] Almost identical observations were reported by Chu and co-workers in SAXS temperature studies of a similar polyurethane with MDI/BD hard-segments.[161] In a separate study, they also used SAXS to measure the kinetics of structure development in segmented PUs quenched from the homogeneous melt to temperatures below T_{MST}.[162] Ryan *et al.* examined the order-disorder transition in a multiblock polyurethane with amorphous hard domains.[163] Like the polyurethanes with semicrystalline hard segments, SAXS profiles of the amorphous PU showed a sharp decrease in the invariant as the temperature increased through the MST, with a corresponding abrupt change in the Bragg spacing. Also, rheological experiments showed that the low-frequency shear storage modulus decreased by roughly

1 order of magnitude as the temperature was increased through the MST, with less temperature dependence above and below the transition.

In this Chapter, the prospect of a MST in the polyurethane cationomers was investigated using SAXS and rheological techniques. Since the experimental temperature range was limited by dequaternization, MST studies of a segmented PU with semicrystalline hard domains and a binary mixture of diblock copolymers were used for comparison.

B. Results and Discussion

B.1. Dequaternization studies. Thermal studies of any polymer system can be jeopardized by decomposition, and the ammonium groups of cationomers which are labile at high temperatures are of concern here. The extent of dequaternization is clearly a function of both time and temperature. However, as opposed to performing a full kinetic study, only the upper temperature at which dequaternization would not significantly affect results was determined. Using a rotating anode X-ray source for SAXS experiments, data collection times of 2 to 4 hours were anticipated at each temperature. The percent dequaternization that might occur during SAXS measurements was estimated by heating thin polymer films (0.2 mm) in a nitrogen atmosphere for 3 hours. Results of the test for the cationomer M-100-I are given in Table VI-1, where the percent dequaternization was defined according to weight loss and the elemental iodine content (Galbraith Laboratories). For calculations based on the percentage weight loss, a Hoffmann-type elimination was assumed in which hydroiodic acid and trimethylamine are the elimination

Table VI-1
Extent of Dequaternization as Measured by Weight Loss and Iodine Content

Temperature[a] (°C)	%I⁻	Percent Weight Loss	Percent Dequaternization	
			I⁻ Basis	Weight Basis[b]
Initial	11.87	---	---	---
110	11.50	0.8	3	5
145	10.77	3.8	9	25
180	4.53	15.9	60	110

[a] 3 hours in dry nitrogen.
[b] Assumes Hoffman-type elimination.

products. Charlier *et al.* found that this mechanism was the most likely mode of end group degradation in telechelic polystyrenes with quaternary ammonium end groups.[164] Two points can be readily inferred from the results of Table VI-1. First and most importantly, the upper temperature limit for SAXS experiments will be somewhere in the range of 110 to 140°C. In determining this limit, the assumption was made that a few percent dequaternization will not significantly alter the cationomer morphology. Secondly, an additional mechanism(s) of degradation is evident since levels of dequaternization calculated from weight loss were always greater than levels determined from iodine content, and the Hoffmann-type elimination has the maximum theoretical weight loss of dequaternization. Results suggest the second type of degradation occurs at temperatures as low as 110°C. Some mode of degradation catalyzed by the hydroiodic acid eliminated during dequaternization is likely, since PUs typically show much better thermal stability.

Although a few percent dequaternization is tolerable in SAXS studies, this is not true for rheological experiments where subtle transitions in viscoelastic properties were investigated. To define experimental conditions where essentially no dequaternization occurs, the weight loss and elemental analysis methods of quantifying dequaternization are not accurate enough. However, experiments in Chapter V suggested that the N-H stretching region of infrared spectra was very sensitive to even small levels of dequaternization. The following procedure was developed to determine the upper temperature limit for rheological experiments. The cationomers M-100-I and M-50-I were heated in a nitrogen atmosphere from room temperature to some elevated

temperature in 2 to 3 minutes, held at temperature for 20 minutes, then cooled back to room temperature in 5 to 7 minutes. FTIR spectra were recorded before and after heating, and compared to determine if the process was reversible. In addition to looking for qualitative differences in the spectra, before and after spectra were compared mathematically. Assuming that the after spectrum can be "mapped" onto the before spectrum with an offset constant B and multiplication factor M according to Equation VI-1,

$$A_{After}(\nu) \ = \ M \times A_{Before}(\nu) + B \qquad\qquad (VI-1)$$

then the linear least-squares fit of the absorbances A over all wavelengths ν yields a correlation coefficient ϵ that quantifies the similarity in shape of the spectra before and after heating. The constant B eliminates the effect of slight differences in baseline subtraction, while M adjusts for small errors in normalization for sample thickness.

Correlation coefficients for both cationomers at temperatures from 130 to 180°C are given in Table VI-2, with the before and after spectra of the N-H stretching region displayed in Figure VI-1 for M-100-I and Figure VI-2 for M-50-I. At least 12 samples of each cationomer were correlated to each other prior to heating. Sample to sample comparisons of M-100-I all gave values of ϵ greater than 0.990, and greater than 0.995 for M-50-I. These values were used as the criteria to determine if before and after spectra at a given temperature were "identical." Heating for 20 minutes at 170°C and higher clearly resulted in irreversible changes to the N-H stretching region of both cationomers. At temperatures at or below 140°C, the process for both cationomers
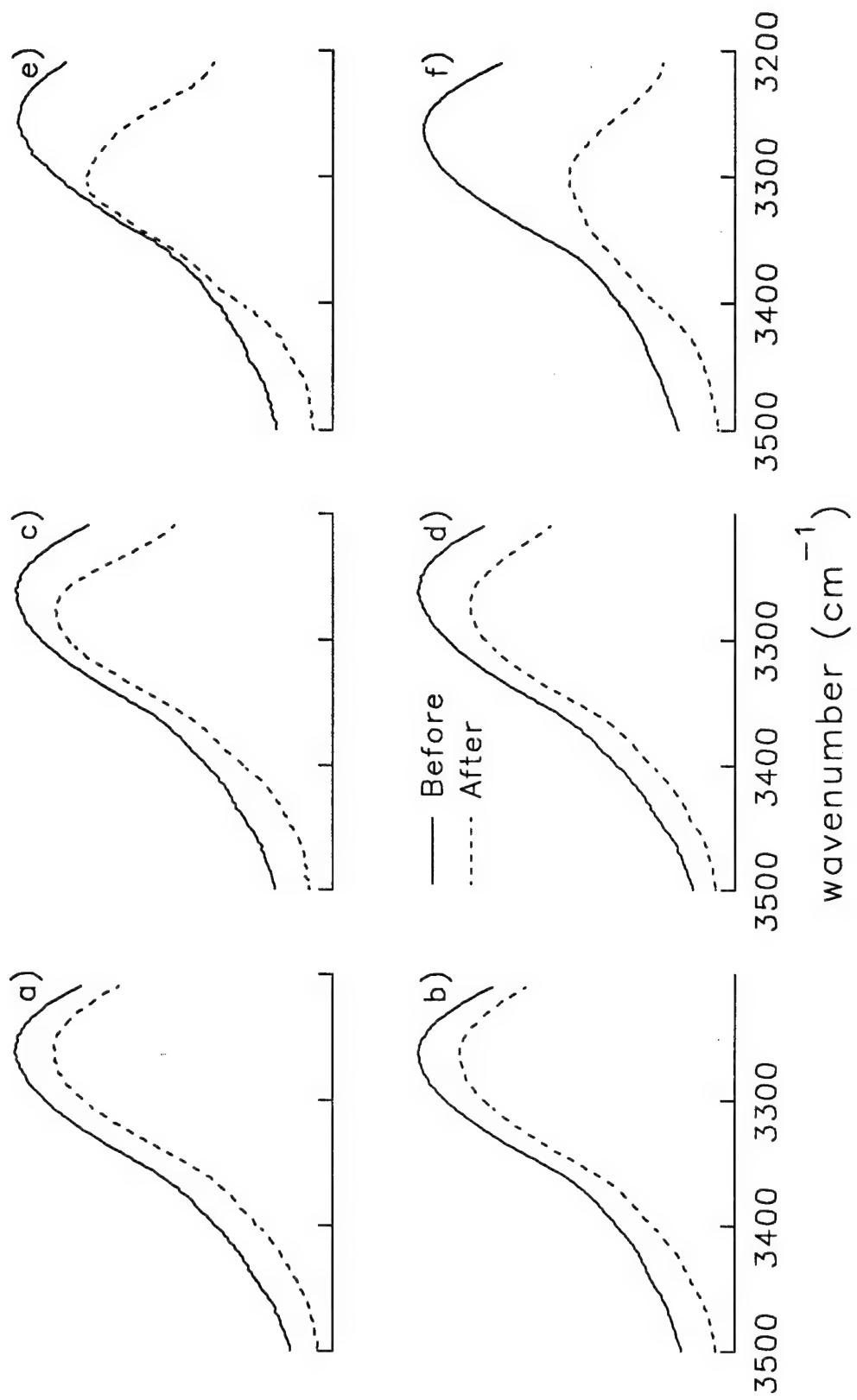
Figure VI-1. FTIR spectra of M-100-I in the N-H stretching region before and after 20 minutes heating at a) 130°C, b) 140, c) 150, d) 160, e) 170, f) 180.
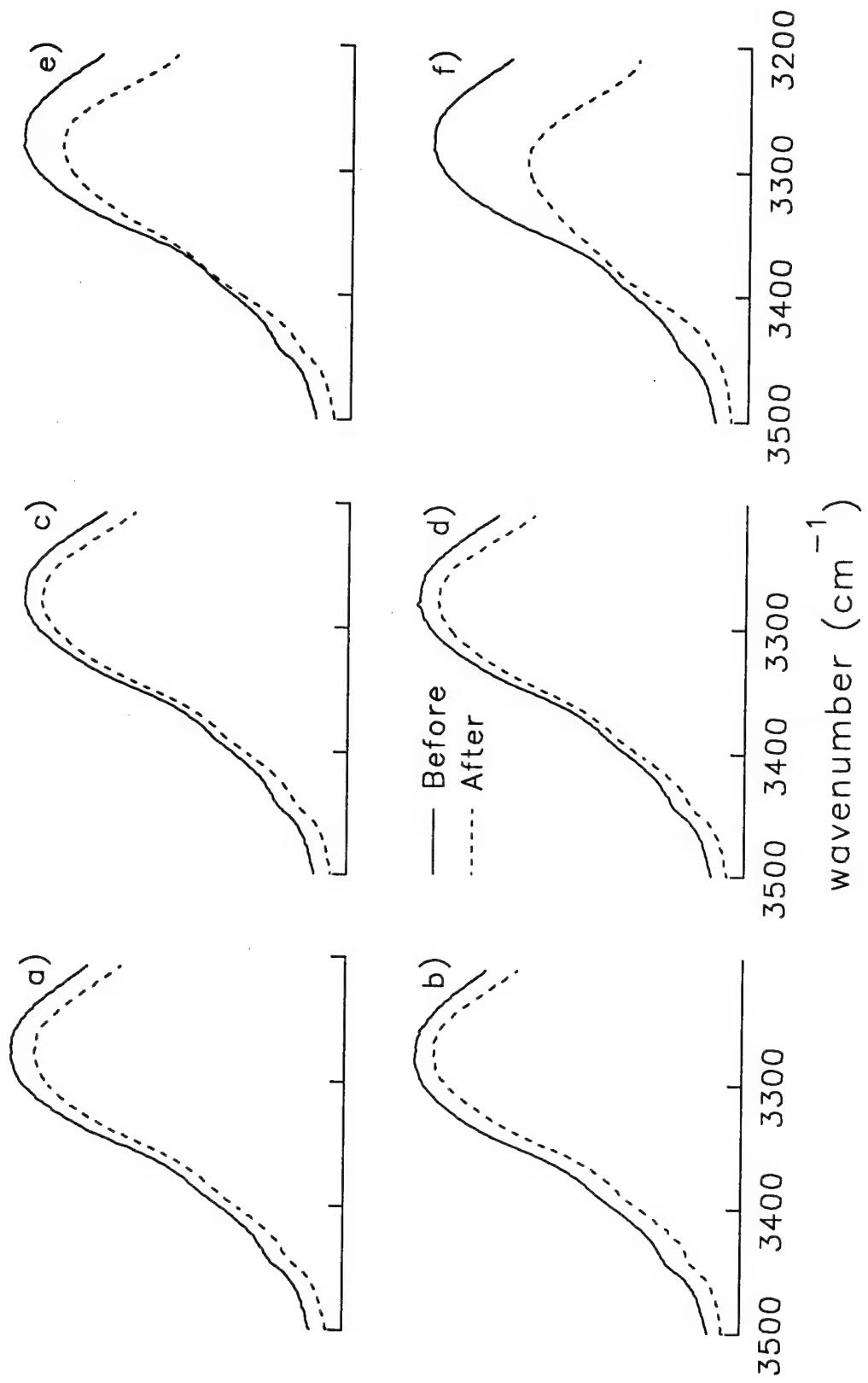
Figure VI-2. Same as Figure VI-1, except sample is M-50-I.

Table VI-2
Dequaternization as Indicated by Changes in the N-H Stretching Vibration

Temperature[a] (°C)	M-100		M-50	
	ϵ	Detectable[b] Dequaternization	ϵ	Detectable[b] Dequaternization
130	0.997	No	0.998	No
140	0.998	No	0.999	No
150	0.984	Marginal	0.999	No
160	0.983	Marginal	0.999	No
170	0.868	Yes	0.986	Yes
180	0.776	Yes	0.938	Yes

[a] 20 minutes in dry nitrogen.
[b] See text for criteria.

appears fully reversible. The heating of sample M-100-I to temperatures between 150 and 160°C was only slightly irreversible as evidenced by a subtle convergence of before and after spectra around 3350 cm^{-1}, and correlation coefficients just below 0.990. For sample M-50-I, values of ϵ would imply reversibility at 150 and 160°C. However, the subtle convergence around 3350 cm^{-1} described for M-100-I was also evident for the sample M-50-I. Based on these results, a maximum temperature of 150°C was selected for dynamic viscoelastic measurements.

Results of the brief dequaternization study also suggested that further investigation of the MST for the cationomer M-100-I would be fruitless, since experiments in the temperature regime of viscous flow would be compromised by dequaternization. However, the upper transition in DMTA spectra of sample M-50-I (Figure V-17) is only around 85°C. A "temperature window" therefore exists, between the onset of viscous flow and the experimental temperature limits defined by dequaternization, where a homogenous melt might exist.

B.2. SAXS temperature studies. Figure VI-3 shows SAXS profiles of the cationomer M-50-I, at temperatures from 30 to 130°C, after subtraction of background scattering. Data collection times ranged from 4 hours at room temperature to 2 hours at 110 and 130°C. The SAXS curve at room temperature displayed a single interference maxima at q=0.65 nm^{-1}. In Chapter III, this peak was attributed to a periodic arrangement of lamellar hard and soft domains analogous to that found in conventional PU elastomers. From 30 to 70°C, the intensity of the peak increased approximately 10%, while the position of the peak was essentially unchanged. Above 70°C there was a clear
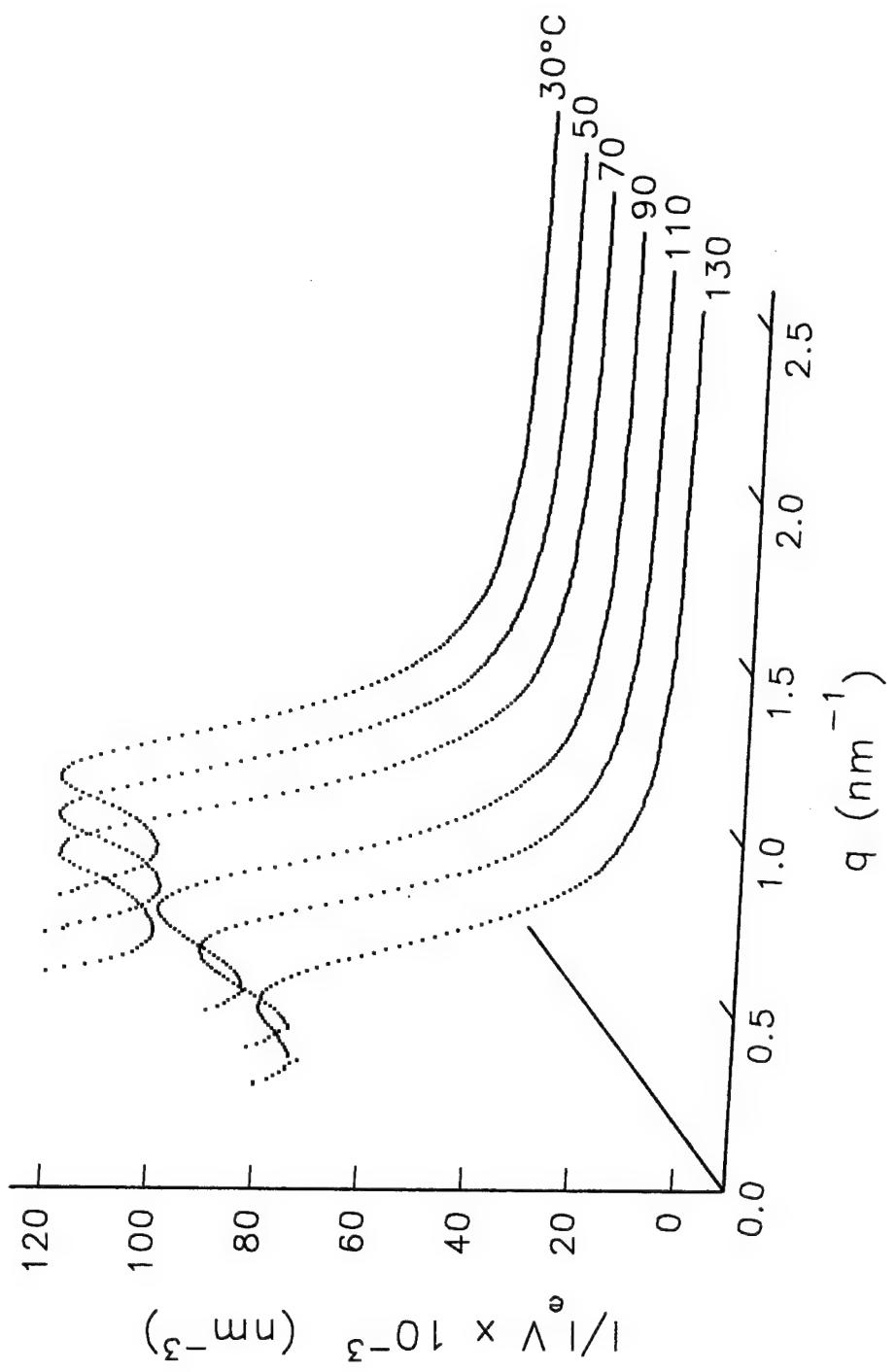
Figure VI-3.   Temperature dependence of SAXS profiles for M-50-I.

change in the scattering curves, as the intensity of the maxima decreased substantially and

the peak position shifted to lower wavevectors with increasing temperature. The decrease

in intensity was much greater than might be explained by dequaternization, because μ was

constant (within experimental error of 5%) before and after SAXS data collection at all

temperatures. This indicates that less than 7% dequaternization occurred, since iodine

atoms absorb greater than 75% of the X-rays.

Differences in morphology as a function of temperature were quantified by first

multiplying the scattered intensity by q^2. Bragg's law was applied to the peak of the

corrected profile to evaluate the interlamellar spacing L_{1-D}, while the extent of microphase

mixing was reflected in the total integrated scattered intensity, or invariant Q, given by

Equation II-4. Morphological parameters are summarized in Table VI-3, and displayed

graphically as a function of temperature in Figure VI-4. Also included in Figure VI-4 is

data from Galambos for a segmented PU with semicrystalline hard domains of

MDI/BD.[165] Three temperature regions are generally observed for conventional

polyurethanes. At low temperatures, Q increases with temperature while the interdomain

spacing may increase slightly or remain constant. Previous researchers have postulated

a variety of phenomena that could explain the trends in this region including increased

purity of the microdomains,[166] and thermal expansion.[161,163,166] Next, a temperature regime

exists where the invariant decreases sharply with increasing temperature. Since the

invariant is independent of the size and shape of the domains, the sharp decrease in Q

results from microphase mixing and the consequent loss of electron density contrast as
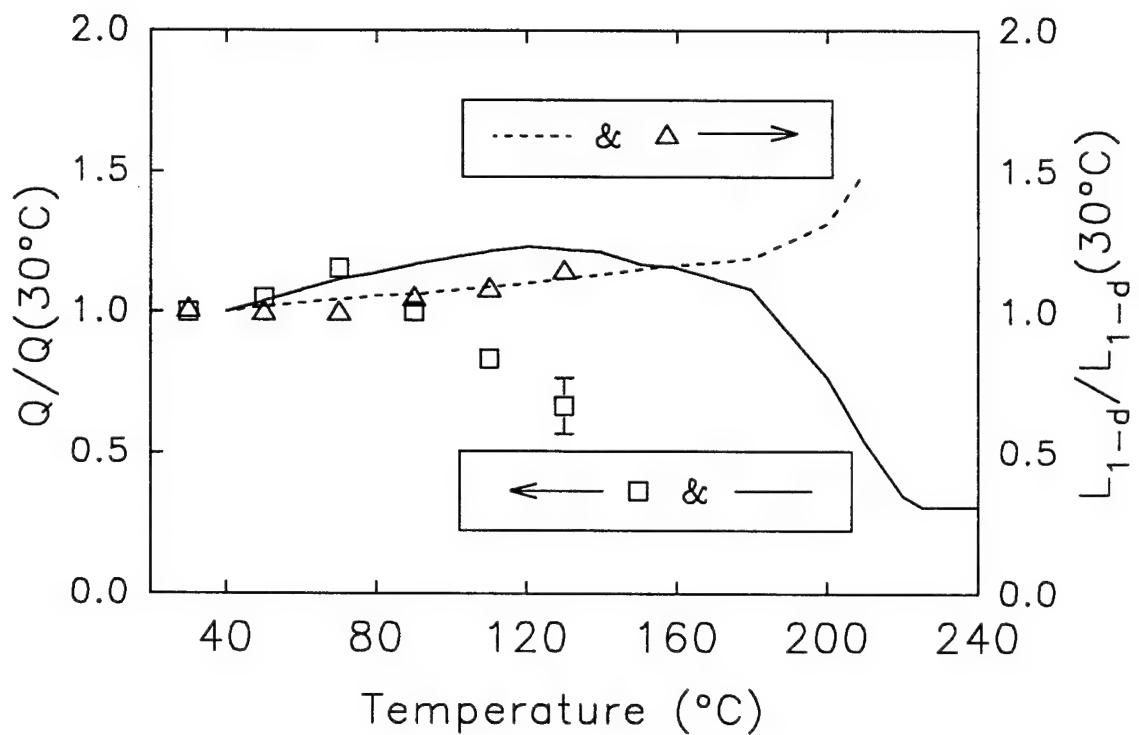
Figure VI-4. SAXS invariant and interlamellar repeat distance of the cationomer M-50-I (symbols) from patterns of Figure VI-3. Also included is data from Galambos for a PU with MDI/BD hard segments (lines).[165] All data were normalized to the values at 30°C.

Table VI-3
SAXS Parameters at Various Temperatures

Temperature (°C)	L_{1-D} (nm)	Q/V (nm^{-6})
30	9.6	31000
50	9.5	32600
70	9.5	35800
90	10.0	31100
110	10.3	25900
130	10.9	20700

indicated by the Equation II-5. Above T_{MST} the invariant plateaus, and the interdomain spacing becomes ill-defined as the interference peak decays beyond distinction.

Although the highest experimental temperature for M-50-I was limited to 130°C by dequaternization, the same general behavior was observed. Only the plateau region at high temperatures was absent. From 30 to 70°C, the invariant increased 15%, while the interlamellar distance was unchanged. In the transition region between 90°C and the maximum experimental temperature of 130°C, the repeat distance increased approximately 15% and the invariant decreased over 40%. For the PU cationomers, these results indicate that considerable intersegmental mixing accompanies the onset of viscous flow and shift in N-H bonding from the anions to urethane carbonyls. However, some evidence of the heterogeneous lamellar structure still exists in the melt to temperatures of at least 130°C.

B.3. Dynamic viscoelastic properties. The rheological properties of the cationomer M-50-I are shown in Figure VI-5, where G' and G" are plotted versus frequency at various temperatures from 60 to 150°C. At temperatures up to approximately 100°C, complex rheological behavior with a relatively weak ω-dependence was observed. At the lowest frequencies, both G' and G" approached the lines proportional to $\omega^{1/2}$ that have been observed in previous investigations of ordered diblock and triblock copolymers.[156,160,167] The ω-dependence of G' and G" increased with increasing temperature, although at 150°C the storage modulus still had a slope less steep than the line G' ~ ω^2 which is expected for homopolymers and disordered copolymers. At 150°C, the loss modulus closely matches the anticipated result G" ~ ω for
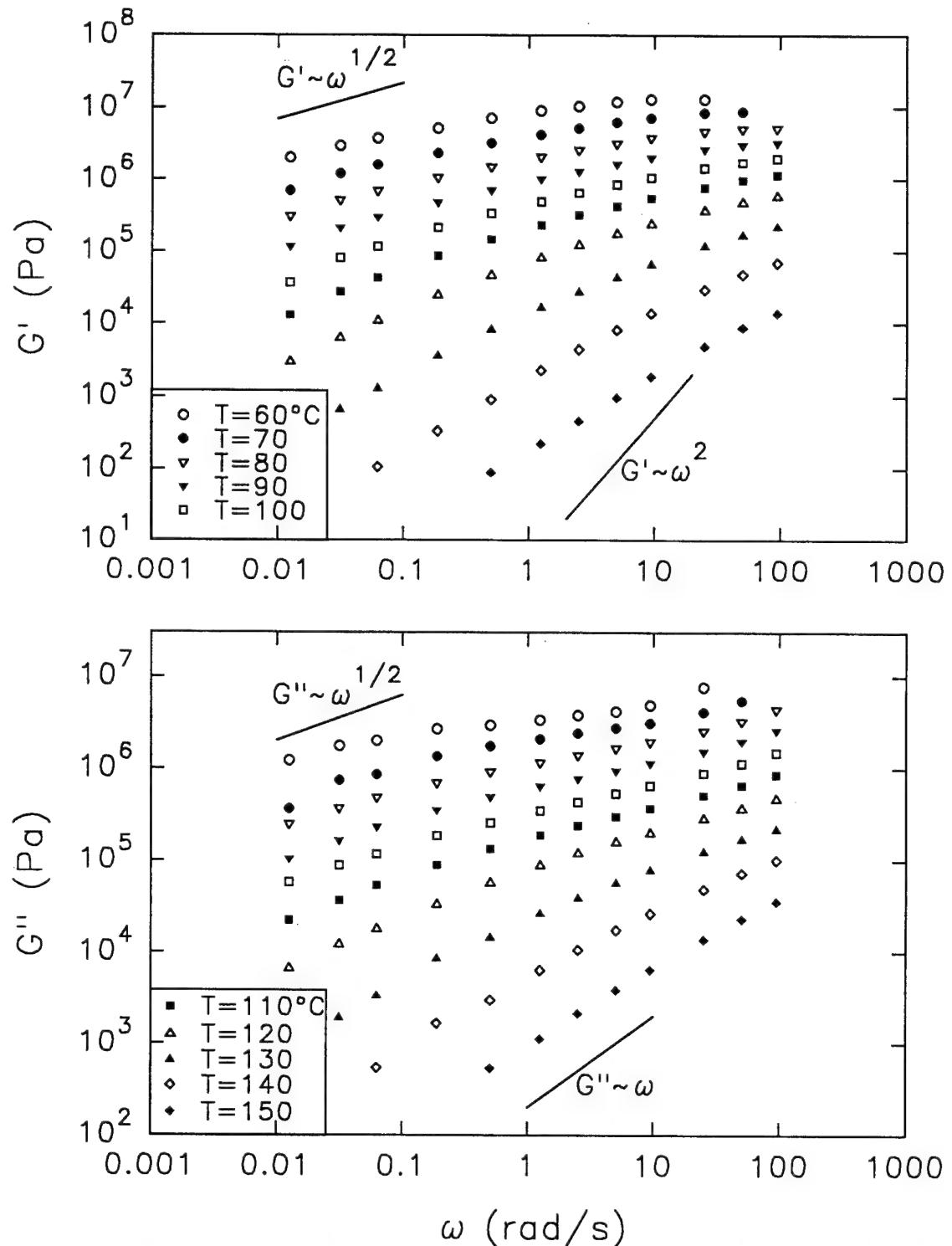
Figure VI-5. Dynamic storage modulus G' (top) and loss modulus G" (bottom) of M-50-I in the temperature interval 60-150°C.

homogeneous polymer melts. In Figure VI-6, the same G' data are replotted as isochronal temperature curves. Symmetric monodisperse diblock and triblock copolymers frequently show a sharp discontinuity in G' at T_{MST} at low frequencies.[155,156,158] At increased frequencies, the transition broadens and shifts to higher temperatures. A discontinuous drop in G' was not observed for the PU cationomer at even the lowest test frequency of 0.063 rad/s. However, a relatively sharp decline was observed starting around 110°C. Similar results, shown by the dashed line of Figure VI-6, were reported by Almdal et al.[168] for a binary mixture of diblock copolymers of the same composition but different block lengths. Their results showed that even modest asymmetries and polydispersities of the blocks led to a order-disorder transition with continuous character. They speculated the broad transition was a biphasic region, where the fraction of the disordered phase increased with increasing temperature.

Applying this reasoning to the PU cationomers, an even wider MST might be expected. Not only are the distributions of chain molecular weight and segment lengths for polyurethanes considerably broader, but individual hard-segments of the M-50-I cationomer may contain anywhere from 0 to 100% of the ionic chain-extender responsible for microphase separation. Isochronal curves at higher frequencies were shifted to higher temperatures as expected, but the ω-dependence was less than is often noted for diblock and triblock copolymers. Gouinlock and Porter reported that the greatest frequency dependence occurs around the critical reduced frequency for the polymer, above which no domain disruption occurs.[155] The critical frequency is a strong function of molecular weight as well as the copolymer composition. For the segmented PU cationomers,
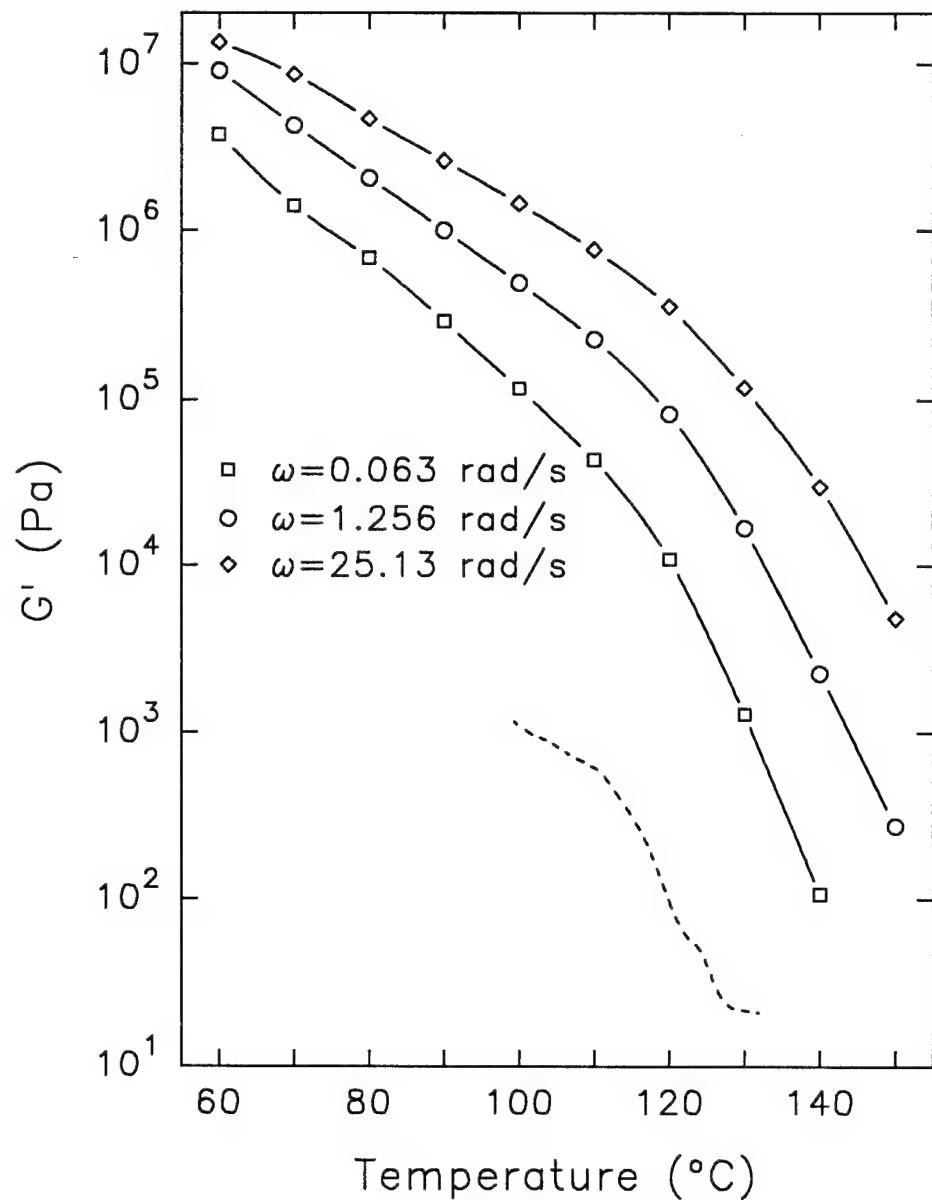
Figure VI-6. Isochronal plots of G' vs temperature for M-50-I (solid lines). Included for comparison is data for a binary mixture of diblock copolymers of the same composition but different block lengths (dashed line).[168]

extraction of individual chain segments from a domain would likely have a relatively short relaxation time due to the smaller block lengths compared to diblock and triblock copolymers. A shorter relaxation time corresponds to a higher critical frequency, which for the sample M-50-I is apparently above the greatest test frequency of 100 rad/s. A weak ω-dependence was also recently shown for a styrene-isoprene diblock copolymer with liquid-like order (i.e. the domains were not ordered onto a lattice) by Adams and co-workers.[169]

B.4. Comparison of SAXS and melt rheology. In Figure VI-7, the SAXS invariant is superimposed on a semi-log plot of G' versus temperature at ω=0.063 rad/s. Both techniques indicate a broad and continuous transition, with no "plateau" regions corresponding to a homogenous melt. At first glance, the temperature range of the transition seems to differ for the two methods. However, one must remember that only the onset and part of the breadth of a relatively wide transition are observed. The initial decrease in the SAXS invariant, at around 70°C, marks the temperature at which segmental mixing first occurs. If we assume that the biphasic model of Almdal *et al.*[168] reasonably explains the rheological transition, then the onset at approximately 110°C might be thought of as the point at which some tiny fraction of the melt behaves like a homopolymer. One would expect this to transpire at a higher temperature than the onset of segmental mixing. In Ryan and co-workers' investigation of the order-disorder transition in amorphous segmented polyurethanes, a similar difference in the "onset" temperature is observed, with the initial decline in the SAXS invariant just above 100°C and the abrupt drop in the low-frequency storage modulus starting at 148°C.[163]
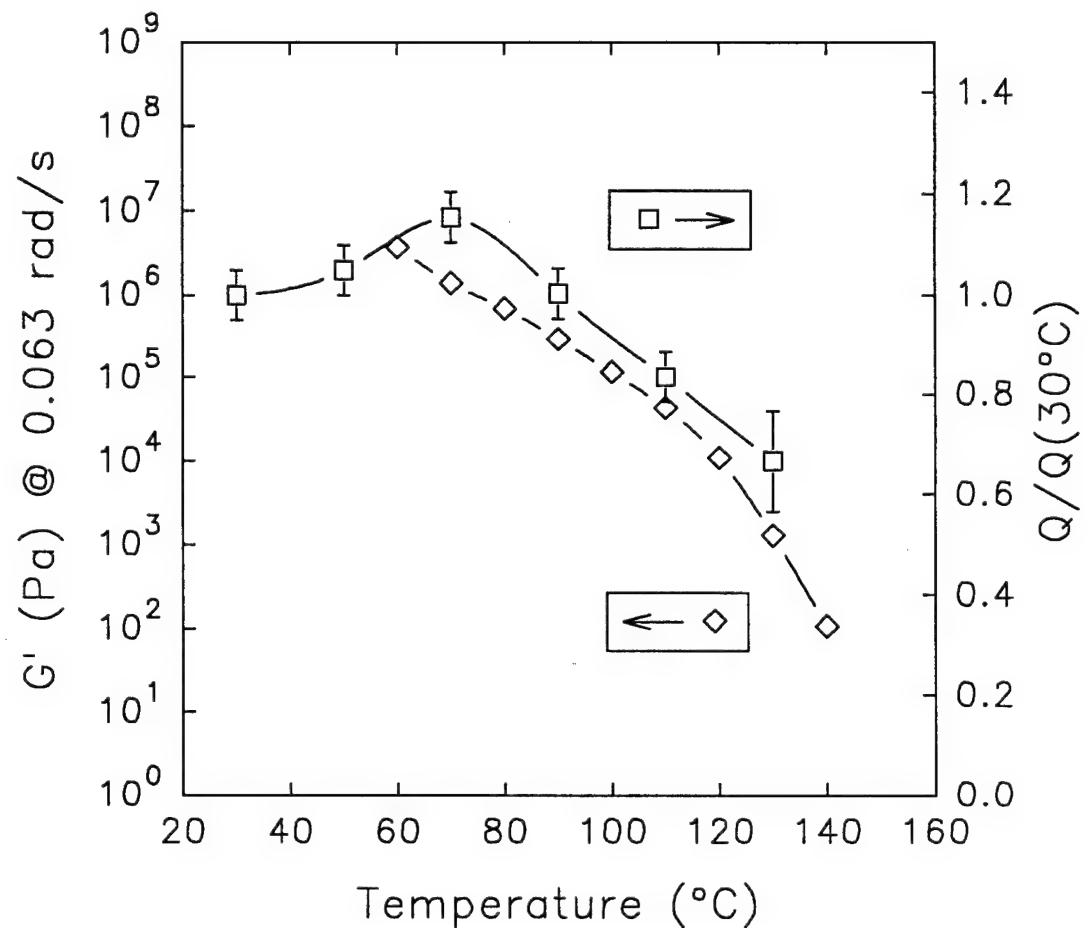
Figure VI-7. Overlay of the low-frequency storage modulus from Figure VI-6 and normalized SAXS invariant from Figure VI-4.

C. Summary

Both SAXS and rheological experiments show considerable microphase mixing near the onset of viscous flow. The SAXS invariant begins decreasing between 70 and 90°C, and drops over 40% by 130°C. An increase in the ω-dependence of G' and G" starts around 110°C, and at 150°C the rheological behavior approaches that of a homogeneous copolymer or homopolymer melt. When replotted as a function of temperature, a sharp but continuous decrease in the low-frequency storage modulus is apparent beginning at 110°C. Results of the two techniques are consistent with the onset of a broad microphase separation transition, and agree qualitatively with investigations of the MST in more conventional multiblock copolymers and less-ordered diblock and triblock copolymers. Although a transition in microstructure is suggested, and extensive intersegmental mixing clearly occurs, a homogenous melt was not observed. Dequaternization limited the upper temperature of SAXS and rheological experiments to 130 and 150°C, respectively, and a heterogeneous lamellar microstructure was still evident in the melt at the highest temperatures.

Chapter VII. Conclusions and Recommendations

Novel polyurethane cationomers with pendant trialkylammonium groups were synthesized using ionic chain extenders. The morphology and physical properties of the polymers were investigated as a function of ion content, alkyl group length, and neutralizing anion. Bulky pendant groups on the chain extenders, attached to asymmetric carbon atoms, prevented crystallization in the hard domains. In the unionized polymers little or no phase separation was evident, and the materials were adhesive-like at room temperature. Addition of cationic groups dramatically improved phase separation and mechanical properties; the tensile modulus of the cationomers chain-extended with 100% ionic diol was around 500 MPa, as compared to less than 10 Mpa for the unionized polymers and 85 Mpa for a conventional polyurethane with the same hard segment content. Within the range of variables tested, the ionic content affected phase separation and mechanical properties the most, the alkyl group length was of secondary importance, and the type of neutralizing anion had essentially no effect.

In spite of the fact that ionic interactions were the primary driving force for phase separation, small angle X-ray scattering (SAXS) and tensile results indicated a lamellar morphology akin to conventional polyurethanes with semicrystalline hard segments, rather than a typical ionomer microstructure. Further, neither SAXS patterns or extended X-ray absorption fine structure (EXAFS) spectra showed any evidence of ion aggregation within the lamellae. Results of Fourier transform infrared (FTIR) temperature studies showed that the interurethane N-H to C=O hydrogen bond found in typical polyurethanes was replaced by a stronger interaction between urethane N-H groups and the neutralizing

anion. A mass balance of functional groups suggested that roughly one N-H group is hydrogen bonded to each anion. These interchain ties are apparently the specific interaction responsible for the increased phase separation and excellent mechanical properties of the polyurethane cationomers.

On heating, a redistribution of N-H hydrogen bonds from the anion to urethane carbonyls was observed. The process was reversible to a maximum temperature of approximately 140°C, beyond which dequaternization of the ammonium groups was significant. Since the N-H to anion bonds are the primary interaction which "hold the polymer together," and the upper transition in dynamic mechanical thermal analysis was below 140°C for some cationomers, the flow transition is presumably a direct consequence of this steady shift in N-H bonding from the anion to carbonyl groups. Even though the number of N-H to anion bonds responsible for phase separation decreased at elevated temperatures, SAXS and rheological experiments showed that the lamellar microstructure persisted into the melt. However, results also indicated that macroscopic flow was accompanied by considerable intersegmental mixing, consistent with the onset of a broad microphase separation transition.

At the onset, the two main goals of this research were to systematically investigate the effect of ion-related variables on the microstructure and physical properties of polyurethane cationomers, and to obtain a greater fundamental understanding of the specific interactions in these systems. To a large extent, both objectives were met; however, a number of areas for further research are suggested.

165

With respect to polyurethane cationomers with pendant trialkylammonium groups, the investigation of the microphase separation temperature was limited by dequaternization. Materials should be synthesized using isocyanates more flexible than MDI, such as hexamethylene diisocyanate or isophorone diisocyanate, in order to lower the temperature of the viscous flow transition. Since the kinetics of dequaternization are likely not affected by the type of isocyanate, this would allow a wider "temperature window" for thermal studies in the melt. Further, SAXS data could be taken at higher temperatures and closer intervals at a synchrotron X-ray source, where the intensity of the source is orders of magnitude greater than a rotating anode.

The uncertainty in the distribution of hydrogen bonds in FTIR studies would also be reduced using aliphatic diisocyanates, since the π electrons of MDI aromatic groups can hydrogen bond. Elimination of the soft segment from the polyurethane would also reduce the number of proton acceptors, further improving the accuracy of the functional group balance.

All of the general conclusions regarding the relative effects of various ion-related variables and the nature of the specific interactions in polyurethanes with pendant ammonium groups are probably also applicable to urethanes where the quaternized amine is in the polymer backbone. However, this assumption should be tested, with the relative strengths of interactions compared in both systems.

Finally, the techniques employed in this thesis could be extended to study other polyurethane systems. Polyurethane anionomers with either carboxylate or sulfonate functionality are commercially used in aqueous dispersions, but like the cationomers the

specific interactions are not well understood. Previous investigations show some evidence of ionic aggregation within the hard domains of polyurethane anionomers;[30] however, more complex interactions may also occur with the number of different functional groups available. In blends of polyamide and sulfonated polystyrene, a variety of specific interactions were postulated to explain the observed miscibility enhancement versus unfunctionalized polystyrene, including: strong attractions between the amide carbonyl and some neutralizing cations, complexation of transition metal cations and the amide group, and hydrogen bonding between the amide N-H and sulfonate groups.[170,171] Recent work in this research group also indicates that coordination interactions can enhance phase separation and hard domain cohesion in polyurethane multiblock copolymers.[66] When acetates of various transition metals were blended with a pyridine-containing polyurethane, the tensile modulus increased by as much as 35 times that of the precursor polymer. Although coordination of the pyridine nitrogens and transition metals is expected to be the primary mechanism responsible for the dramatic increase in mechanical strength, proof of this model has not yet been obtained, and a number of other interactions are again possible.

References

1. S.L. Cooper and A.V. Tobolsky, *J. Appl. Polym. Sci.*, **10**, 1837 (1966).

2. H.N. Ng, A.E. Allegrezza, R.W. Seymour and S.L. Cooper, *Polymer*, **14**, 255 (1973).

3. S.L. Samuels and G.L. Wilkes, *J. Polym. Sci., Polym. Symp.*, **43**, 149 (1973).

4. C.G. Seefried, Jr., J.V. Koleske and F.E. Critchfield, *J. Appl. Polym. Sci.*, **19**, 2493 (1975).

5. C.G. Seefried, Jr., J.V. Koleske and F.E. Critchfield, *J. Appl. Polym. Sci.*, **19**, 2503 (1975).

6. J.W.C. VanBogart, A. Lilaonitkul, L.E. Lerner and S.L. Cooper, *J. Macromol. Sci., Phys.*, **B17**, 267 (1980).

7. N.S. Schneider, C.M. Brunett, S.L. Hsu and W.J. MacKnight, *Adv. Ureth. Sci. Tech.*, **8**, 49 (1981).

8. R. Russo and E.L. Thomas, *J. Macromol. Sci., Phys.*, **B22**, 553 (1983).

9. J.W.C. VanBogart, P.E. Gibson and S.L. Cooper, *J. Polym. Sci., Polym. Phys.*, **21**, 65 (1983).

10. S.W. Wong, K.C. Frisch, C.A. Byrne, D.P. Mack and N.S. Schneider, *Adv. Ureth. Sci. Tech.*, **9**, 77 (1984).

11. W. Nierzwicki and B. Walczynski, *J. Appl. Polym. Sci.*, **41**, 907 (1990).

12. C. Li, S.L. Goodman, R.M. Albrecht and S.L. Cooper, *Macromolecules*, **21**, 2361 (1988).

13. J. Foks, G. Michler and I. Nauman, *Polymer*, **28**, 2195 (1987).

14. R. Bonart and E.H. Müller, *J. Macromol. Sci., Phys.*, **B10**, 345 (1974).

15. J.T. Koberstein and R.S. Stein, *J. Polym. Sci., Polym. Phys.*, **21**, 1439 (1983).

16. P.E. Gibson, J.W.C. VanBogart and S.L. Cooper, *J. Polym. Sci., Part B: Polym. Phys.*, **24**, 885 (1986).

17. D. Tyagi, J.E. McGrath and G.L. Wilkes, *Polym. Eng. Sci.*, **26**, 1371 (1986).

18. J.T. Koberstein and T.P. Russell, *Macromolecules*, **19**, 714 (1986).

19. L.M. Leung and J.T. Koberstein, *Macromolecules*, **19**, 706 (1986).

20. Z.S. Petrović and I. Javni, *J. Polym. Sci., Part B: Polym. Phys.*, **27**, 545 (1989).

21. L. Cuvé, J.P. Pascault, G. Boiteux and G. Seytre, *Polymer*, **32**, 343 (1991).

22. J.T. Koberstein and A.F. Galambos, *Macromolecules*, **25**, 5618 (1992).

23. M.V. Pandya, D.D. Deshpande and D.G. Hundiwale, *J. Appl. Polym. Sci.*, **32**, 4959 (1986).

24. J.V. Duffy, G.F. Lee, J.D. Lee and B. Hartmann, *ACS Symp. Ser.*, **424**, 281 (1990).

25. G. Spathis, E. Kontou, V. Kefalas, L. Apekis, C. Christodoulides, P. Pissis, M. Ollivon and S. Quinquenet, *J. Macromol. Sci., Phys.*, **B29**, 31 (1990).

26. D. Dietrich, W. Keberle and H. Witt, *Angew. Chem. Internat. Edit.*, **9**, 40 (1970).

27. Y.S. Ding, R.A. Register, C.Z. Yang and S.L. Cooper, *Polymer,* **30**, 1213 (1989).

28. S.A. Visser and S.L. Cooper, *Polymer* **33**, 3790 (1992).

29. Y.S. Lipatov, V.I. Shtompel, V.A. Vilenskii, Y.Y. Kercha, V.A. Shrubovich and V.V. Shevchenko, *Polym. Sci. USSR* **29**, 606 (1987).

30. C.Z. Yang, T.G. Grasel, J.L. Bell, R.A. Register and S.L. Cooper, *J. Polym. Sci., Part B: Polym. Phys.* **29**, 581 (1991).

31. V.O. Lorenz, F. Haulena and D. Kleborn, *Angew. Makromol. Chem.*, **33**, 159 (1973).

32. V.A. Vilenskii, Y.Y. Kercha, Y.S. Lipatov, V.I. Shtompel, V.A. Shrubovich and V.V. Shevchenko, *Doklady Phys. Chem.*, **281**, 370 (1985).

33. Y.S. Lipatov, V.V. Shilov, S.P. Oleinik, V.A. Bogdanovich and L.A. Shelkovnikova, *Polym. Sci. USSR*, **28**, 2494 (1986).

34. V.A. Khranovskii, Y.S. Lipatov and A.F. Maslyuk, *Doklady Phys. Chem.*, **285**, 1135 (1985).

35. W. Nierzwicki and M. Rutkowska, *Polym. Comm.*, **27**, 327 (1986).

36. H.A. Al-Salah, H.X. Xiao, J.A. McLean, Jr. and K.C. Frisch, *J. Polym. Sci., Part A: Polym. Chem.*, **26**, 1609 (1988).

37. S.A. Chen and W.C. Chan, *Makromol. Chem.*, **189**, 1523 (1988).

38. W.C. Chan and S.A. Chen, *Polymer*, **29**, 1995 (1988).

39. W.C. Chan and S.A. Chen, *Angew. Makromol. Chem.*, **163**, 77 (1988).

40. S.A. Chen and W.C. Chan, *J. Polym. Sci., Part B: Polym. Phys.*, **28**, 1499 (1990).

41. S.A. Chen and W.C. Chan, *J. Polym. Sci., Part B: Polym. Phys.*, **28**, 1515 (1990).

42. T. Buruiană, I. Beştiuc and A. Caraculacu, *Angew. Makromol. Chem.*, **147**, 99 (1987).

43. M. Tanaka and T. Nakaya, *Makromol. Chem.*, **190**, 3067 (1989).

44. S.C. Varma, M.A. Ahsan, M.H. George and J.A. Barrie, *Polym. Comm.*, **31**, 11 (1990).

45. B. Chattopadyay, K. Balasubramanian, D. Ramaswamy and K.S.V. Srinivasan, *Polym. Comm.*, **31**, 15 (1990).

46. S. Kohjiya, T. Hashimoto and S. Yamashita, *J. Appl. Polym. Sci.*, **44**, 555 (1992).

47. W.P. Yang, C.W. Macosko and S.T. Wellinghoff, *Polymer*, **27**, 1235 (1989).

48. J.A. Lake, *Acta. Cryst.*, **23**, 191 (1967).

49. R.A. Register and S.L. Cooper, *J. Appl. Cryst.*, **21**, 550 (1988).

50. J.L. Koenig, *Spectroscopy of Polymers*, American Chemical Society, Washington, DC, 1992.

51. R. Bonart and E.H. Müller, *J. Macromol. Sci., Phys.*, **B10**, 177 (1974).

52. W.L. Bragg, *The Crystalline State*, Macmillan, New York, 1933.

53. C.G. Vonk and G. Kortleve, *Kolloid Z.*, **220**, 19 (1967).

54. C.G. Vonk, *J. Appl. Cryst.*, **6**, 81 (1973).

55. G. Porod, *Kolloid Z.*, **124**, 83 (1951).

56. G. Porod, *Kolloid Z.*, **125**, 51; **125**, 108 (1952).

57. A. Guinier and G. Fournet, *Small-Angle Scattering of X-Rays*, J. Wiley and Sons, New York, 1955.

58. see for example E.A. Stern, *Phys. Rev. B*, **10**, 3027 (1974) and E.A. Stern, D.E. Sayers, and F.W. Lytle, *Phys. Rev. B*, **11**, 4836 (1975).

59. B.K. Teo and P.A. Lee, *J. Am. Chem. Soc.*, **101**, 2815 (1979).

60. A.G. McKale, B.W. Veal, A.P. Paulikas, S.K. Chan and G.S. Knapp, *Phys. Rev. B*, **38**, 10919 (1988).

61. B.K. Teo, *EXAFS: Basic Principles and Data Analysis*, Springer-Verlag, New York (1986).

62. J.J. Rehr, R.C. Albers and S.I. Zabinsky, *Phys. Rev. Lett.*, **69**, 3397 (1992).

63. K.K.S. Hwang, T.A. Speckhard and S.L. Cooper, *J. Macromol. Sci., Phys.*, **B23**, 153 (1984).

64. T.A. Speckhard, K.K.S. Hwang, C.Z. Yang, W.R. Laupan and S.L. Cooper, *J. Macromol. Sci., Phys.*, **B23**, 175 (1984).

65. X. Yu, M.R. Nagarajan, C. Li, P.E. Gibson and S.L. Cooper, *J. Polym. Sci., Part B: Polym. Phys.*, **24**, 2681 (1986).

66. C.Z. Yang, X. Zhang, E.M. O'Connell, R.J. Goddard and S.L. Cooper, *J. Appl. Polym. Sci.*, **51**, 365 (1994).

67. I. Kimura, H. Ishihara, H. Ono, N. Yoshihara, S. Nomura and H. Kawai, *Macromolecules*, **7**, 355 (1974).

68. M. Shibayama, Y. Ohki, T. Korani and S. Nomura. *Polym. J.*, **19**, 1067 (1987).

69. C.W. Myers and S.L. Cooper, to be submitted.

70. C. Li and S.L. Cooper, *Polymer*, **31**, 3 (1990).

71. T.D. Gierke, G.E. Munn and F.C. Wilson, *J. Polym. Sci., Polym. Phys.*, **19**, 1687 (1981).

72. R.A. Register and S.L. Cooper, *Macromolecules*, **23**, 318 (1990).

73. R.A. Weiss, A. Sen, L.A. Pottick and C.L. Willis, *Polymer*, **32**, 2785 (1991).

74. S. Gauthier and A. Eisenberg, *Am. Chem. Soc., Polym. Prepr.*, **22(2)**, 293 (1981).

75. C.G. Bazuin and A. Eisenberg, *J. Polym. Sci., Part B: Polym. Phys.*, **24**, 1121 (1986).

76. J.T. Koberstein and R.S. Stein, *J. Polym. Sci., Polym. Phys.*, **21**, 2181 (1983).

77. D. Graiver, M. Litt and E. Baer, *J. Polym. Sci., Polym. Chem.*, **17**, 3573 (1979).

78. C.L. Marx and S.L. Cooper, *J. Macromol. Sci., Phys.*, **B9**, 19 (1974).

79. R. Longworth and D.J. Vaughn, *Am. Chem. Soc., Polym. Prepr.*, **9(1)**, 525 (1968).

80. H.W. Holden, *J. Polym. Sci., Part C, Polym. Symp.*, **6**, 53 (1964).

81. K. Tadano, E. Hirasawa, H. Yamamoto and S. Yano, *Macromolecules*, **22**, 226 (1989).

82. E. Hirasawa, Y. Yamamoto, K. Tadano and S. Yano, *Macromolecules*, **22**, 2776 (1989).

83. K. Tsunashima, H. Nishioji, E. Hirasawa and S. Yano, *Polymer*, **33**, 1809 (1992).

84. H.K. Pan, G.S. Knapp and S.L. Cooper, *Colloid Polym. Sci.*, **262**, 734 (1984).

85. K. Tsunashima, S. Kutsumizu, E. Hirasawa and S. Yano, *Macromolecules*, **24**, 5910 (1991).

86. S. Kutsumizu, Y. Hashimoto, S. Yano and E. Hirasawa, *Macromolecules*, **24**, 2629 (1991).

87. S. Yano, N. Nagao, M. Hattori, E. Hirasawa and K. Tadano, *Macromolecules*, **25**, 368 (1992).

88. H. Tachino, H. Hara, E. Hirasawa, S. Kutsumizu, K. Tadano and S. Yano, *Macromolecules*, **26**, 752 (1993).

89. E. Hirasawa, Y. Yamamoto, K. Tadano and S. Yano, *J. Appl. Polym. Sci.*, **42**, 351 (1991).

90. E. Hirasawa, K. Tadano and S. Yano, *J. Polym. Sci., Part B: Polym. Phys.*, **29**, 753 (1991).

91. E. Hirasawa, H. Hamazaki, K. Tadano and S. Yano, *J. Appl. Polym. Sci.*, **42**, 621 (1991).

92. P.C. Painter, B.A. Brozoski and M.M. Coleman, *J. Polym. Sci., Polym. Phys.*, **20**, 1069 (1982).

93. B.A. Brozoski, M.M. Coleman and P.C. Painter, *J. Polym. Sci., Polym. Phys.*, **21**, 301 (1983).

94. B.A. Brozoski, M.M. Coleman and P.C. Painter, *Macromolecules*, **17**, 230 (1984).

95. B.A. Brozoski, P.C. Painter and M.M. Coleman, *Macromolecules*, **21**, 1591 (1984).

96. S. Kutsumizu, N. Nagao, K. Tadano, H. Tachino, E. Hirasawa and S. Yano, *Macromolecules*, **25**, 6829 (1992).

97. B.P. Grady and S.L. Cooper, *Macromolecules*, **27**, in press.

98. E.A. Stern, P. Līviņš, and Z. Zhang, *Phys. Rev. B*, **43**, 8850 (1991).

99. R. Powers and R. Rudman, *J. Chem. Phys.*, **72**, 1629 (1980).

100. S.C. Abrahams and J.L. Bernstein, *Acta. Cryst.*, **B33**, 3601 (1977).

101. M. Newville, Univeristy of Washington, private communication.

102. B.P. Grady, E.M. O'Connell, C.Z. Yang and S.L. Cooper, *J. Polym. Sci., Part B: Polym. Phys.*, **32**, in press.

103. R.W.G. Wyckoff, *Z. Kristall.*, **67**, 91 (1928).

104. G. Kabisch, *J. Raman Spectrosc.*, **9**, 279 (1980).

105. R.A. Register, M. Foucart, R. Jérôme, Y.S. Ding and S.L. Cooper, *Macromolecules*, **21**, 1009 (1988).

106. Y.S. Ding, R.A. Register, C.Z. Yang and S.L. Cooper, *Polymer*, **30**, 1221 (1989).

107. D.S. Trifan and J.F. Terenzi, *J. Polym. Sci.* **28**, 443 (1958).

108. T. Tanaka, T. Yokoyama, and Y. Yamaguchi, *J. Polym. Sci., Part A-1*, **6**, 2153 (1968).

109. V.W. Srichatrapimuk and S.L. Cooper, *J. Macromol. Sci., Phys.*, **B15**, 267 (1978).

110. C.M. Brunette, S.L. Hsu and W.J. MacKnight, *Macromolecules*, **15**, 71 (1982).

111. S.B. Lin, K.K.S. Hwang, S.Y. Tsay and S.L. Cooper, *Colloid Polym. Sci.*, **263**, 128 (1985).

112. C.P. Christenson, M.A. Harthcock, M.D. Meadows, H.L. Spell, W.L. Howard, M.W. Creswick, R.E. Guerra and R.B. Turner, *J. Polym. Sci., Part B: Polym. Phys.*, **24**, 1401 (1986).

113. S.K. Pollack, D.Y. Shen, S.L. Hsu, Q. Wang and H.D. Stidham, *Macromolecules*, **22**, 551 (1989).

114. M.A. Harthcock, *Polymer,* **30**, 1234 (1989).

115. S.C. Yoon, Y.K. Sung and B.D. Ratner, *Macromolecules*, **23**, 4351 (1990).

116. T.V. Kozlova, S.V. Vdovina and V.V. Zharkov, *Polym. Sci. USSR*, **33**, 749 (1991).

117. X. Yuying, Z. Zhiping, W. Dening, Y. Shengkang and L. Junxian, *Polymer*, **33**, 1335 (1992).

118. R.W. Seymour, G.M. Estes and S.L. Cooper, *Macromolecules*, **3**, 579 (1970).

119. C.S.P. Sung, and N.S. Schneider, *Macromolecules* **8**, 68 (1975).

120. C.D. Eisenbach and W. Gronski, *Makromol. Chem. Rap. Commun.* **4**, 707 (1983).

121. J.T. Koberstein, I. Gancarz and T.C. Clarke, *J. Polym. Sci., Part B: Polym. Phys.*, **24**, 2487 (1986).

122. H.S. Lee, Y.K. Wang and S.L. Hsu, *Macromolecules*, **20**, 2089 (1987).

123. H.S. Lee and S.L. Hsu, *Macromolecules*, **22**, 1100 (1989).

124. G.M. Estes, R.W. Seymour and S.L. Cooper, *Macromolecules*, **4**, 452 (1971).

125. H.W. Siesler, *Polym. Bull.*, **9**, 471 (1983).

126. R.W. Seymour and S.L. Cooper, *Macromolecules*, **6**, 48 (1973).

127. W.J. MacKnight and M. Yang, *J. Polym. Sci., Polym. Symp.*, **42**, 817 (1973).

128. C.S.P. Sung and N.S. Schneider, *Macromolecules*, **10**, 452 (1977).

129. G.A. Senich and W.J. MacKnight, *Macromolecules*, **13**, 106 (1980).

130. M.M. Coleman, K.H. Lee, D.J. Skrovanek and P.C. Painter, *Macromolecules*, **19**, 2149 (1986).

131. J. Bufalini and K.H. Stern, *J. Am. Chem. Soc.* **83**, 4362 (1961).

132. A. Allerhand and P.R. Schleyer, *J. Am. Chem. Soc.* **85**, 1233 (1963).

133. H. Tsubomura, *J. Chem. Phys.*, **24**, 927 (1956).

134. D.J. Skrovanek, S.E. Howe, P.C. Painter and M.M. Coleman, *Macromolecules*, **18**, 1676 (1985).

135. D.J. Skrovanek, P.C. Painter and M.M. Coleman, *Macromolecules*, **19**, 699 (1986).

136. M.M. Coleman, D.J. Skrovanek and P.C. Painter, *Makromol. Chem., Macromol. Symp.*, **5**, 21 (1986).

137. Y.M. Boyarchuk, L.Y. Rappoport, V.N. Nikitin and N.P. Apukhtina, *Polym. Sci. USSR*, **7**, 859 (1965).

138. S.L. Hsu, *Acta Polymerica Sinica*, **3**, 322 (1989).

139. V.V. Zharkov, A.G. Strikovsky and T.E. Verteletskaya, *Polymer*, **34**, 938 (1993).

140. F.C. Wang, M. Feve, T.M. Lam and J.P. Pascault, *J. Polym. Sci., Part B: Polym. Phys.*, **32**, 1315 (1994).

141. F.C. Wang, M. Feve, T.M. Lam and J.P. Pascault, *J. Polym. Sci., Part B: Polym. Phys.*, **32**, 1305 (1994).

142. J.M. Widmaier and G.C. Meyer, *J. Polym. Sci., Polym. Phys.*, **18**, 2217 (1980).

143. R-J Roe, M. Fishkis and J.C. Chang, *Macromolecules*, **14**, 1091 (1981).

144. K. Mori, H. Hasegawa and T. Hashimoto, *Polymer J.*, **17**, 799 (1985).

145. J.T. Koberstein, T.P. Russell, D.J. Walsh and L. Pottick, *Macromolecules*, **23**, 877 (1990).

146. S. Sakurai, K. Mori, A. Okawara, K. Kimishima and T. Hashimoto, *Macromolecules*, **25**, 2679 (1992).

147. T. Wolff, C. Burger and W. Ruland, *Macromolecules*, **26**, 1707 (1993).

148. A. Hoffmann, T. Koch and B. Stühn, *Macromolecules*, **26**, 7288 (1993).

149. H.H. Winter, D.B. Scott, W. Gronski, S. Okamoto and T. Hashimoto, *Macromolecules*, **26**, 7236 (1993).

150. K.I. Winey, D.A. Gobran, Z. Xu, L.J. Fetters and E.L. Thomas, *Macromolecules*, **27**, 2392 (1994).

151. R.E. Cohen and A.R. Ramos, *Macromolecules*, **12**, 131 (1979).

152. F.S. Bates, H.E. Bair and M.A. Hartney, *Macromolecules*, **17**, 1987 (1984).

153. G. Kraus, F.E. Naylor and K.W. Rollmann, *J. Polym. Sci., Part A-2*, **9**, 1839 (1971).

154. C.I. Chung and C.G. Gale, *J. Polym. Sci., Polym. Phys.*, **14**, 1149 (1976).

155. E.V. Gouinlock and R.S. Porter, *Polym. Eng. Sci.*, **17**, 534 (1977).

156. F.S. Bates, *Macromolecules*, **17**, 2607 (1984).

157. C.D. Han and J. Kim, *J. Polym. Sci., Part B: Polym. Phys.*, **25**, 1741 (1987).

158. C.D. Han, D.M. Baek and J.K. Kim, *Macromolecules*, **23**, 561 (1990).

159. M.D. Gehlsen, K. Almdal and F.S. Bates, *Macromolecules*, **25**, 939 (1992).

160. N.P. Balsara, D. Derahia, C.R. Safinya, M. Tirrell, and T.P. Lodge, *Macromolecules*, **25**, 3896 (1992).

161. Y, Li, T. Gao, J. Liu, K. Linliu, C.R. Desper and B. Chu, *Macromolecules*, **25**, 7365 (1992).

162. B. Chu, T. Gao, Y. Li, J. Wang, C.R. Desper and C.A. Byrne, *Macromolecules*, **25**, 5724 (1992).

163. A.J. Ryan, C.W. Macosko and W. Bras, *Macromolecules*, **25**, 6277 (1992).

164. P. Charlier, R. Jérôme, P. Teyssié and R.E. Prud'homme, *J. Polym. Sci., Part A: Polym. Chem.*, **31**, 129 (1993).

165. A.F. Galambos, Ph.D. Dissertation, Princeton University, 1989.

166. T.P. Russell, R. Jérôme, P. Charlier and M. Foucart, *Macromolecules*, **21**, 1709 (1988).

167. F.S. Bates, J.H. Rosedale and G.H. Fredrickson, *J. Chem. Phys.*, **92**, 6255 (1990).

168. K. Almdal, J.H. Rosedale and F.S. Bates, *Macromolecules*, **23**, 4336 (1990).

169. J.L. Adams, W.W. Graessley and R.A. Register, *Am. Chem. Soc., Polym. Prepr.*, **35(1)**, 591 (1994).

170. X. Lu and R.A. Weiss, *Macromolecules*, **24**, 4381 (1991).

171. A. Molnar and A. Eisenberg, *Macromolecules*, **25**, 5774 (1992).